Matrix-free stability analysis of fluid-structure interaction problems with an Immersed Boundary method.

Politecnico di Bari

Department of Mechanics, Mathematics and Management
MECHANICAL AND MANAGEMENT ENGINEERING
Ph.D. Program
SSD: ING-IND/06–FLUID DYNAMICS

Final Dissertation

Matrix-free Stability Analysis of fluid-structure interaction problems with an Immersed Boundary method

---

by
ANTONIA TIRRI

Supervisors:
Prof. Marco D. DE TULLIO
Prof. Flavio GIANNETTI
Dr. Ing. Alessandro NITTI

Coordinator of Ph.D. Program:
Prof. Giuseppe P. Demelio

Course n°35, 01/11/2019-31/01/2023

Politecnico di Bari

Department of Mechanics, Mathematics and Management
MECHANICAL AND MANAGEMENT ENGINEERING
Ph.D. Program
SSD: ING-IND/06–FLUID DYNAMICS

Final Dissertation

Matrix-free Stability Analysis of fluid-structure interaction problems with an Immersed Boundary method

---

by
ANTONIA TIRRI

Referees:

Prof. Franco AUTERI

Prof. Simone CAMARRI

Supervisors:
Prof. Marco D. DE TULLIO

Prof. Flavio GIANNETTI

Dr. Ing. Alessandro NITTI

Coordinator of Ph.D Program:
Prof. Giuseppe P. Demelio

Course n°35, 01/11/2019-31/01/2023

ABSTRACT

The mutual interaction between viscous fluids and elastic solids plays a role in a variety of engineering applications and natural systems. In some cases, large structural deformations are sought for engineering purposes, at other times undesirable vibrations cause structural damage.

Performing accurate and high-fidelity numerical simulations to investigate the behavior of such fluid-structure interaction (FSI) problems is not trivial nor cheap, thus the development of numerical methods for FSI is a very active research area. Another possibility is to investigate the linear dynamics of these coupled systems. Linear stability analysis is a popular tool in the fluid mechanics community since it allows the faster identification of the stability criteria and gives insights into the underlying physics of the phenomena. As a matter of fact, the data resulting from temporal simulations may be difficult to interpret directly. Besides, it is usually necessary to run long simulations to go past the transient phase and see if a given perturbation fades away.

However, many FSI configurations of engineering relevance are still uninvestigated from a linear point of view due to the complexity of the linearization of the coupled dynamics. The main objective of this thesis is to promote a wide adoption of the linear approach to FSI problems. An Immersed Boundary (IB) framework is introduced, based on a direct-forcing moving-least-squares procedure to couple the fluid and solid dynamics, which has been already well validated and has proven to accurately capture the coupled dynamics. The major novelty of the present work is the development of a general approach to perform linear stability analyses of large-scale FSI problems, based on the IB method previously mentioned. To the author's knowledge, in the context of FSI systems, the global linear approach has not been yet extended to problems involving multiple elastic bodies. The proposed methodology allows the treatment of multi-body configurations with no added complexity and reasonable computational cost.

In this thesis, the proposed methodology is derived and the numerical solver is validated against results from the literature. Then, the procedure is applied to analyze the vortex-induced vibrations of two elastically mounted cylinders in tandem arrangement. Two unstable eigenmodes are identified in the analysis, and an explanation is suggested for a change in the nonlinear behavior of the system, previously noted by other researchers but still without interpretation.

In the last chapter, a different methodology is adopted to investigate the linear dynamics of a gas bubble placed in a uniform straining flow. For this case, it is used a recently developed linearized Arbitrary Lagrangian-Eulerian framework. The linear analysis of this configuration reveals the existence of a saddle-node bifurcation linked to the breakup of the bubble via an end-pinching mechanism. Interestingly, a self-propelling unstable mode emerges, which is counterintuitive as it consists in a displacement of the bubble towards a higher-pressure region. The existence of this mode is confirmed in the inviscid limit, and it is shown that the propulsive mechanism exploits shape asymmetries to create a net thrust.

PUBLISHED CONTENT AND CONTRIBUTIONS

Tirri, Antonia et al. (2023). "Linear stability analysis of fluid–structure interaction problems with an immersed boundary method". In: *Journal of Fluids and Structures* 117, p. 103830. ISSN: 0889-9746. DOI: https://doi.org/10.1016/j.jfluidstructs.2022.103830. URL: https://www.sciencedirect.com/science/article/pii/S0889974622002225.

AT implemented the numerical method, ran all the simulations and was the primary author of the article.

Sierra-Ausin, Javier, Paul Bonnefis, Antonia Tirri, David Fabre, and Jacques Magnaudet (Nov. 2022). "Dynamics of a gas bubble in a straining flow: Deformation, oscillations, self-propulsion". In: *Phys. Rev. Fluids* 7 (11), p. 113603. DOI: 10.1103/PhysRevFluids.7.113603.

AT ran part of the computations and participated in the analysis of the results.

TABLE OF CONTENTS

LIST OF ILLUSTRATIONS

LIST OF TABLES

NOMENCLATURE

λ	dynamic viscosity
$\boldsymbol{\Sigma}$	stress tensor
$\boldsymbol{\xi}$	ALE extension field
$\boldsymbol{v}$	flow velocity
χ	bubble aspect ratio
η	interface position
γ	surface tension
κ	curvature of the interface
$\boldsymbol{\Omega}$	fluid domain
Oh	Ohnesorge number
p_b	bubble pressure
S	Strain rate
V_b	bubble volume
We	Weber number
We_c	critical weber number
$\boldsymbol{\Phi}$	exponential propagator
$\boldsymbol{\Psi}_i^{\mathsf{T}}$	MLS transfer function for the i–th velocity component
$\boldsymbol{\tau}$	non-dimensional stress tensor
$\boldsymbol{F}$	nonlinear propagator
$\boldsymbol{f}$	IB forcing term
$\boldsymbol{H}_m$	Hessenberg matrix
$\boldsymbol{J}_b$	Jacobian operator
$\boldsymbol{n}$	unit normal vector

$\boldsymbol{q}$	state vector
$\boldsymbol{q}'$	perturbation vector
$\boldsymbol{q}_+$	"positive" time-stepper call for the central difference
$\boldsymbol{q}_-$	"negative" time-stepper call for the central difference
$\boldsymbol{q}_b$	base state
$\boldsymbol{q}_p$	discrete perturbation vector
$\boldsymbol{R}$	evolution operator of the nonlinear system
$\boldsymbol{u}$	non-dimensional velocity vector
$\boldsymbol{x}$	vector of non-dimensional solid displacements
$\boldsymbol{x}^l$	Lagrangian marker position
$\boldsymbol{x}_B$	structural solution
$\Delta\tilde{\boldsymbol{u}}$	velocity increment
ϵ	scaling coefficient for the perturbation vector
ϵ_0	user defined linearization parameter
$\hat{\boldsymbol{q}}$	eigenvector of the system
$\hat{\boldsymbol{u}}$	preliminary velocity field
μ	complex eigenvalue of the propagator
ν	kinematic viscosity
ω	complex eigenvalue
ρ^*	solid-to-fluid density ratio
ρ_f	fluid density
ρ_s	solid density
$\tilde{\boldsymbol{u}}$	intermediate velocity field
φ	pseudo pressure
F_i^l	Lagrangian IB forcing term
N	system size
n_e	number of Eulerian points contained in the support domain

n_{DOF} number of solid DOFs

n_{st} number of time steps for the linearization

p pressure

Re Reynolds number

Re_c critical Reynolds number

St Strouhal number

U^* reduced velocity

ALE Arbitrary Lagrangian Eulerian

CFD Computational Fluid Dynamics

CFL Courant-Friedrichs-Lewy number

CN Crank-Nicolson scheme

DNS Direct Numerical Simulation

DOF degree of freedom

EVP Eigenvalue Problem

FSI Fluid-Structure Interaction

IB Immersed Boundary

IRAM Implicitly Restarted Arnoldi Method

IVP Initial Value Problem

LSA Linear Stability Analysis

MLS Moving Least-Squares

RHS right-hand side

RK3 Third order Runge-Kutta scheme

RMSE Root-mean-square error

VIV Vortex-Induced Vibration

Chapter 1

INTRODUCTION

> *Without reason, no effect is produced in nature; understand the reason and you will not need experience.*
>
> Leonardo da Vinci

This chapter contains a brief introduction to the comprehensive topic of flow instability from a historical perspective. The chapter also provides the reader with the essential terminology employed throughout the thesis and discusses different approaches to perform the linear stability analysis of fluid-structure systems. Eventually, the structure and the objectives of the thesis are presented.

The interaction of fluid flows with elastic structures is a widespread phenomenon occurring in a variety of engineering applications and natural systems. The reconfiguration of seaweed blades in a current (Vettori and Nikora, 2019), the synchronization of a trout's gait to ambient vortices (Liao et al. 2003), and the flapping flight of a fruit fly (Lehmann, Wang, and Engels, 2021) are typical examples of *fluid-structure interaction* (FSI) in biological systems. The mutual interaction of fluid and structure plays a major role in the cardiovascular system as well. The flow of blood through the aortic valve attracted the interest of Leonardo da Vinci, who first identified the role of the vortex formation in the sinus of Valsalva during the closing of the valve (Marusic and Broomhall, 2021). During the past several years, public environmental concern has led to significant research efforts focused on bio-inspired energy harvesting mechanisms (Orrego et al. 2017; Nitti, De Cillis, and de Tullio, 2022) that exploit flow-induced vibrations (FIV) of structures to extract energy from ambient flows. In other cases, FSI leads to undesirable vibrations that cause structural fatigue and can provoke serious damage to the structure, the most dramatic example being the collapse of the Tacoma Narrows bridge (Arioli and Gazzola, 2017).

Often, these vibrations take the form of self-excited phenomena that appear above a certain threshold of a control parameter of the system. The term *self-excited* indicates that the motion of the structure and its interplay with the flow is intimately

coupled with the emergence of the oscillatory behavior, which arises without the intervention of external sources of energy. From a linear perspective, the spontaneous appearance of these vibrations represents an *instability* of the fluid-structure system.

1.1 Instabilities in fluids: an overview

The concept of stability of a dynamical system has received great attention since the nineteenth century, with the pioneering works of Poincaré and Lyapunov. In his famous memoir (Poincaré, 1886), Poincaré introduced the notion of *trajectory*, paving the way for the foundation of a theory of dynamical systems. His paper was a source of inspiration for Lyapunov, who gave a rigorous definition of asymptotic stability in his doctoral dissertation (Lyapunov, 1892). A compendium of the history of dynamical systems theory throughout the twentieth century is beyond the scope of this thesis and can be found in (Holmes, 2007). Depending on the context, different definitions of stability have been employed by researchers over time (in (Glendinning, 1994), the author identifies 57 distinct stability types!). The focus throughout this manuscript is on determining the reaction of a system to small perturbations, *i.e.* a particular state of the system is considered *stable* if every possible disturbance dies out, and *unstable* if some perturbation grows in amplitude such that the system departs from its original state. When these disturbances are considered to be infinitesimal, the stability of the system can be inferred from the linearized equations that govern the evolution of such perturbations.

In the field of fluid mechanics, the concept of hydrodynamic stability plays a fundamental role given its connection with the transition to turbulence. It is recognized that, under given steady boundary conditions, there exists a solution of the steady Navier-Stokes equations, yet not every mathematically valid solution is observed in real life. The explanation lies in the instability of the solution with respect to infinitesimal disturbances, therefore, these flows occur in practice only for certain ranges of the parameters that govern the dynamics. The most famous of these parameters is certainly the Reynolds number Re, named after Osborne Reynolds and his classic experiments (Reynolds, 1883) on the instability of the laminar Poiseuille pipe flow. Together with Reynolds' observations on the transition to turbulence of pipe flow, in the nineteenth century, the foundations were laid for many others of the essential problems of hydrodynamic stability, thanks to the interest of renowned scientists such as Stokes, Helmholtz, Kelvin, and Rayleigh, just to name a few.

In general, the objective of the stability analysis of flows is the identification of

the *neutral* states of the system, *i.e.* those particular equilibrium solutions that are neither linearly stable nor unstable , as a function of the characteristic parameters. A typical example of this concept is provided by the flow over a bluff body. It is well-known that the steady flow around a circular cylinder loses its stability for a critical Reynolds number Re_c that is slightly below 50 (Giannetti and Luchini, 2007). For Reynolds numbers larger than that Re_c, unsteady vortices are observed to detach periodically from the cylinder's surface. This two-dimensional flow pattern was first described by Theodore von Kármán and is now recognized as an *absolute* instability (Huerre and Monkewitz, 1985) of the wake of solid obstacles, *i.e.* a disturbance that grows locally in time, associated with a Hopf *bifurcation* .
On the other hand, an example of *convective* instability, corresponding to a perturbation that is amplified as it is advected far from the location of the impulse, is provided by the mixing layer between two parallel streams with different velocities. In this case, vortices appear in the shear layer as a consequence of the Kelvin-Helmholtz instability mechanism, then these vortical structures grow as they are convected downstream. In this sense, the mixing layer functions as a noise amplifier. Another representative example of convective instability is provided by the boundary layer over a flat plate placed in a uniform flow. In this flow configuration, disturbances are created close to the leading edge but intermittent structures appear farther downstream under the form of Tollmien-Schlichting waves that ultimately lead to turbulence.

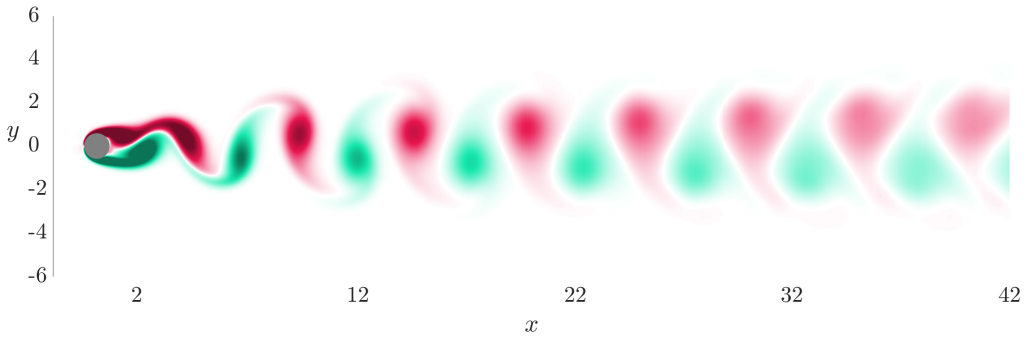

Figure 1.1: A typical flow instability, the Von Kármán vortex wake behind a fixed circular cylinder. The image shows the vorticity field of a snapshot of a simulation at $Re = 100$. The simulation was conducted by the author, with the finite-difference solver described in section 2.4 at a constant $CFL = 0.2$.

Instabilities occur in elastic solids as well. For example, when a slender structure is compressed beyond a critical level, it can deflect laterally as a sign of buckling instability. This phenomenon, already recognized by Euler in the eighteenth century,

can lead to severe damage and even to the failure of the structure. Another example of elastic instability is the torsional instability of a slender rod. For large values of torsional stresses, the rod coils around itself eventually forming a twisting knot (Ciarletta and Destrade, 2014).

Fluid-structure instabilities

When fluids and solids are coupled together, the already-reach dynamics exhibited by the two separate systems becomes even more complex due to their mutual interaction. In some cases, previously existing instability mechanisms can interact and reciprocally intensify one another. It is the case of the vortex-induced vibration (VIV) of an elastically mounted bluff body placed in a cross-flow. The global instability resulting in the vortex-shedding in the wake of a fixed body has already been mentioned before; When the solid is free to move, the fluctuations in the lift force, caused by the unsteady wake, result in an oscillatory motion of the bluff body, which in turn influences the wake dynamics. These oscillations are frequently encountered in engineering applications and are, in general, not worrisome. It is only when the frequency of vortex shedding and the natural frequency of the structure are close to each other that the *lock-in* phenomenon occurs and large-amplitude oscillations can arise.

Other instability types, on the contrary, do not show a connection with pre-existing instability mechanisms but are the result of an unstable coupling of the two systems, as in the case of the coupled-mode *flutter* that is often observed for aerodynamical sections. In the latter case, the instability is due to the coupling of the flexion and torsion modes of the section as the flow velocity increases. This phenomenon is inherently different from the VIV of a bluff body since its main feature is that the frequency of oscillation is zero at the beginning, but it becomes finite as the velocity of the flow increases. From a linear perspective, the emergence of flutter is linked to the instability of one of the structural modes that are connected via the flow field (de Langre, 2006). Nonetheless, unstable states characterized by static divergence, large and small-amplitude flapping (see Figure 1.2), and chaotic behavior can be also present with a rigid structure, as in the case of the rigid inverted flag, attached at its trailing edge to a torsional spring (Leontini and Sader, 2022).

Other examples of these new classes of instability emerging in FSI configurations are the *galloping* of bridge decks and the static *divergence* instability of wing sections. The former is a phenomenon characterized by much lower frequencies than the vortex shedding frequencies of the wake and takes its name from its resemblance with a

galloping horse. The latter, instead, is a static aeroelastic instability that corresponds to the destabilization of the pitching mode of the wing section (E. H. Dowell et al. 1989) without the presence of oscillations around the new angle of attack.

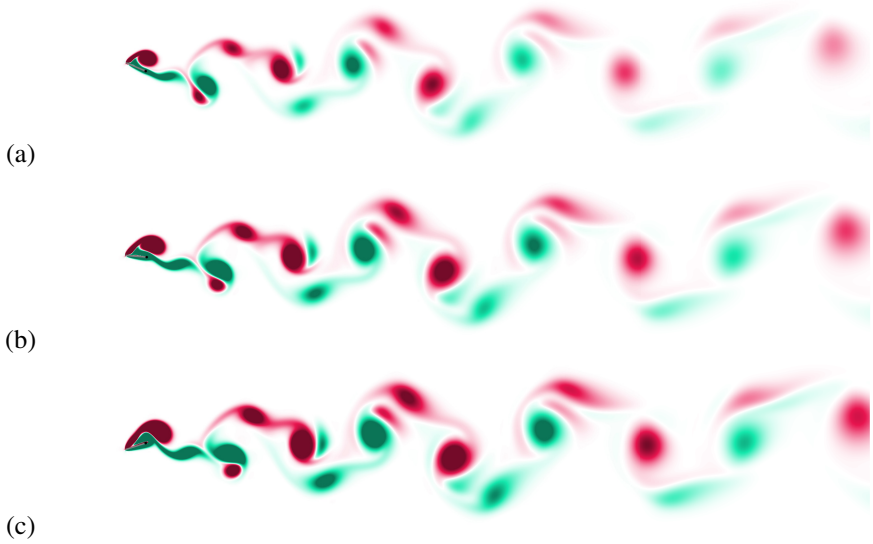

Figure 1.2: Large-amplitude flapping regime of a rigid inverted flag placed in a uniform flow. The image shows the vorticity field for three snapshots of a simulation at $Re = 200$. The simulation was conducted by the author, with the solver described in section 2.4. The (hinged) trailing edge of the flag is marked with a black circle.

Linear Stability Analysis of flows: historical background The essence of the linear stability theory lies in the investigation of the temporal and spatial evolution of small-amplitude disturbances superimposed on either a steady or time-periodic laminar base flow. Specifically, one wants to investigate the response of the system once it is perturbed from its equilibrium: will the disturbance die away, or will the system reach a new state? To answer this question, the basic idea is to linearize the Navier-Stokes equations around the *base flow*, or *basic* state, to obtain an initial value problem (IVP) that governs the evolution of small amplitude perturbations. In agreement with the definition, a stable base flow is stable to all possible infinitesimal disturbances, therefore, a proper stability analysis should examine a generic perturbation. This is usually done, in practice, by expanding the disturbance into a suitable set of *normal modes* and later investigating the stability of the base flow with respect to each mode separately. This classic ansatz follows from the observation that the coefficients of the linearized problem are independent of time, thus one can in principle separate the variables in time via eigensolution expansion to get a generalized eigenvalue problem (EVP) . The modal approach (Juniper, Ardeshir Hanifi, and

Theofilis, 2014) is justified by the observation that, close to the instability threshold, the amplitudes of the disturbances are typically small and exponentially growing. Consequently, a necessary and sufficient condition for the linear stability of a basic flow is the absence of normal modes with a positive growth rate.

Given a three-dimensional basic state, the most general application of the modal approach requires the identification of time-periodic perturbations whose amplitude function is inhomogeneous in each of the three directions. However, from a computational perspective, the size of the generalized EVPs resulting from the discretization of the three-dimensional linearized Navier-Stokes equations makes a direct solution challenging. Early analyses based on the linear theory circumvented this hurdle by way of the *parallel-flow* assumption. This approach, also termed *local* analysis and dating back to the first half of the past century (Huerre and Monkewitz, 1990), exploits the spatial separation of variables by assuming the existence of only one inhomogeneous direction as far as the linear perturbations are concerned. This approximation, which is suitable for external flows such as boundary layers and shear layers (Drazin and Reid, 2004), or for axisymmetric flow configurations, generates an EVP of reasonable size that can be solved through direct techniques. However, the number of industrially relevant flows that show dependence upon only one coordinate is rather limited. When the focus is on flows through more complex geometries, the assumption of two homogeneous directions fails to adequately represent the underlying physics of the phenomena. These flow conditions require a *global* analysis, whose eigenfunctions, differently from the local approach, show a dependence on all the spatial coordinates. At a minor level of approximation with respect to the local approach, one finds the weakly non-parallel linear analysis, employed through the 1980s to circumvent the restriction of a parallel base state (Chomaz, 2005). Within the weakly non-parallel assumption, the base flow shows one homogeneous and one slowly varying spatial direction while the disturbance field is assumed to vary on a shorter length scale such that it behaves as if the base flow were parallel at each location of the weakly inhomogeneous coordinate.

With the advance in computing power and owing to the availability of publicly available libraries that implement efficient numerical methods for the numerical solution of large-scale generalized EVPs, the linear analysis of complex flows with a global approach has become feasible. In the past decades, the range of applications of global linear theory has expanded significantly in several areas of fluid mechanics (V. Theofilis, 2011). The most common approach consists in discretizing the Linearized Navier-Stokes equations, *e.g.* by means of spectral methods, finite

elements or finite differences, and solving the resulting generalized eigenvalue problem, often by means of standard library sub-routines. For instance, Zebib (Zebib, 1987) carried out the first linear stability analysis of the two-dimensional flow past a circular cylinder exploiting Chebyshev polynomials. During the second half of the twentieth century, algorithms based on the QZ decomposition have been extensively applied to investigate the full eigenspectrum of a wide class of flows. When attainable, the computation of the full eigenspectrum is to be preferred as it provides a comprehensive overview of the physics of a new problem under investigation. However, this approach comes across computational difficulties for large-scale systems ($N \sim O(10^6)$) as computing time and memory requirements grow as $O(N^3)$ and $O(N^2)$, respectively (V. Theofilis, 2011), where N is the size of the system matrix. This is the reason for the popularity gained through the 80s and 90s by various libraries that implemented iterative methods (ARPACK (Lehoucq, Sorensen, and Yang, 1998), LAPACK (Anderson et al. 1990)). The most common class of iterative approaches is that of Krylov subspace methods. This family of algorithms is based on the assumption that the eigenvalue problem can be projected on a vector space characterized by a much smaller dimension. As a consequence, iterative methods are able to retrieve a limited portion of the spectrum compared to the full spectrum recovery of direct methods. Nonetheless, such iterative techniques are favored by the fact that, in most fluid mechanics applications, the interest is just on a few least stable eigenvalues.

A further distinction can be done between *matrix-forming* and *matrix-free* strategies. Within the former approach, the stability matrix of the system is explicitly assembled and stored. On the contrary, matrix-free techniques simply evaluate a sequence of matrix-vector products in order to assemble the subspace needed by an iterative solver. The considerations about memory and hardware requirements done for direct and iterative methods apply also to matrix-forming and matrix-free strategies. One aspect that is worth noticing about the matrix-free framework regards the difficulties that arise with spectral transformation and preconditioning. Typically, preconditioning techniques are needed to achieve a good convergence rate in a Krylov method. In addition, it is often desirable to alter the spectrum in order to separate the eigenvalues and promote the emergence of the most interesting ones. This is often the case when the desired eigenvalues are not the dominant ones, or when they are clustered around a certain value.

In general, spectral transformations involve the use of a preconditioning matrix, the construction of which requires access to the stability matrix in explicit form. This

is clearly unattainable in a matrix-free environment, where information about the matrix is obtained only through matrix-vector products, therefore one has to recur to simplified preconditioners based on estimates of the actual matrix.

Finally, to close this brief discussion about the methods and applications of linear stability analysis (LSA) in fluid mechanics, it is worth remarking that linear analysis does not necessarily imply modal analysis, even though the normal-mode approach has dominated the field of hydrodynamic stability theory for several decades. Recently, this traditional technique has been complemented with the relatively new nonmodal analysis (Schmid, 2007). The concept at the base of this tool is that the non-normality of the linearized Navier-Stokes operator can lead to large transient energy growth of a perturbation (Trefethen et al. 1993). As a matter of fact, nonmodal effects can account for the discrepancies observed in the transitional Reynolds number between linear predictions and experiments for several wall-bounded shear flows (Schmid and D. Henningson, 2001).

1.2 Stability analysis of fluid-structure problems

Despite the significant advances achieved in the last decades in the application of global stability analysis of flows through complex geometries, the field of FSI remains largely unexplored from a linear point of view. The reason lies in the complexity of the linearization process in presence of a moving fluid-solid interface. Hence, these configurations are generally investigated by way of experiments and high-fidelity temporal simulations.

In the context of fluid-solid instability, classic approaches to determine the onset of vibrations were either theoretical or adopted reduced-order models both for the fluid and solid dynamics. The first examples of linear stability analyses over FSI configurations date back to the pivotal studies of Theodorsen (1934) on the flutter instability of an aerodynamic section. Theodorsen's formulation was based on the potential flow and slender body assumptions. The same analytical approach was also followed by Kornecki, E. Dowell, and O'Brien (1976), who theoretically investigated the divergence and flutter instability of a panel in a two-dimensional incompressible flow. More recent applications of theoretical approaches to the linear stability analysis of plates can be found in the works of Guo and Paidoussis (1999) and Eloy, Souilliez, and Schouveiler (2007). In their work, Argentina and Mahadevan (2005) investigated the stability of cantilevered flags in axial flow extending Theodorsen's formulation to include the effects of viscous drag and finite plate length.

Even though the adoption of these simplified flow models is legitimate in the field

of classic aeronautics, applications involving low to medium Reynolds numbers or flow separation require the simultaneous solution of the linearized Navier-Stokes equations coupled with the linearized equation of motion of the elastic solid. As a low-cost alternative, reduced-order methods have been applied to recover the mean features of some FSI configurations involving bluff bodies in low-to-medium Reynolds number flows; de Langre (2006), for instance, investigated the VIVs of a spring-mounted rigid cylinder modeling the wake dynamics as a van der Pol oscillator. Cossu and Morino (2000) were the first to perform a linear stability analysis of a two-dimensional low Reynolds number flow interacting with an elastically-mounted bluff body. They investigated the primary instability of a circular cylinder, which was free to oscillate in the cross-flow direction by solving the linearized flow equations in a moving reference frame. Navrose and Mittal (2016) adopted the same approach with a non-inertial frame of reference to conduct a parametric study of the lock-in phenomenon exhibited by elastically-mounted circular cylinders in the laminar flow regime. Cossu and Morino (2000) reported a critical Reynolds number that is about half of the value obtained for the fixed cylinder case with low solid-to-fluid density ratios. Meliga and Chomaz (2011) extended the stability analyses to smaller mass ratios ($O(10^{-4})$), employing a multiple-time-scale expansion to decouple fluid and solid dynamics at the leading order of the perturbation.

More recently, Pfister, Marquet, and Carini (2019) adopted a Lagrangian-based approach to derive a linearization of the equations of motion for a coupled fluid-structure problem written in an Arbitrary-Lagrangian-Eulerian (ALE) framework. This formulation becomes cumbersome when it is based on the Lagrangian motion of the structure, requiring important modifications in the residual of the Navier-Stokes equations to take into account the motion of the mesh. Fernández and Le Tallec (2002) proposed, instead, an Eulerian-based formulation of the perturbation in an attempt to overcome the difficulties arising from a moving grid. In their formulation, obtained starting from the weak form of the ALE equations, the coupling between the flow and the solid is made via a transpiration technique. Although reducing considerably the complexity of the problem, this method produces additional stress contributions at the interface, termed *added stiffness*, that depend on higher-order derivatives of the flow variables. Negi, A. Hanifi, and D. S. Henningson (2020) followed the same methodology but performed the linearization of the equations of motion in their strong form.

Moulin et al. (2017) suggested the use of non-conforming methods to investigate the stability of strongly coupled FSI systems, discussing, in particular, the adoption

of a fictitious domain formulation to handle the coupling between the fluid and the solid. Goza, Colonius, and Sader (2018), who also proposed a non-conforming approach, conducted the global stability analysis of an inverted flag in a uniform flow using an Immersed Boundary (IB) method . They resorted to the numerical derivation of the Jacobian matrix linearizing the discretized operators around the steady state via a first-order finite difference scheme. The memory requirements with matrix-forming strategies become rapidly unfeasible when dealing with a large number of degrees of freedom, e.g. three-dimensional FSI configurations. This aspect is even more relevant in the computation of neutral curves since the Jacobian matrix must be re-evaluated for each base flow.

1.3 Motivation and outlook

Many FSI configurations of industrial relevance are still unexplored from a linear perspective due to the complexity of the linearization of the coupled dynamics. For this reason, the main objective of this thesis is to propose an alternative, matrix-free methodology for the global stability analysis of viscous laminar flows interacting with elastic solids.

The method is based on a time-stepping procedure that makes use of high-fidelity nonlinear simulations obtained with a direct-forcing immersed boundary (IB) method, based on a moving-least-squares (MLS) approach. One of the main advantages of the IB formulation resides in the fact that it can handle multi-body configurations with no additional complexity. Besides, the fluid equations are solved on a staggered Cartesian grid, which makes the method prone to a simple parallel implementation for three-dimensional computations.

Details on the IB treatment are provided in Chapter 2. The method has undergone extensive validation through the years (de Tullio and Pascazio, 2016). Here, its key components are analyzed from a linear perspective, and special care is given to the computation of the forces acting on the immersed body. The choice of the specific IB forcing technique is indeed crucial for the success of linear computations.

In Chapter 3, the problem of linear stability in the context of fluid-structure interaction is introduced and the methodology is derived from theoretical considerations. The proposed strategy involves the adoption of the matrix exponential, first introduced by Eriksson and Rizzi (1985) in the context of global stability analysis of the Euler equations. The same approach was later extended to the full Navier-Stokes equations by Chiba (1998), who performed a linear stability analysis of the two-dimensional square lid-driven cavity flow. This contribution provides an extension

of Chiba's approach to FSI problems. To the author's knowledge, time-stepping techniques had not been applied to study the linear stability of FSI problems up to this work. The numerical linearization proposed in this thesis accounts for the fully coupled solid and fluid dynamics, and thus is able to identify all the instability mechanisms arising in the system. In addition, the general formulation derived here can be directly applied to multi-body FSI problems without modifications, and with a little increase in the computational effort, a characteristic that is not shared by grid-conforming methodologies. The proposed time-stepping IB approach, indeed, is able to extract stability information from simulations, irrespective of the total number of immersed bodies or the complexity of the multi-physics phenomenon under investigation.

Details of the numerical implementation of the solver are given in section 3.4, together with a discussion of the most critical aspects. The method is then validated against the benchmark case of the vortex-induced vibrations of an elastically mounted rigid cylinder. Chapter 4 reports the results obtained by applying the presented strategy to the problem of flow-induced vibrations of two cylinders in tandem. The obtained results provide further confidence in the robustness of the method. Besides, the linear predictions identify an unstable eigenvalue responsible for a change of behavior of the system already observed in previous studies, which has remained without explanation until now.

Chapter 5 is dedicated to the stability analysis of a gas bubble placed in a uniaxial straining flow. In this case, the role of the solid elasticity is taken by the surface tension at the interface between the two fluids. The linear dynamics of the system is investigated by means of a recently developed (Bonnefis, 2019) method based on a linearized Arbitrary Lagrangian-Eulerian framework. The analysis systematically revises this classic problem from a linear perspective. Results from the literature are confirmed for the stable base states, and a second unstable branch of steady states is found via a continuation method, linked to the stable branch through a saddle-node bifurcation. The unstable branch leads to the breakup of the bubble via an end-pinching mechanism. Interestingly, a self-propelling unstable mode emerges, which is counterintuitive as it consists in a displacement of the bubble towards a higher-pressure region.

Finally, Chapter 6 summarizes the results of the thesis and offers an outlook on future developments.

References

Anderson, E. et al. (1990). “LAPACK: A portable linear algebra library for high-performance computers”. English. In: *SC*. Proceedings of Supercomputing ’90 ; Conference date: 01-07-1990. United States: IEEE, pp. 2–11. ISBN: 0818620560.

Argentina, Mederic and Lakshminarayanan Mahadevan (Mar. 2005). “Flow-induced flutter of a flag”. In: *Proceedings of the National Academy of Sciences of the United States of America* 102, pp. 1829–34. DOI: 10.1073/pnas.0408383102.

Arioli, Gianni and Filippo Gazzola (2017). “Torsional instability in suspension bridges: The Tacoma Narrows Bridge case”. In: *Communications in Nonlinear Science and Numerical Simulation* 42, pp. 342–357. ISSN: 1007-5704. DOI: https://doi.org/10.1016/j.cnsns.2016.05.028.

Bonnefis, P. (2019). “Etude des instabilités de sillage, de forme et de trajectoire de bulles par une approche de stabilité linéaire globale”. PhD thesis. Toulouse, France (available online at http://www.theses.fr/2019INPT0070): Inst. Nat. Polytech. Toulouse.

Chiba, Satoshi (1998). “Global stability analysis of incompressible viscous flow”. In: *Journal of Japan Society of Computational Fluid Dynamics* 7, 20–48 (In Japanese).

Chomaz, Jean-Marc (2005). “GLOBAL INSTABILITIES IN SPATIALLY DEVELOPING FLOWS: Non-Normality and Nonlinearity”. In: *Annual Review of Fluid Mechanics* 37.1, pp. 357–392. DOI: 10.1146/annurev.fluid.37.061903.175810.

Ciarletta, Pasquale and Michel Destrade (Sept. 2014). “Torsion instability of soft solid cylinders”. In: *IMA Journal of Applied Mathematics* 79, pp. 804–819. DOI: 10.1093/imamat/hxt052.

Cossu, C. and L. Morino (2000). “On the instability of a spring-mounted circular cylinder in a viscous flow at low Reynolds numbers”. In: *Journal of Fluids and Structures* 14.2, pp. 183–196. ISSN: 0889-9746. DOI: https://doi.org/10.1006/jfls.1999.0261.

de Langre, E. (2006). “Frequency lock-in is caused by coupled-mode flutter”. In: *Journal of Fluids and Structures* 22.6. "Bluff Body Wakes and Vortex-Induced Vibrations (BBVIV-4), pp. 783–791. ISSN: 0889-9746. DOI: https://doi.org/10.1016/j.jfluidstructs.2006.04.008.

de Tullio, M.D. and G. Pascazio (2016). “A moving-least-squares immersed boundary method for simulating the fluid–structure interaction of elastic bodies with arbitrary thickness”. In: *Journal of Computational Physics* 325, pp. 201–225. ISSN: 0021-9991. DOI: https://doi.org/10.1016/j.jcp.2016.08.020.

Dowell, Earl H. et al. (1989). *A modern course in aeroelasticity*. Dordrecht: Springer Netherlands. ISBN: 978-94-015-7858-5. DOI: 10.1007/978-94-015-7858-5.

Drazin, P. G. and W. H. Reid (2004). *Hydrodynamic Stability*. 2nd ed. Cambridge Mathematical Library. Cambridge University Press. DOI: 10.1017/CBO9780511616938.

Eloy, C., C. Souilliez, and L. Schouveiler (2007). "Flutter of a rectangular plate". In: *Journal of Fluids and Structures* 23.6, pp. 904–919. ISSN: 0889-9746. DOI: https://doi.org/10.1016/j.jfluidstructs.2007.02.002.

Eriksson, Lars E and Arthur Rizzi (1985). "Computer-aided analysis of the convergence to steady state of discrete approximations to the euler equations". In: *Journal of Computational Physics* 57.1, pp. 90–128. ISSN: 0021-9991. DOI: https://doi.org/10.1016/0021-9991(85)90054-3.

Fernández, Miguel Angel and Patrick Le Tallec (2002). *Linear stability analysis in fluid-structure interaction with transpiration. Part I: formulation and mathematical analysis*. Research Report RR-4570. INRIA.

Giannetti, Flavio and Paolo Luchini (2007). "Structural sensitivity of the first instability of the cylinder wake". In: *Journal of Fluid Mechanics* 581, pp. 167–197. DOI: 10.1017/S0022112007005654.

Glendinning, Paul (1994). *Stability, Instability and Chaos: An Introduction to the Theory of Nonlinear Differential Equations*. Cambridge Texts in Applied Mathematics. Cambridge University Press. DOI: 10.1017/CBO9780511626296.

Goza, Andres, Tim Colonius, and John E. Sader (2018). "Global modes and nonlinear analysis of inverted-flag flapping". In: *Journal of Fluid Mechanics* 857, pp. 312–344. DOI: 10.1017/jfm.2018.728.

Guo, C. Q. and M. P. Paidoussis (Sept. 1999). "Stability of Rectangular Plates With Free Side-Edges in Two-Dimensional Inviscid Channel Flow ". In: *Journal of Applied Mechanics* 67.1, pp. 171–176. ISSN: 0021-8936. DOI: 10.1115/1.321143.

Holmes, Philip (2007). "A SHORT HISTORY OF DYNAMICAL SYSTEMS THEORY: 1885- 2007". In:

Huerre, P. and P. A. Monkewitz (1985). "Absolute and convective instabilities in free shear layers". In: *Journal of Fluid Mechanics* 159, pp. 151–168. DOI: 10.1017/S0022112085003147.

– (1990). "Local and Global Instabilities in Spatially Developing Flows". In: *Annual Review of Fluid Mechanics* 22.1, pp. 473–537. DOI: 10.1146/annurev.fl.22.010190.002353.

Juniper, Matthew P., Ardeshir Hanifi, and Theofilis (2014). "Modal stability theory". In:

Kornecki, A., E.H. Dowell, and J. O'Brien (1976). "On the aeroelastic instability of two-dimensional panels in uniform incompressible flow". In: *Journal of Sound and Vibration* 47.2, pp. 163–178. ISSN: 0022-460X. DOI: https://doi.org/10.1016/0022-460X(76)90715-X.

Lehmann, Fritz-Olaf, Hao Wang, and Thomas Engels (Mar. 2021). "Vortex trapping recaptures energy in flying fruit flies". In: *Scientific Reports* 11. DOI: 10.1038/s41598-021-86359-z.

Lehoucq, R. B., D. C. Sorensen, and C. Yang (1998). *ARPACK Users' Guide*. Society for Industrial and Applied Mathematics. DOI: 10.1137/1.9780898719628. eprint: https://epubs.siam.org/doi/pdf/10.1137/1.9780898719628.

Leontini, Justin S. and John E. Sader (2022). "The dynamics of a rigid inverted flag". In: *Journal of Fluid Mechanics* 948, A47. DOI: 10.1017/jfm.2022.718.

Liao, James et al. (Dec. 2003). "Fish Exploiting Vortices Decrease Muscle Activity". In: *Science (New York, N.Y.)* 302, pp. 1566–9. DOI: 10.1126/science.1088295.

Lyapunov, A. M. (1892). "The general problem of the stability of motion". (in Russian). PhD thesis. University of Kharkov.

Marusic, Ivan and Susan Broomhall (2021). "Leonardo da Vinci and Fluid Mechanics". In: *Annual Review of Fluid Mechanics* 53.1, pp. 1–25. DOI: 10.1146/annurev-fluid-022620-122816.

Meliga, Philippe and Jean-Marc Chomaz (2011). "An asymptotic expansion for the vortex-induced vibrations of a circular cylinder". In: *Journal of Fluid Mechanics* 671, pp. 137–167. DOI: 10.1017/S0022112010005550.

Moulin, Johann et al. (June 2017). "A distributed Lagrangian multiplier/fictitious domain approach for coupled fluid/structure stability analysis". In: *12th ERCOFTAC SIG 33 Workshop, Progress in Flow Instablity, Transition and Control (Certosa di Pontignano, Italy)*.

Navrose and Sanjay Mittal (2016). "Lock-in in vortex-induced vibration". In: *Journal of Fluid Mechanics* 794, pp. 565–594. DOI: 10.1017/jfm.2016.157.

Negi, P. S., A. Hanifi, and D. S. Henningson (2020). "On the linear global stability analysis of rigid-body motion fluid–structure-interaction problems". In: *Journal of Fluid Mechanics* 903, A35. DOI: 10.1017/jfm.2020.685.

Nitti, A., G. De Cillis, and M.D. de Tullio (2022). "Cross-flow oscillations of a circular cylinder with mechanically coupled rotation". In: *Journal of Fluid Mechanics* 943, A30. DOI: 10.1017/jfm.2022.442.

Orrego, Santiago et al. (2017). "Harvesting ambient wind energy with an inverted piezoelectric flag". In: *Applied Energy* 194, pp. 212–222. ISSN: 0306-2619. DOI: https://doi.org/10.1016/j.apenergy.2017.03.016.

Pfister, Jean-Lou, Olivier Marquet, and Marco Carini (2019). "Linear stability analysis of strongly coupled fluid–structure problems with the Arbitrary-Lagrangian–Eulerian method". In: *Computer Methods in Applied Mechanics and Engineering* 355, pp. 663–689. ISSN: 0045-7825. DOI: https://doi.org/10.1016/j.cma.2019.06.024.

Poincaré, H. (1886). “Sur les courbes définies par les équations différentielles (IV)”. fre. In: *Journal de Mathématiques Pures et Appliquées* 2, pp. 151–218. URL: http://eudml.org/doc/234516.

Reynolds, Osborne (1883). “An Experimental Investigation of the Circumstances Which Determine Whether the Motion of Water Shall Be Direct or Sinuous, and of the Law of Resistance in Parallel Channels”. In: *Proceedings of the Royal Society of London* 35, pp. 84–99.

Schmid, Peter J. (2007). “Nonmodal Stability Theory”. In: *Annual Review of Fluid Mechanics* 39.1, pp. 129–162. DOI: 10.1146/annurev.fluid.38.050304.092139.

Schmid, Peter J. and Dan Henningson (Jan. 2001). *Stability and Transition in Shear Flows*. Vol. 142. ISBN: 9780387989853. DOI: 10.1007/978-1-4613-0185-1.

Theodorsen, Theodore (1934). “General Theory of Aerodynamic Instability and the Mechanism of Flutter”. In:

Theofilis, Vassilios (2011). “Global Linear Instability”. In: *Annual Review of Fluid Mechanics* 43.1, pp. 319–352. DOI: 10.1146/annurev-fluid-122109-160705. eprint: https://doi.org/10.1146/annurev-fluid-122109-16070.

Trefethen, Lloyd N. et al. (1993). “Hydrodynamic Stability Without Eigenvalues”. In: *Science* 261.5121, pp. 578–584. DOI: 10.1126/science.261.5121.578.

Vettori, Davide and Vladimir Nikora (Oct. 2019). “Flow-seaweed interactions of Saccharina latissima at a blade scale: turbulence, drag force, and blade dynamics”. In: *Aquatic Sciences* 81. DOI: 10.1007/s00027-019-0656-x.

Zebib, A. (1987). “Stability of viscous flow past a circular cylinder”. In: *J Eng Math* 21.1, pp. 155–165. DOI: https://doi.org/10.1007/BF00127673.

Chapter 2

AN IMMERSED BOUNDARY FRAMEWORK FOR FLUID-STRUCTURE INTERACTION

The applied scientist needs to cope increasingly with the nonlinear world and the extra mathematical sophistication that this requires. For that is where the rewards are.

Michiel Hazewinkel

This chapter outlines the immersed boundary framework that is used throughout the subsequent chapters. The first part contains a general overview of the most common techniques employed for non-linear simulations of fluid-structure interaction problems. The limitations and drawbacks of each approach are explored, with a particular focus on immersed boundary methods.

Then, the governing equations for FSI problems involving elastically mounted rigid bodies are presented and the time-stepping algorithm is described in detail. Some aspects regarding the hydrodynamic load evaluation and the forcing technique are analyzed here due to their relevance to the linearization procedure described in the next chapter.

2.1 Methods for fluid-structure interaction simulations

For the majority of FSI problems, the nonlinearity in the fluid equations and the complexity of the dynamic interplay between flow and structure make analytical solutions unattainable. Thus, to investigate the physics of the interaction, one has to resort to experiments and high-fidelity numerical simulations. That being said, the task of developing efficient and accurate computational solvers for FSI simulations poses several difficulties owing to the mutual interaction between the two systems and the displacement of the common interface.

In recent years, this topic has received great attention from the scientific community, resulting in the development of different computational strategies (Hou, Wang, and Layton, 2012; W. Kim and Choi, 2019). Broadly speaking, the universe of algorithms employed for the simulations of FSI problems can be categorized into two main approaches, namely the *monolithic* and the *partitioned* approaches. In a

monolithic framework, the fluid and solid domains are considered as a single system from a mathematical point of view, and the coupling conditions at the interface are treated implicitly by the procedure. Conversely, in partitioned (or *staggered*) methods, the fluid and structural dynamics are solved separately, each with its own algorithm, while information is transferred at the interface from one domain to the other. One of the biggest advantages of staggered approaches is that they enable the selection of the most suitable and well-validated solvers for both the fluid and structural parts. On the other hand, in a monolithic setting, the fluid and the structural systems are to be solved with the same numerical approach, despite their intrinsic differences from a mathematical perspective. As a matter of fact, in solid mechanics, the stress tensor is generally a function of the current strain state, while it is dependent upon the pressure and the instantaneous velocity gradient for a Newtonian fluid. Given the dependence of the stresses upon the deformation with respect to a reference configuration, the Lagrangian description is usually prevalent in solid mechanics. On the contrary, the large displacements that characterize fluid problems suggest an Eulerian framework as the most convenient choice. As a result, the development of a reliable monolithic solver is not an easy task, furthermore, its usage requires a significant computational effort due to the solution of a nonlinear large system at each time step. Nonetheless, the monolithic approach presents the indubious advantage that the strong coupling between the two dynamics is naturally enforced at each step, resulting in a more robust solver. By contrast, staggered solvers give rise to smaller and better-conditioned systems, but these are solved sequentially at each time step and require an appropriate technique to exchange information at the fluid-structure interface. With reference to partitioned solvers, a further distinction can be made between *weakly* and *strongly* coupled methods. In the former case, the outputs from one solver are passed as boundary conditions to the other solver in a sequential fashion, thus the two solutions do not satisfy exactly the interface conditions at the end of the time step. The correct imposition of the interface conditions is necessary when large structural motions are involved, in this case, weakly (or *loosely*) coupled methods have proven to be unstable for low solid-to-fluid density ratios (Förster, Wall, and Ramm, 2007). To overcome this difficulty and the consequential restrictions on the time step size, strongly coupled methods strictly enforce the equilibrium conditions at the common interface, typically by means of a set of sub-iterations performed at every time step. Unfortunately, the same *added mass* effect that causes the instability of the explicit loosely coupled approach deteriorates the convergence properties of implicit algorithms, as they

require more iterations to converge (Causin, Gerbeau, and Nobile, 2005). The added mass effect, which is well-known to the FSI community, is a by-product of the time lag introduced by the staggered approach. Its name derives from the fact that the fluid present in the immediate vicinity of the interface acts as an additional inertial force on the structural degrees of freedom owing to the dependence of the fluid forces upon the structural solution obtained at a previous time instant, being unknown the solution at the synchronous time.

Another typical categorization of FSI methods distinguishes between *conforming* and *non-conforming* mesh approaches. In the former, the fluid is solved on a grid or mesh that conforms to the shape of the fluid-solid interface. This approach possesses the obvious advantage of an accurate evaluation of the quantities of interest at the interface, but it requires the adaptation of the fluid mesh with every change in the position and shape of the interface. Non-conformal techniques, on the other hand, solve the fluid and structural equations on separate grids that do not necessitate common nodes as the interfacial conditions are treated as constraints. These approaches are computationally more efficient, but the complexity is moved from the grid adaptation task to the communication between the two meshes at the interface. Besides, it is easier to locally refine a body-conformal mesh rather than a regular grid.

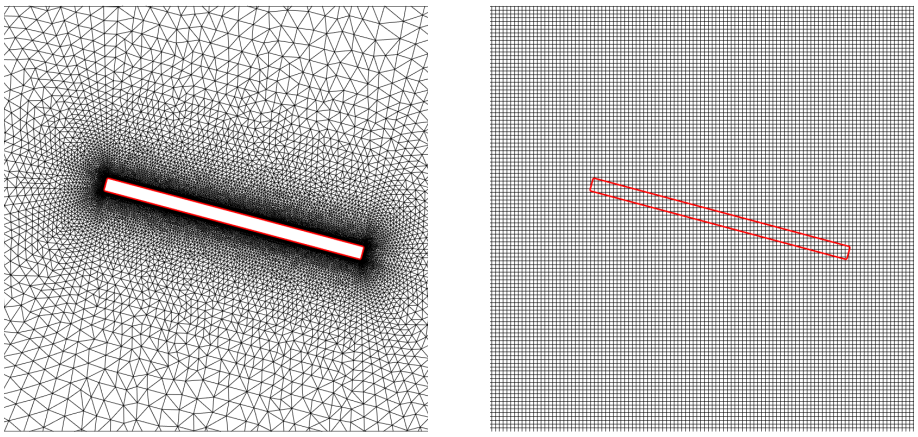

(a) Conforming (b) Non-conforming

Figure 2.1: Illustrative example of meshes/grids employed in FSI algorithms. The body-conformal mesh on the left changes as the rectangular plate moves. The plate on the right, instead, moves on a fixed grid.

2.2 Immersed Boundary Methods

Among the many approaches that fall in the category of non-body-fitted methods, the immersed boundary (IB) method has gained great popularity in recent years due to its straightforward application with complex geometries. The idea at the base of IB methods is to solve the fluid and the structure independently on separate grids, while the exchange of information between the two discretizations is typically obtained by means of a distribution of *forcing* terms in the fluid equations that mimics the presence of the interface. The forcing distribution is therefore prescribed on the fluid grid and is determined in order to enforce the correct interfacial boundary conditions.

The term *immersed boundary* was first introduced by Peskin (1972) in a seminal work on the flow around the human mitral valve. In Peskin's original formulation, the fluid equations are solved on a uniform Cartesian grid and the interface is represented as a set of Lagrangian points whose position is tracked throughout the simulation. A semi-discrete version of the Dirac delta distribution δ is introduced as a singular source term in the momentum equations to reproduce the forces exerted on the fluid by the immersed surface. In this work, the forcing terms are computed assuming an elastic behavior of the structure and selecting an appropriate constitutive law. Almost simultaneously, Viecelli (1971) proposed an extension of the Marker and Cell method to impose pressure and velocity boundary conditions on moving boundaries of arbitrary shape. The idea behind the method, referred to as ABMAC (Arbitrary Boundary Marker And Cell), is that the presence of a given interface can be represented by a pressure distribution that imposes a no-penetration condition. One drawback of Peskin's original formulation is that it is impossible to compute the forcing term in the case of a rigid body. To overcome this difficulty, Goldstein, Handler, and Sirovich (1993) developed an IB method based on a feedback scheme in which the surface force is determined directly from the local velocity field. The main drawback of this approach is that it contains two arbitrary constants that must be tuned to the flow frequencies. Besides, large values of these parameters require a small time-step size due to the stiffness of the system.

The methods developed by Peskin (1972) and Goldstein, Handler, and Sirovich (1993) come under the definition of *continuous* forcing approaches, in the sense that the forcing function is already present in the continuous equations. An alternative *discrete* formulation is possible, in which the forcing field is to be evaluated after the discretization of the equations. The primary advantage of this second formulation is the absence of user-defined parameters in the forcing function, and the conse-

quent elimination of their stability issues. Among the various IB schemes, a further distinction can be made between *direct* [1] (Fadlun et al. 2000), in the sense that the momentum forcing is imposed directly in the discretized equations to prescribe the desired velocity value at every time-step, and *indirect* forcing techniques, such as Goldstein's (1993) feedback method. In the direct-forcing formulation proposed by Fadlun et al. (2000), the body force term is evaluated by means of a linear interpolation of the velocity field at the grid points closest to the solid boundary. In this sense, the procedure reduces to a modification of the stencil to account for the position of the solid boundary. An alternative direct-forcing scheme was proposed by Uhlmann (2005), where the forcing field is computed on the Lagrangian points instead of the Eulerian grid points. In this method, the forcing field is computed by requiring the intermediate velocity of a fractional-step scheme to be equal to the local velocity on the surface of the body. The hydrodynamic load acting on a solid particle is evaluated directly from the IB force distribution, yielding an explicit coupling of the fluid and solid dynamics.

The distinguishing feature of IB methods is the way they accomplish the information exchange between the fluid and structural degrees of freedom. Since the grid points are in general not coincident, an interpolation procedure is needed to transfer the information about the velocity field at the desired location. Different techniques to reconstruct the solution near the interface give rise to distinct IB methodologies. In Uhlmann's approach (2005), for instance, the interpolation procedure is based on a regularized Dirac delta function that involves three Eulerian grid points in each direction. The spreading of the interpolation operator over a small support domain results in reduced spurious oscillations of the hydrodynamic loads, which have been observed with a sharp representation of the interface. In *sharp-interface* IB methods, such as cut-cell (Udaykumar et al. 2001) and ghost-cell (Tseng and Ferziger, 2003) formulations, the interface is represented accurately by means of a modification of the computational stencil near the immersed boundary. The accurate representation of the solid surface is a desirable feature, especially for high Reynolds number flow, but it comes at the price of introducing spurious force oscillations in the case of moving bodies. Basically, these oscillations originate from the change of role of the Eulerian points close to the surface from one time-step to the other (Uhlmann, 2003). As a grid point comes out of the solid phase, for instance, it carries no information about the fluid phase at the previous time-step, hence providing inaccurate values for the temporal discretization of the flow variables. Motivated by

[1] Here the attribute *direct* is used as in (Fadlun et al. 2000)

the need for smoother hydrodynamic loads, Vanella and Balaras (2009) improved Uhlmann's approach (2005) by introducing the use of the Moving Least Squares (MLS) approximation to construct the Eulerian-Lagrangian transfer function.
Nowadays IB methods are widely employed to model complex FSI problems involving large structural displacements. In presence of significant boundary deformations, indeed, the use of a mesh-conforming framework, such as the Arbitrary Lagrangian-Eulerian (ALE) method (Souli, Ouahsine, and Lewin, 2000), would produce severe mesh distortions in the proximity of the interface, thus limiting its application to problems involving small structural displacements. In addition to the ease in handling multibody configurations, another important advantage offered by IB methods is their simple implementation on stationary Cartesian grids, thus allowing easier parallelization and enabling the use of fast algebraic solvers.
Despite the many benefits IB techniques offer, there are some drawbacks to consider

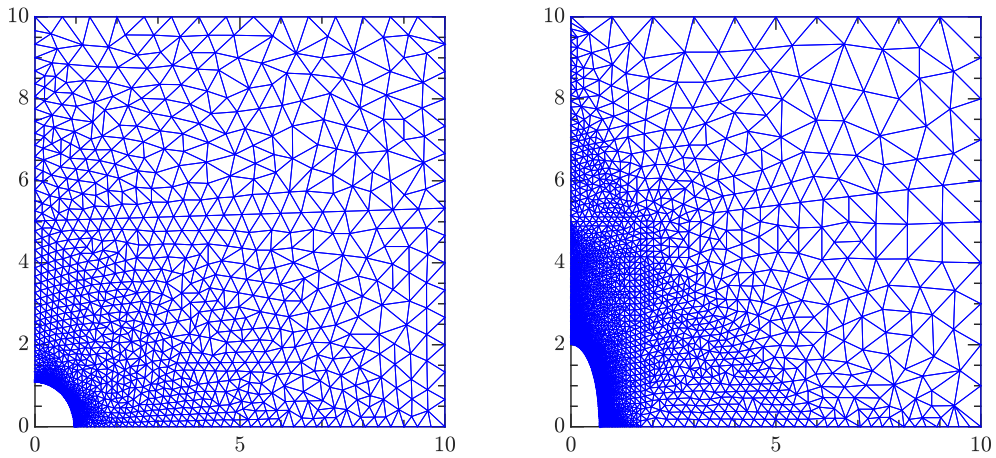

(a) (b)

Figure 2.2: Example of the mesh adaptation that results from body-conformal approaches. Specifically, the initial mesh (a) is updated (b) to follow the movement of the interface. The meshes shown above have been used by the author in the computation of the steady states for the problem of a gas bubble in a straining flow described in Chapter 5.

as well. One downside of these methods is that they solve the momentum equations also for the grid points inside the solid boundaries. With increasing Reynolds numbers, and consequently the number of discretization cells required to resolve the small flow scales, solving for the inner points constitutes a computational burden that cannot be neglected. Besides, the cost required to achieve high resolution near

the body increases significantly with uniform or stretched grids. As a matter of fact, with Cartesian grids, the grid refinement is propagated with grid lines and a high density of cells is obtained also far from the body. To alleviate this computational burden, a local refinement is needed (de Tullio, De Palma, et al. 2007). Another crucial point about IB methods is the evaluation of surface stresses at the interface, which is a nontrivial task when the solid and fluid grid points do not coincide, as is generally the case. This aspect is further discussed in section 2.4.

Without any pretense of being exhaustive, this short review has served as an introduction to the basic concepts of the IB methodology that is used in the following chapters. For an overview of the various IB methodologies, the reader is referred to the review of Mittal and Iaccarino (2005). In the next section, after introducing the governing equations for the fluid-structure model, the IB framework method adopted to handle the moving surfaces is presented in detail.

2.3 Governing equations

The focus here is on homogeneous incompressible viscous flows that interact with elastically mounted rigid bodies, although the formulation derived for the solver remains very general and utilizable with various structural models (and solvers). The dynamics of the fluid system is governed by the Navier-Stokes and continuity equations, reported here in their non-dimensionalized form:

$$\frac{\partial \boldsymbol{u}}{\partial t} + \boldsymbol{u} \cdot \nabla \boldsymbol{u} = -\nabla p + \frac{1}{Re}\nabla^2 \boldsymbol{u} + \boldsymbol{f}, \tag{2.1a}$$

$$\nabla \cdot \boldsymbol{u} = 0. \tag{2.1b}$$

In the equations above, $\boldsymbol{u}$ and p denote the fluid velocity and pressure , respectively. The body force term $\boldsymbol{f}$, in the absence of other external fields, corresponds to the IB body-force field. The system of equations (2.1) is closed by appropriate boundary conditions related to the specific configuration to be studied. Fluid variables have been made dimensionless by considering a reference length L_r and velocity scale U_r, and the Reynolds number is defined as $Re = \dfrac{U_r L_r}{\nu}$, with ν the kinematic viscosity of the fluid. The time is non-dimensionalized with respect to the reference value $\tau_r = L_r/U_r$.

The equations that govern the motion of an elastically mounted rigid body, with the elastic center coincident with the center of mass, and subject to structural damping and hydrodynamic forces are reported below:

$$\ddot{\tilde{x}}_i + \frac{c_i}{A_i \rho_s}\dot{\tilde{x}}_i + \frac{k_i}{A_i \rho_s}\left(\tilde{x}_i - \tilde{x}_i^{eq}\right) = F_i, \quad i = 1, .., n_{DOF}. \tag{2.2}$$

The above equation describes the temporal evolution of a simple damped oscillator, where $\tilde{x}_i$ represents the position of the i–th degree of freedom (DOF) , $\tilde{x}_i^{eq}$ being the equilibrium position of the spring for the same DOF, c_i and k_i are the damping and stiffness coefficients, respectively, ρ_s is the density of the solid and F_i is the sum of all external loads acting on the i–th DOF. For two-dimensional problems, each solid body has $n_{DOF} = 3$ degrees of freedom, namely the two components of the displacement vector and a rigid rotation around the center of mass. The inertia associated with the i–th DOF is given by $\rho_s A_i$, where the parameter A_i is used to indicate the cross-sectional area (for the translational DOFs) or the moment of area of the cross-section (for the rotational DOF). The dot notation is used to indicate time derivatives.

After non-dimensionalization, the equation for the i–th DOF reads:

$$\ddot{x}_i + \frac{\sigma_i}{A_i^* \rho^*}\dot{x}_i + \frac{\xi_i}{A_i^* \rho^*}\left(x_i - x_i^{eq}\right) = C_i, \quad i = 1, .., n_{DOF} \tag{2.3}$$

where the solid variables have been made dimensionless by means of the bulk parameters of the flow field .

The non-dimensional cross-sectional area is defined as $A^* = A/L_{ref}^2$, while the non-dimensional moment of area corresponds to the second moment of area with respect to the centroidal axis divided by the fourth power of L_r. The parameter ρ^* is the ratio of solid-to-fluid densities, $\rho^* = \rho_s/\rho_f$, with ρ_f being the density of the fluid phase. The non-dimensional linear damping (σ_i) and stiffness (ξ_i) coefficients are defined as follows:

$$\sigma_{x,y} = \frac{c_{x,y}}{\rho_f U_{ref} L_{ref}}, \quad \sigma_\theta = \frac{c_\theta}{\rho_f U_{ref} L_{ref}^3}, \quad \xi_{x,y} = \frac{k_{x,y}}{\rho_f U_{ref}^2}, \quad \xi_\theta = \frac{k_\theta}{\rho_f U_{ref}^2 L_{ref}^2}.$$

In the definitions above, the subscripts x and y are used to indicate the translational DOFs, while the subscript θ indicates the rotation around an axis perpendicular to the xy–plane and passing through the center of mass. The coefficient C_i represents the non-dimensional force (or torque) acting upon the $i-$th DOF, given by:

$$C_{x,y} = \frac{F_{x,y}}{\rho_f U_{ref}^2 L_{ref}}, \quad C_\theta = \frac{F_\theta}{\rho_f U_{ref}^2 L_{ref}^2}.$$

The coupling between the two systems of equations (2.3) and (2.1) is accomplished via the forcing term $\boldsymbol{f}$ in the momentum equations that represents the action of the solid boundaries on the flow, and the lift and torque coefficients above defined, which give the hydrodynamic load, in absence of other external force fields, such as gravity, that act on the body.

2.4 Time-stepping algorithm

The finite-difference solver employed in this work (Nitti et al. 2020) integrates in time the Navier-Stokes equations (2.1) through a semi-implicit procedure, where the convective and viscous terms in the momentum equations (2.1a) are discretized by a third-order Runge-Kutta (RK3) and a Crank-Nicolson (CN) scheme, respectively. Each substep is resolved by means of a classic fractional-step method (Chorin, 1968), in which the coupling between the flow and the structure is obtained by means of Uhlmann's direct-forcing IB technique (Uhlmann, 2005). This method introduces an additional force term into the right-hand side (RHS) of eq. (2.1a) to take into account the effect of the solid boundaries. The method is outlined below.

At the beginning of the $(k+1)$–th substep, a preliminary velocity field $\hat{\boldsymbol{u}}$ is evaluated by making use of known quantities from the previous time steps

$$\hat{\boldsymbol{u}} = \boldsymbol{u}^k + \Delta t \left[-\alpha^k \nabla p^k + \beta^k \left(\boldsymbol{u}\cdot\nabla\boldsymbol{u}\right)^k + \gamma^k \left(\boldsymbol{u}\cdot\nabla\boldsymbol{u}\right)^{k-1} + \frac{\alpha^k}{Re}\nabla^2\boldsymbol{u}^k \right], \tag{2.4}$$

where Δt is the total time step and the coefficients for the three Runge-Kutta substeps are the same as in (Mohan Rai and Moin, 1991):

$$\alpha = \left(\frac{8}{15}, \frac{2}{15}, \frac{5}{15}\right), \quad \beta = \left(\frac{32}{60}, \frac{25}{60}, \frac{45}{60}\right), \quad \gamma = \left(0, \frac{-17}{60}, \frac{-25}{60}\right).$$

The preliminary velocity $\hat{\boldsymbol{u}}$ is then used to compute the IB forcing term $\boldsymbol{f}$, which is in turn employed to advance in time the intermediate velocity field $\tilde{\boldsymbol{u}}$,

$$\frac{\tilde{\boldsymbol{u}} - \boldsymbol{u}^k}{\Delta t} = -\alpha^k \nabla p^k + \beta^k \left(\boldsymbol{u}\cdot\nabla\boldsymbol{u}\right)^k + \gamma^k \left(\boldsymbol{u}\cdot\nabla\boldsymbol{u}\right)^{k-1} + \frac{\alpha^k}{2Re}\nabla^2\left(\tilde{\boldsymbol{u}} + \boldsymbol{u}^k\right) + \boldsymbol{f}\left(\hat{\boldsymbol{u}}\right). \tag{2.5}$$

The evaluation of the preliminary velocity field involves only quantities already computed in the previous time step, hence it requires a low-cost explicit computation. Furthermore, its value is contained in the RHS of eq. (2.5), therefore the evaluation of the forcing field upon the preliminary velocity does not increase the computational cost compared to its evaluation upon the velocity at the previous time-step (J. Kim, D. Kim, and Choi, 2001). The details about the IB procedure adopted to evaluate $\boldsymbol{f}$ are provided in section 2.4, after a brief discussion about the coupling between the fluid and the solid dynamics.

After the evaluation of the forcing term, a Helmholtz equation is to be solved for the velocity increment $\Delta\tilde{\boldsymbol{u}}$,

$$\left(1 - \frac{\alpha^k \Delta t}{2Re}\right)\Delta\tilde{\boldsymbol{u}} = \hat{\boldsymbol{u}} - \boldsymbol{u}^k + \Delta t\,\boldsymbol{f}, \tag{2.6}$$

with

$$\Delta\tilde{\boldsymbol{u}} = \tilde{\boldsymbol{u}} - \boldsymbol{u}^k. \tag{2.7}$$

The fluid equations are solved on a Cartesian staggered grid (Welch et al. 1965), where the velocity components and the IB forcing terms are located at face centers, and the scalar quantities are defined at the centers of the cells. The spatial derivatives are approximated by means of standard second-order central finite differences. In this way, the staggered grid allows for compact stencils and does not require boundary conditions for the pseudo-pressure φ (Orlandi, 2001).

The solution of eq. (2.6) would involve the inversion of a large sparse matrix. This is avoided by adopting an approximate factorization procedure (Briley and McDonald, 1980) to reduce the large banded matrix associated with the implicit treatment of viscous terms to the product of two tridiagonal matrices. This operation allows the use of fast tridiagonal solvers, such as the Thomas algorithm, leading to a saving in computational time. The solution of eq. (2.5) gives an intermediate velocity field that does not satisfy the continuity equation. To enforce the continuity of the final velocity $\boldsymbol{u}^{k+1}$, a pseudo-pressure field φ is introduced in such a way that the expression for the final velocity reads

$$\boldsymbol{u}^{k+1} = \tilde{\boldsymbol{u}} - \alpha^k \Delta t \nabla\varphi. \tag{2.8}$$

Taking the divergence of the discrete fields in (2.8) and requiring the divergence of $\boldsymbol{u}^{k+1}$ to be zero everywhere, a Poisson equation is obtained for φ:

$$\nabla^2\varphi = \frac{\nabla\cdot\tilde{\boldsymbol{u}}}{\alpha^k\Delta t}. \tag{2.9}$$

The discretized Poisson equation is solved to machine precision using a direct method based on the eigendecomposition of the coefficient matrices (Haidvogel and Zang, 1979). On a fixed grid, the decomposition procedure must be done once and for all since the matrix entries do not change with time. The direct solution of eq. (2.9) is needed to enforce the continuity condition with a tight tolerance at each time step and is accomplished by using standard LAPACK (Anderson et al. 1990) routines. For computational domains with different numbers of cells in the two directions, it is preferred to solve for N_x tridiagonal matrices of order N_y, where x is the direction with more grid points.

Once eq. (2.9) is solved for the scalar field φ, the pressure can be updated (if needed) as

$$p^{k+1} = p^k + \varphi - \frac{\nabla\cdot\tilde{\boldsymbol{u}}}{2Re}. \tag{2.10}$$

For incompressible flow problems, indeed, the pressure, or in this case the related scalar variable φ, is used as a Lagrangian multiplier to impose the divergence-free condition upon the velocity field.

Before describing the possible coupling techniques for the fluid and the solid dynamics, there is another important aspect to be mentioned. The forcing term in eq. (2.5), is evaluated based on the preliminary velocity $\hat{\boldsymbol{u}}$ but is applied to the intermediate velocity $\tilde{\boldsymbol{u}}$. Given the semi-implicit nature of the time-stepping algorithm, the boundary conditions of the fluid-solid interface may not be satisfied after the solution of the Helmholtz equation (2.6). Furthermore, given the time-splitting nature of the fractional-step approach, the imposition of the boundary conditions at the interface is subsequently spoiled in the corrector step to enforce local continuity (Fadlun et al. 2000).

However, the modification of the interface velocity caused by the correction step can be minimized through a repetition of the forcing procedure after the solution of the Helmholtz equation. Specifically, once eq. (2.6) has been solved, the interpolation procedure described in section 2.4 is used to compute an updated IB forcing term, then the intermediate velocity is modified accordingly. The iterative procedure is described below:

for $s := 1, n_s$ **do**

$$\boldsymbol{f}_s^{n+1/2} = \boldsymbol{f}\left(\tilde{\boldsymbol{u}}_{s-1}^{n+1}\right)$$

$$\tilde{\boldsymbol{u}}_s^{n+1} = \hat{\boldsymbol{u}} + \Delta t\, \boldsymbol{f}_s^{n+1/2}$$

end for

where n_s is a pre-defined number of iterations of the forcing procedure. Observations have shown that the discrepancy between the interpolated final fluid velocity and the local body velocity is effectively reduced with three to five iterations of the forcing procedure (Breugem, 2012), up to a root-mean-square error that goes as $\sim O(10^{-5})$ of the reference flow velocity. Within the present method, the local difference between the interpolated fluid velocity and the solid velocity employed in the forcing stage is measured downstream of the time scheme, and its Root Mean Square is evaluated over the set of Lagrangian markers (section 2.4). In presence of moving surfaces, the root-mean squre error (RMSE) is found to be $\sim O(10^{-4})$ of the reference velocity (see fig. 11 of (Nitti et al. 2020)).

The code is a collection of Fortran90 routines, and the flow solver is parallelized by means of MPI libraries.

Time integration of rigid-body dynamics

The equations of motion for the rigid body are integrated in time by means of a CN scheme. Within this staggered approach, at each time step, the fluid and the structural systems are solved in a sequential fashion: first, a low-order extrapolation for the fluid-solid interface position and velocity is required to compute the IB forcing terms and advance the flow field in time; then the coupling between fluid and rigid-body dynamics is accomplished using the Eulerian load distribution $\boldsymbol{f}$ coming from the IB procedure to obtain the total force and moment integrals (Lācis, Taira, and Bagheri, 2016; Lai and Peskin, 2000) in the RHS of Newton's equations (2.3). This procedure avoids the integration of pressure and viscous stresses on the contour of the body, circumventing the need for a reconstruction procedure. More details about the hydrodynamic load evaluation are given in section 2.4.

Weak and strong coupling between fluid and rigid body dynamics

At this point, a distinction must be done between explicit and implicit fluid-structure coupling schemes. When an explicit formulation is adopted to couple the fluid and rigid-body dynamics, a specific time level for the IB forcing term should be introduced.

Weakly coupled solver Specifically, the forcing function in the RHS of eq. (2.5) employed to advance in time the solution of one time-step, from n to $n+1$, is evaluated by using the structural solution obtained at n. Therefore, when the explicit coupling approach is used, a time level $n+1/2$ for the IB forcing is introduced. Namely, the fluid solution at $n+1$ depends upon $\boldsymbol{f}^{n+1/2}\left(\boldsymbol{x}_B^{n+1/2}\right)$, where $\boldsymbol{x}_b^{n+1/2}$ is a predictor for the local interfacial displacement and velocity. For an undamped system, the structural solution is then advanced in time following a CN scheme

$$\left(M+\frac{1}{2}K\right)\left(\boldsymbol{x}_B^{n+1}-\boldsymbol{x}_B^{n}\right)+K\boldsymbol{x}_B^{n}=\boldsymbol{C}^{n+1/2}, \tag{2.11}$$

where the hydrodynamic load $\boldsymbol{C}^{n+1/2}$ is given by the integral of the forcing terms $\boldsymbol{f}^{n+1/2}$ previously computed. In eq. (2.11), vector $\boldsymbol{x}_B$ collects the structural displacements and velocities, while M and K are, respectively, the mass and stiffness matrices of the body.

The partitioned approach described above allows for fast FSI computations, however, its staggered nature reduces the temporal accuracy of the solution due to the

time lag introduced in the IB coupling procedure. Furthermore, loosely coupled solvers are unstable for small solid-to-fluid density ratios ρ^* (Causin, Gerbeau, and Nobile, 2005; Förster, Wall, and Ramm, 2007) owing to the added-mass effect .

Iterative procedure To overcome these stability issues, an implicit approach is needed. The one proposed in this work preserves the partitioned nature of the solver by performing a set of iterations of the main loop. Iterative procedures enable the decoupling of the fluid and structural steps, thus allowing one to use already available solvers for both parts while still describing their instantaneous mutual interaction. The simple iterative procedure is described below. To advance the solution of one time-step, from n to $n+1$, the following loop is repeated until the desired convergence on the structural degrees of freedom is reached:

while $\|\boldsymbol{x}_{B,l+1}^{n+1} - \boldsymbol{x}_{B,l}^{n+1}\|_\infty > tol$ **do**

$$\boldsymbol{f}_l^{n+1} = \boldsymbol{f}\left(\boldsymbol{u}_l^{n+1}, \boldsymbol{x}_{B,l}^{n+1}\right)$$

$$\boldsymbol{u}_{l+1}^{n+1} = FS\left(\boldsymbol{u}_l^{n+1}, \boldsymbol{f}_l^{n+1}\right)$$

$$\boldsymbol{x}_{B,l+1}^{n+1} = SS\left(\boldsymbol{x}_{B,l}, \boldsymbol{f}_l^{n+1}\right)$$

end while

In the above equations, the flow and structural solvers are denoted by FS and SS, respectively. The subscripts l and $l+1$ refer to the iteration number, while the superscripts indicate the time level. With the scheme described above, the output from one solver is used as an input for the other solver and viceversa. The time lag of the explicit procedure is eliminated since both the solid velocity and displacements are treated implicitly. The stopping criterion is based on the infinity norm of the structural DOFs. Specifically, iterations stop when the norm reaches a prescribed tolerance, or a limiting number of iterations is reached.

It has to be noted, however, that iterative algorithms feature convergence difficulties for low values of the density ratio, due to the dominance of the fluid force over the solid inertia (Baek and Karniadakis, 2012). Furthermore, with the iterative coupling procedure, the computational cost per time step increases considerably.

In the above-illustrated procedure, the time level notation has been retained also for the IB forcing term, to keep the notation consistent with the explicit procedure. However, within the implicit framework, the forcing term does not necessitate a time level since it can be viewed as a Lagrange multiplier (Lācis, Taira, and Bagheri, 2016) required to impose the boundary conditions at the interface, just as the pseudo-

pressure φ is used to enforce the divergence-free constraint.

Hydrodinamic load evaluation

The accurate calculation of surface stresses and forces acting on the immersed bodies is a crucial aspect of non-conforming methods. The expression for the hydrodynamic load acting on a rigid body reads

$$\boldsymbol{F}^{ext} = \rho_f \oint_{\Gamma_B} \boldsymbol{\tau} \cdot \boldsymbol{n} d\gamma, \tag{2.12}$$

$$\boldsymbol{C}^{ext} = \rho_f \oint_{\Gamma_B} \boldsymbol{r} \wedge (\boldsymbol{\tau} \cdot \boldsymbol{n})\, d\gamma, \tag{2.13}$$

where $\boldsymbol{F}^{ext}$ and $\boldsymbol{C}^{ext}$ represent, respectively, the vectors of hydrodynamic forces and moments applied to a solid body occupying a volume S_B (a surface in a two-dimensional domain). Γ_B is the contour of the body, $\boldsymbol{n}$ is the outward-pointing unit normal vector, $\boldsymbol{\tau}$ is the stress tensor, and $\boldsymbol{r}$ is the position vector of surface points with respect to the center of mass. The evaluation of the above-defined surface integrals would require knowing the flow quantities at the interface. This is not the case with non-conformal approaches, since Eulerian grid points generally do not coincide with the Lagrangian markers, therefore the direct computation of integrals (2.12) necessitates an interpolation of the entries of the stress tensor onto the interface.

To overcome these difficulties and avoid the estimation of inaccurate gradients, in this method the forcing term in the momentum equations (2.1a) is used to evaluate the stresses at the interface. Following Uhlmann (2005), the hydrodynamic loads can be evaluated from a momentum balance over the fluid encompassed by Γ_B

$$\rho_f \oint_{\Gamma_b} \boldsymbol{\tau} \cdot \boldsymbol{n} d\gamma = \frac{d}{dt} \rho_f \oint_{S_B} \boldsymbol{u} dS - \rho_f \int_{S_B} \boldsymbol{f}_V dS - \rho_f \oint_{\Gamma_B} \boldsymbol{f}_S d\gamma, \tag{2.14}$$

where $\boldsymbol{f}_V$ and $\boldsymbol{f}_S$ represent the contribution of volume and surface forces, respectively, acting on the fluid. An analogous equation can be derived for the angular momentum.

Within an IB framework, and in absence of other external fields, the second integral in the RHS of (2.14) is simply the integral of the IB source term in the momentum equations. The first term in the RHS of (2.14), instead, gives the linear acceleration of the fluid enclosed by Γ_B, which needs to be accounted for in the evaluation of $\boldsymbol{F}^{ext}$. A simple approach to do so was presented by Uhlmann (2005), where it is

assumed a rigid-body motion for the fictitious fluid inside the body. In this way, the coefficients of the mass matrix of the body are modified to take into account the inertia of the fictitious fluid. As pointed out by Kempe and Fröhlich (2012), this approach leads to a singularity for $\rho_s = \rho_f$. Besides, the assumption of rigid motion inside the solid could be questioned especially in problems involving the rotation of the body. Therefore, the approach followed here is the one described by Lācis, Taira, and Bagheri (2016). Specifically, it is based on the direct account of the fluid inertia within the body, evaluated by means of a first-order approximation of the time derivative of the volume integral in (2.14)

$$dQ_x^{n+1/2} = \frac{Q_x u^n - Q_x u^{n-1}}{\Delta t}, \tag{2.15}$$

where $dQ_x^{n+1/2}$ is the discrete fluid inertia at the time level $n + 1/2$ for the coordinate direction x, u is the component of velocity in the same direction, and Q_x is the numerical evaluation of the volume integral, obtained through a second-order midpoint quadrature rule

$$Q_x u^n = \sum_{ij} u_{ij}^n \alpha_{ij} \Delta x_i \Delta y_j. \tag{2.16}$$

In the above equation, the subscripts of the cell spacings Δx_i and Δy_j are necessary for non-uniform stretched grids. The coefficient α_{ij} in (2.16) gives the fraction of the cell volume occupied by the solid a time n, and is computed as

$$\alpha_{ij} = \frac{\sum_{p=1}^{4} -\zeta_p H\left(\zeta_p\right)}{\sum_{p=1}^{4} \left|\zeta_p\right|}, \tag{2.17}$$

where H is the Heaviside step function, and ζ is the distance from the surface of the body of the four corners of cell (i, j). The sign of ζ is assumed to be positive for points outside the body. An analogous expression can be derived for the rotational inertia.

To obtain α_{ij} and $Q_x u^n$, it is necessary to know the actual position of each cell with respect to the interface. This is trivial for rigid bodies whose surfaces can be described as a locus of points in the Euclidean plane, such as ellipses. For more complex geometries, this task can be accomplished by means of a ray-tracing algorithm (O'Rourke, 1998).

The effect of the fictitious fluid inside the bodies is negligible for high-density ratios ρ^* for which the solid inertia dominates over the fluid contribution. For comparable values of ρ_s and ρ_f, its effect on the accuracy of the results has been evaluated

on the VIV case of a spring-mounted cylinder in an open flow, free to oscillate in the cross-flow direction, at $Re = 60$ for $\rho^* = 5$ and $\rho^* = 2.5$. In Figure 2.3 are reported the time traces of the vertical displacement of a cylinder with $\rho^* = 5$ (a) and $\rho^* = 2.5$ (b) obtained with and without the correction for the fictitious fluid inside the cylinder, respectively. In both cases, the two simulations start from the same steady solution, and no initial perturbation is added to the field. The simulations are performed with a time-step size adapted to get keep the Courant-Friedrichs-Lewy (CFL) number equal to 0.1. The selected Reynolds number of the simulations is bigger than the linear instability threshold for an oscillating cylinder, therefore numerical disturbances trigger an unstable mode and the cylinder starts oscillating. The purpose of the validation is to evaluate the effect of the fictitious fluid upon the initial growth of the oscillation amplitude. The results reported in Figure 2.3 show a good agreement between the time evolutions with and without the inner-flow correction for the cases considered. Figure 2.4, instead, shows the effect of the repetition of the forcing procedure, as described in section 2.4, on the computed hydrodynamic loads. Six simulations have been carried out starting from the same initial condition to evaluate the influence of the number of forcing iterations n_s on the hydrodynamic forces calculated according to (2.14). The configuration chosen is the uniform flow past a fixed cylinder at $Re = 100$, for which vortex shedding occurs and three-dimensional modes do not affect the dynamics. According to the results shown in Figure 2.4, there seems to be a small variation of the lift coefficient with n_s, while it is necessary to iterate the forcing procedure at least five times to get an almost independent drag coefficient. This result is not surprising since the inflow velocity is aligned along the x direction. This effect is present also without the inner flow correction procedure given by (2.15), as shown in Figure 2.5. In Figure 2.6, instead, are reported the time histories of the RMSE of the no-slip condition over the set of Lagrangian markers, for the same flow. As can be seen, the difference between structural velocity and interpolated fluid velocity, integrated over the interface, is always kept as a $O(10^{-4})$ fraction of the free-stream velocity. At first, the error diminishes appreciably with the increase of n_s, but the decrease is negligible for $n_s > 3$, suggesting that further increasing n_s is useless for the accuracy of the computation.

Immersed boundary procedure

The boundary conditions at the fluid-structure interface are imposed on the intermediate velocity field $\tilde{\boldsymbol{u}}$ using a direct-forcing immersed boundary technique.

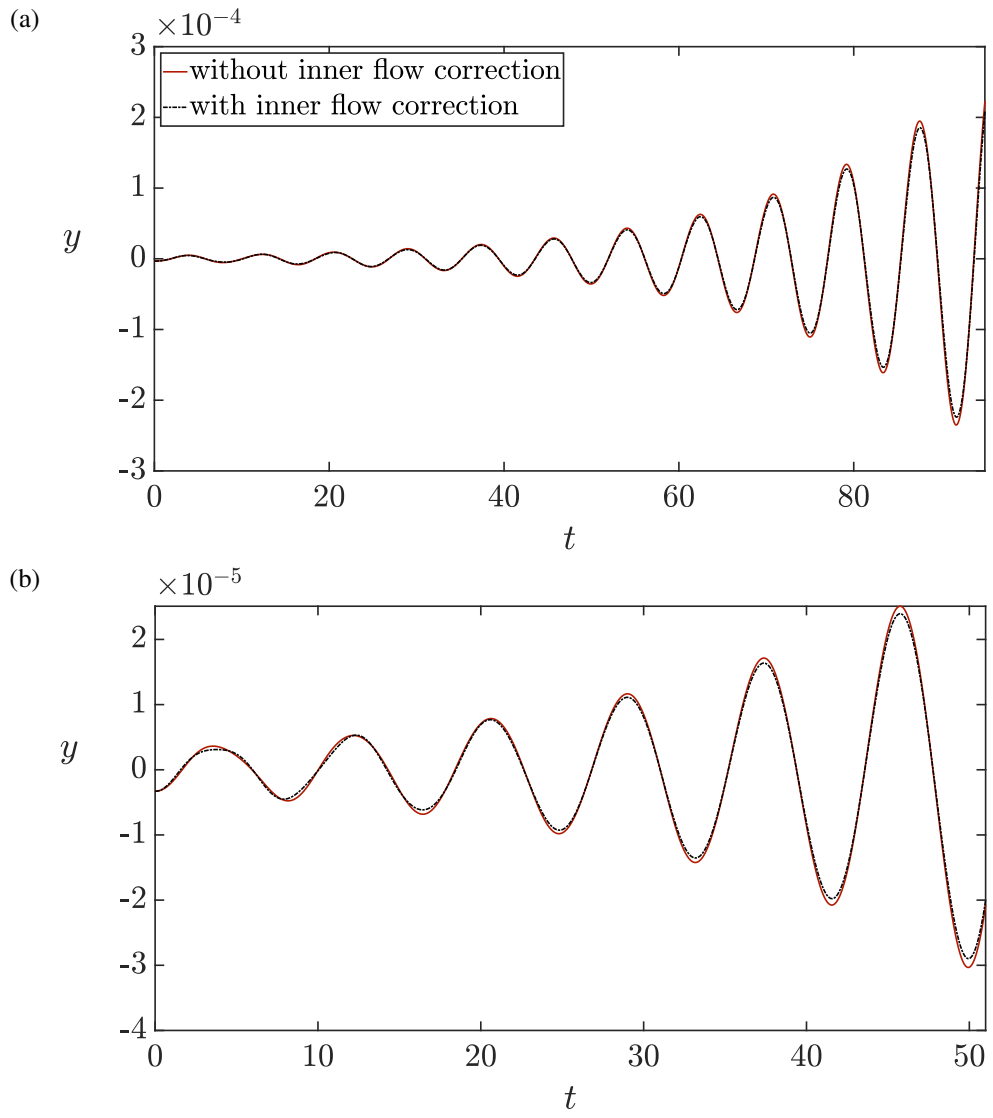

Figure 2.3: Vertical displacement of a spring-mounted rigid cylinder in a cross flow at $Re = 60$, with and without the inner flow correction for different values of the density ratio: (a) $\rho^* = 5$ and (b) $\rho^* = 2.5$.The simulations have been conducted at constant $CFL = 0.1$.

Following Uhlmann (2005), body-force terms are computed over a set of suitably spaced Lagrangian markers laying on the immersed surface. Each velocity component is interpolated at the Lagrangian markers via an MLS approximation (Vanella and Balaras, 2009):

$$\hat{V}_i(\boldsymbol{x}^l) = \boldsymbol{\Psi}_i^{\mathsf{T}}(\boldsymbol{x}^l)\hat{\boldsymbol{u}}_i, \tag{2.18}$$

where $\hat{\boldsymbol{u}}_i$ is the array that collects the i–th velocity component at the face centers within the support domain of each Lagrangian marker and $\hat{V}_i$ is the i–th velocity component at the Lagrangian position $\boldsymbol{x}^l$. In two dimensions, the minimum number

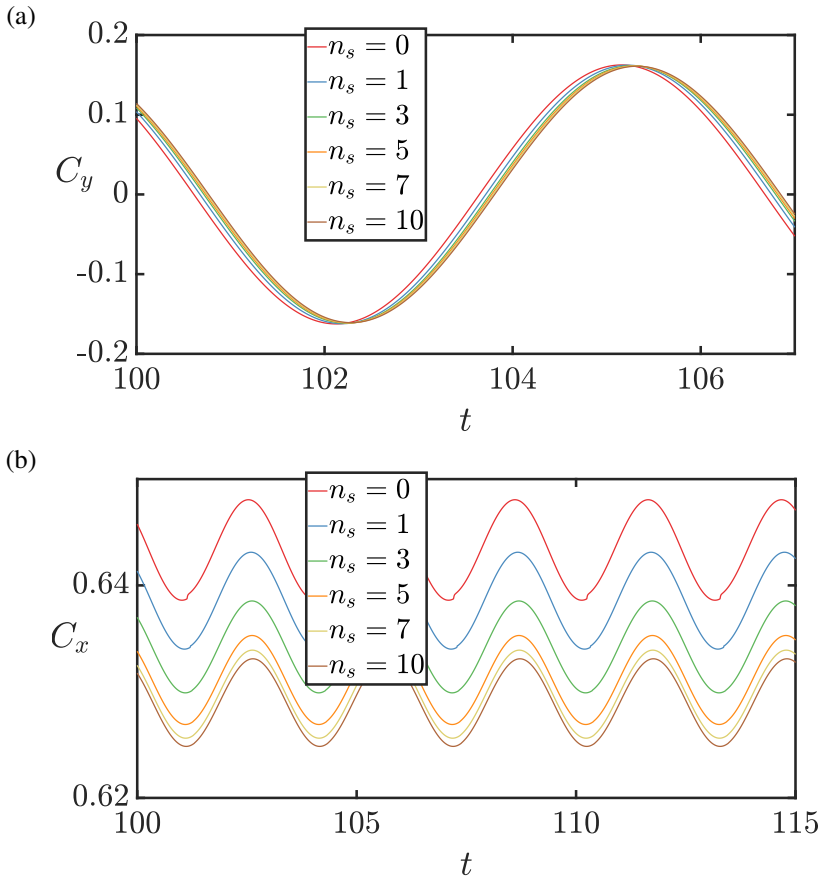

Figure 2.4: Time histories of the non-dimensional lift C_y and drag C_x forces for a fixed cylinder in a uniform flow at $Re = 100$. The calculations have been performed with a different number of iterations n_s of the forcing procedure after the solution of the Helmholtz equation.

of grid cells n_e contained in the support domain is equal to 9. The linear operator $\boldsymbol{\Psi}_i^{\mathsf{T}}(\boldsymbol{x}^l)$ is the MLS transfer function for the i–th velocity component, defined as

$$\boldsymbol{\Psi}^{\mathsf{T}}(\boldsymbol{x}^l) \equiv \boldsymbol{p}^{\mathsf{T}}(\boldsymbol{x}^l)(\boldsymbol{A}(\boldsymbol{x}^l))^{-1}\boldsymbol{B}(\boldsymbol{x}^l), \tag{2.19}$$

where

$$\begin{aligned}
&\boldsymbol{p}^{\mathsf{T}}(\boldsymbol{x}^l) = [1, x^l, y^l], \\
&\boldsymbol{A}(\boldsymbol{x}^l) = \sum_{k=1}^{n_e} W\left(\boldsymbol{x}^l - \boldsymbol{x}^k\right) \boldsymbol{p}\left(\boldsymbol{x}^k\right) \boldsymbol{p}^{\mathsf{T}}\left(\boldsymbol{x}^k\right), \\
&\boldsymbol{B}(\boldsymbol{x}^l) = \left[W(\boldsymbol{x}^l - \boldsymbol{x}^1)\boldsymbol{p}(\boldsymbol{x}^1) \ldots W(\boldsymbol{x}^l - \boldsymbol{x}^{n_e})\boldsymbol{p}(\boldsymbol{x}^{n_e})\right].
\end{aligned} \tag{2.20}$$

The weight function $W(\boldsymbol{x}^l - \boldsymbol{x}^k)$, used in the definition of matrices $\boldsymbol{A}$ and $\boldsymbol{B}$, plays the role of a convolution kernel. Different kinds of weighting functions can be used in (2.20), provided that they are adequately smooth, respect the partition

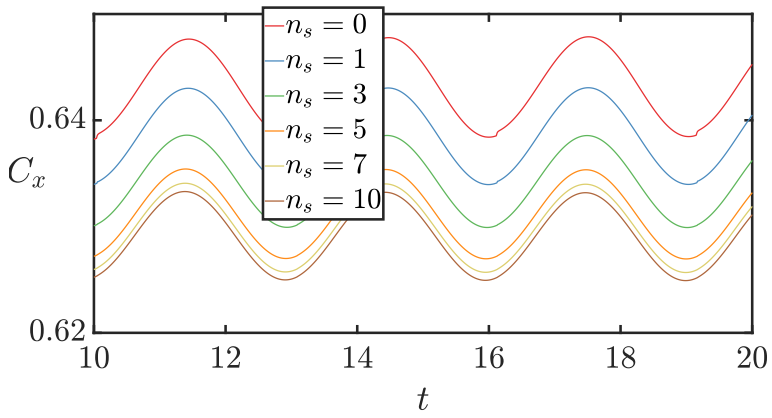

Figure 2.5: Time traces of the drag coefficient C_x of a fixed cylinder immersed in a uniform flow at $Re = 100$. The image shows the variation of C_x as the number of iterations of the forcing procedure is increased, in absence of the correction for the inner fluid inertia.

of unity and compatibility properties, and generate shape functions that reproduce exactly the linear polynomial contained in their basis (Vanella and Balaras, 2009). Two commonly used weighting functions are the cubic spline and the exponential function. Indeed, both the weightings hold comparable results and possess the desirable property of monotonicity. Cubic splines weight functions are defined as

$$W(\boldsymbol{x} - \boldsymbol{x}^k) = \begin{cases} \frac{2}{3} - 4r_k^2 + 4r_k^3, & \text{for } r_k \leq 0.5 \\ \frac{4}{3} - 4r_k + 4r_k^2 - \frac{4}{3}r_k^3, & \text{for } 0.5 < r_k \leq 1.0 \\ 0, & \text{for } r_k > 1.0 \end{cases} \tag{2.21}$$

where $r_k = |\boldsymbol{x} - \boldsymbol{x}^k|/r_i$, and r_i is the size of the support domain in the i-th direction. The exponential function has the following form

$$\mathrm{W}(\boldsymbol{x} - \boldsymbol{x}^k) = \begin{cases} e^{-(r_k/\iota)^2}, & \text{for } r_k \leq 1 \\ 0, & \text{for } r_k > 1 \end{cases} \tag{2.22}$$

where ι is a shape parameter. For the results presented in this work, the exponential function is used with $\iota = 0.3$.

After the interpolation step for the velocity, a volume force component is computed for each Lagrangian marker l,

$$F_i^l = \frac{V_i^l - \hat{V}_i(\boldsymbol{x}^l)}{\Delta t}, \tag{2.23}$$

where V_i^l is the $i-$th component of velocity to be imposed at the interface and Δt is the time-step of the numerical scheme. Finally, the forcing term to be added to the

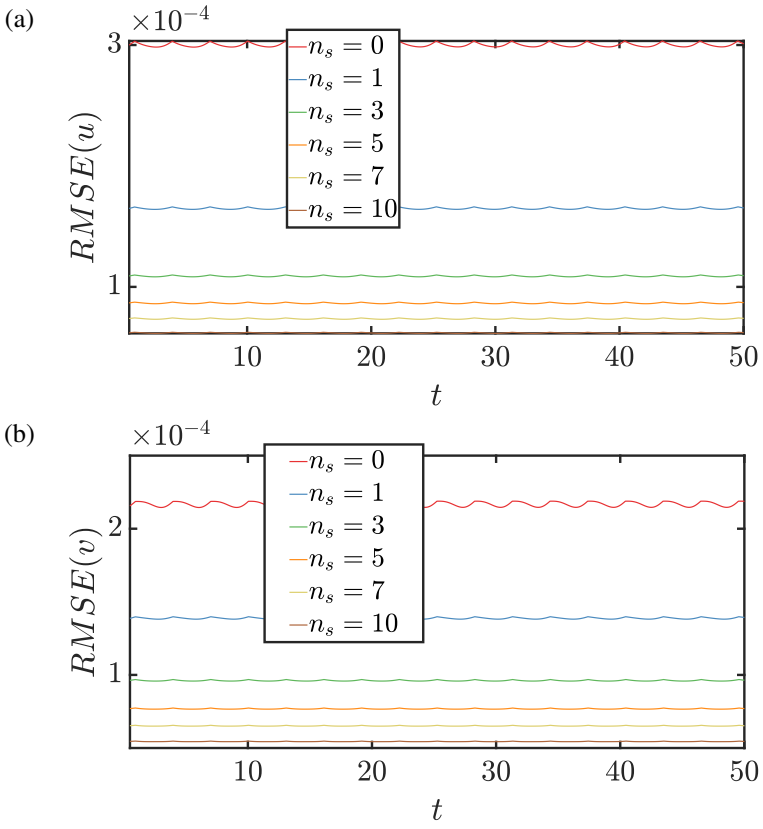

Figure 2.6: Time histories of the RMSE of the velocity components on the body as a function of the total number of force iterations n_s

RHS of the Navier-Stokes equations (2.1a) is computed at each Eulerian grid point using again the shape functions of the interpolation procedure

$$f_i^k = \sum_{l=1}^{n_l} c_l \Psi_k^l F_i^l, \tag{2.24}$$

where f_i^k is the $i-$th component of the forcing for the $k-$th Eulerian grid point, n_l is the number of Lagrangian markers whose support domain contains the selected Eulerian point and c_l is a scaling coefficient needed to ensure the conservation of momentum through the forcing operation (Nitti et al. 2020).

The above-described procedure correctly enforces the boundary conditions, provided that the Lagrangian markers are distributed uniformly on the body and provide sufficient resolution. Hence, the maximum spacing between two contiguous markers has to be comparable to the local size of the Eulerian grid (de Tullio and Pascazio, 2016). In the present solver, Lagrangian markers are separated by a distance that is about $0.7h$, where h indicates the local cell size of the Eulerian grid.

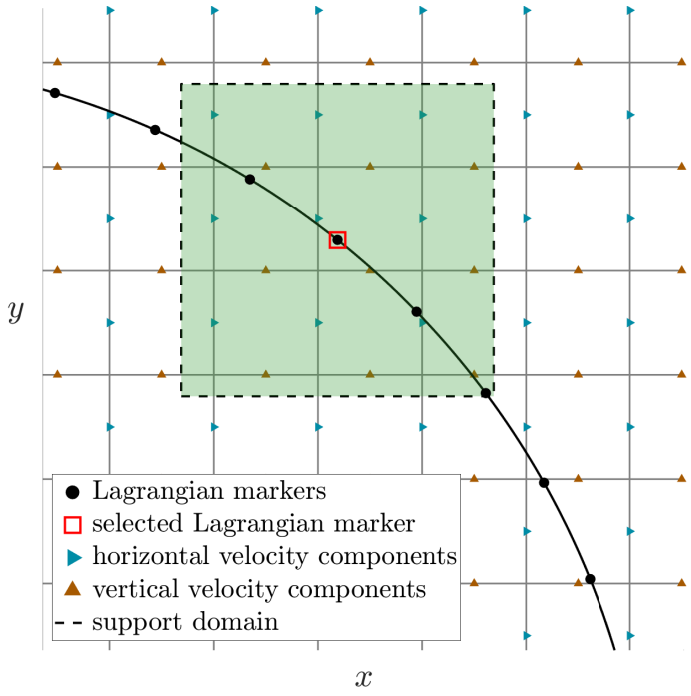

Figure 2.7: Scheme of the IB forcing. The green area contains the Eulerian nodes belonging to the support domain of the selected marker.

References

Anderson, E. et al. (1990). "LAPACK: A portable linear algebra library for high-performance computers". English. In: *SC*. Proceedings of Supercomputing '90 ; Conference date: 01-07-1990. United States: IEEE, pp. 2–11. ISBN: 0818620560.

Baek, Hyoungsu and George Em Karniadakis (2012). "A convergence study of a new partitioned fluid–structure interaction algorithm based on fictitious mass and damping". In: *Journal of Computational Physics* 231.2, pp. 629–652. ISSN: 0021-9991. DOI: https://doi.org/10.1016/j.jcp.2011.09.025.

Breugem, Wim-Paul (May 2012). "A second-order accurate immersed boundary method for fully resolved simulations of particle-laden flows". In: *Journal of Computational Physics* 231, pp. 4469–4498. DOI: 10.1016/j.jcp.2012.02.026.

Briley, W.R and H McDonald (1980). "On the structure and use of linearized block implicit schemes". In: *Journal of Computational Physics* 34.1, pp. 54–73. ISSN: 0021-9991. DOI: https://doi.org/10.1016/0021-9991(80)90112-6.

Causin, P., J.F. Gerbeau, and F. Nobile (2005). "Added-mass effect in the design of partitioned algorithms for fluid–structure problems". In: *Computer Methods in Applied Mechanics and Engineering* 194.42, pp. 4506–4527. ISSN: 0045-7825. DOI: https://doi.org/10.1016/j.cma.2004.12.005.

Chorin, Alexandre (Oct. 1968). "Numerical Solution of the Navier–Stokes Equations". In: *Mathematics of Computation* 22. DOI: 10.2307/2004575.

de Tullio, M.D., P. De Palma, et al. (2007). "An immersed boundary method for compressible flows using local grid refinement". In: *Journal of Computational Physics* 225.2, pp. 2098–2117. ISSN: 0021-9991. DOI: https://doi.org/10.1016/j.jcp.2007.03.008.

de Tullio, M.D. and G. Pascazio (2016). "A moving-least-squares immersed boundary method for simulating the fluid–structure interaction of elastic bodies with arbitrary thickness". In: *Journal of Computational Physics* 325, pp. 201–225. ISSN: 0021-9991. DOI: https://doi.org/10.1016/j.jcp.2016.08.020.

Fadlun, E.A. et al. (2000). "Combined Immersed-Boundary Finite-Difference Methods for Three-Dimensional Complex Flow Simulations". In: *Journal of Computational Physics* 161.1, pp. 35–60. ISSN: 0021-9991. DOI: https://doi.org/10.1006/jcph.2000.6484.

Förster, Christiane, Wolfgang A. Wall, and Ekkehard Ramm (2007). "Artificial added mass instabilities in sequential staggered coupling of nonlinear structures and incompressible viscous flows". In: *Computer Methods in Applied Mechanics and Engineering* 196.7, pp. 1278–1293. ISSN: 0045-7825. DOI: https://doi.org/10.1016/j.cma.2006.09.002.

Goldstein, D., R. Handler, and L. Sirovich (1993). "Modeling a No-Slip Flow Boundary with an External Force Field". In: *Journal of Computational Physics* 105.2, pp. 354–366. ISSN: 0021-9991. DOI: https://doi.org/10.1006/jcph.1993.1081.

Haidvogel, Dale B and Thomas Zang (1979). "The accurate solution of poisson's equation by expansion in chebyshev polynomials". In: *Journal of Computational Physics* 30.2, pp. 167–180. ISSN: 0021-9991. DOI: https://doi.org/10.1016/0021-9991(79)90097-4.

Hou, Gene, Jin Wang, and Anita Layton (2012). "Numerical Methods for Fluid-Structure Interaction — A Review". In: *Communications in Computational Physics* 12.2, pp. 337–377. DOI: 10.4208/cicp.291210.290411s.

Kempe, Tobias and Jochen Fröhlich (2012). "An improved immersed boundary method with direct forcing for the simulation of particle laden flows". In: *Journal of Computational Physics* 231.9, pp. 3663–3684. ISSN: 0021-9991. DOI: https://doi.org/10.1016/j.jcp.2012.01.021.

Kim, Jungwoo, Dongjoo Kim, and Haecheon Choi (2001). "An Immersed-Boundary Finite-Volume Method for Simulations of Flow in Complex Geometries". In: *Journal of Computational Physics* 171.1, pp. 132–150. ISSN: 0021-9991. DOI: https://doi.org/10.1006/jcph.2001.6778.

Kim, Woojin and Haecheon Choi (2019). "Immersed boundary methods for fluid-structure interaction: A review". In: *International Journal of Heat and Fluid Flow* 75, pp. 301–309. ISSN: 0142-727X. DOI: https://doi.org/10.1016/j.ijheatfluidflow.2019.01.010.

Lācis, Uğis, Kunihiko Taira, and Shervin Bagheri (Jan. 2016). "A stable fluid–structure-interaction solver for low-density rigid bodies using the immersed boundary projection method". In: *Journal of Computational Physics* 305, pp. 300–318. DOI: 10.1016/j.jcp.2015.10.041.

Lai, Ming-chih and Charles S. Peskin (2000). "An immersed boundary method with formal second-order accuracy and reduced numerical viscosity". In: *J. Comput. Phys*, pp. 705–719.

Mittal, Rajat and Gianluca Iaccarino (2005). "IMMERSED BOUNDARY METHODS". In: *Annual Review of Fluid Mechanics* 37.1, pp. 239–261. DOI: 10.1146/annurev.fluid.37.061903.175743. eprint: https://doi.org/10.1146/annurev.fluid.37.061903.175743.

Mohan Rai, Man and Parviz Moin (1991). "Direct simulations of turbulent flow using finite-difference schemes". In: *Journal of Computational Physics* 96.1, pp. 15–53. ISSN: 0021-9991. DOI: https://doi.org/10.1016/0021-9991(91)90264-L.

Nitti, Alessandro et al. (June 2020). "An immersed-boundary/isogeometric method for fluid–structure interaction involving thin shells". In: *Computer Methods in Applied Mechanics and Engineering* 364, p. 112977. DOI: 10.1016/j.cma.2020.112977.

O'Rourke, Joseph (1998). *Computational Geometry in C*. 2nd ed. Cambridge University Press. DOI: 10.1017/CBO9780511804120.

Orlandi, Paolo (2001). *Fluid Flow Phenomena - A Numerical Toolkit*. 1st ed. Fluid Mechanics and Its Applications. Springer Dordrecht. DOI: https://doi.org/10.1007/978-94-011-4281-6.

Peskin, Charles S. (1972). "Flow patterns around heart valves: A numerical method". In: *Journal of Computational Physics* 10.2, pp. 252–271. ISSN: 0021-9991. DOI: https://doi.org/10.1016/0021-9991(72)90065-4.

Souli, M., A. Ouahsine, and L. Lewin (2000). "ALE formulation for fluid–structure interaction problems". In: *Computer Methods in Applied Mechanics and Engineering* 190.5, pp. 659–675. ISSN: 0045-7825. DOI: https://doi.org/10.1016/S0045-7825(99)00432-6.

Tseng, Yu-Heng and JH Ferziger (Dec. 2003). "A ghost-cell immersed boundary method for flow in complex geometry". In: *Journal of Computational Physics* 192, pp. 593–623. DOI: 10.1016/j/jcp.2003.07.024.

Udaykumar, H.S. et al. (2001). “A Sharp Interface Cartesian Grid Method for Simulating Flows with Complex Moving Boundaries”. In: *Journal of Computational Physics* 174.1, pp. 345–380. ISSN: 0021-9991. DOI: https://doi.org/10.1006/jcph.2001.6916.

Uhlmann, Markus (July 2003). *First Experiments with the Simulation of Particulate Flows*.

– (2005). “An immersed boundary method with direct forcing for the simulation of particulate flows”. In: *Journal of Computational Physics* 209.2, pp. 448–476. ISSN: 0021-9991. DOI: https://doi.org/10.1016/j.jcp.2005.03.017.

Vanella, Marcos and Elias Balaras (2009). “A moving-least-squares reconstruction for embedded-boundary formulations”. In: *Journal of computational physics (Print)* 228.18, pp. 6617–6628.

Viecelli, J.A. (1971). “A computing method for incompressible flows bounded by moving walls”. In: *Journal of Computational Physics* 8.1, pp. 119–143. ISSN: 0021-9991. DOI: https://doi.org/10.1016/0021-9991(71)90039-8.

Welch, J E et al. (Nov. 1965). “The MAC method-A computing technique for solving viscous, incompressible, transient fluid-flow problems involving free surfaces”. In: DOI: 10.2172/4563173.

Chapter 3

GLOBAL STABILITY ANALYSIS OF FLUID-STRUCTURE INTERACTION PROBLEMS

A method is more important than a discovery since the right method will lead to new and even more important discoveries.

Lev D. Landau

This chapter starts with an introduction to the modal linear stability theory. Then, a general time-stepping procedure is described for the stability analysis of systems involving a reduced structure immersed in an incompressible viscous flow. The algorithm is implemented practically using the finite-differences code described in the previous chapter. Eventually, the method is validated on a classic fluid-structure benchmark problem. The results show a good agreement with instability studies reported in the literature and obtained with body-conformal approaches. Additionally, details are provided on the appropriate selection of the linearization parameters.

3.1 Introduction

Over the nineteenth century, the majority of research efforts in the context of hydrodynamic linear stability theory have been focused on understanding the early stages of laminar-turbulence transition in parallel flows (Peter J. Schmid and D. Henningson, 2001). The evolution of disturbances of such monodimensional velocity profiles is traditionally investigated by means of a modal decomposition, resulting in a relatively small eigenproblem that does not require high computing power to be solved. Over the last decades, as a result of the advancement in computing resources and algorithmic developments, the scope and applications of linear instability analyses have expanded significantly (Vassilios Theofilis, 2003), including the study of two-dimensional and three-dimensional nonparallel flows. In this case, the literature is generally concurrent to refer to the linear stability analysis as *global*.

From a computational point of view, even with modern hardware, the size of the resulting non-symmetric generalized EVPs might represent a challenge for large-scale problems. To alleviate the restrictions on the size of the systems, many iterative

approaches have been developed that rely on matrix-free techniques (Mettot, Renac, and Sipp, 2014) to extract information from the flow. The focus here will be on iterative time-stepping methodologies, which couple common iterative algorithms for the solution of EVPs with validated codes for direct numerical simulations (DNS). In recent years, thanks to the advancement in computational hardware, accurate and fast DNS solvers have become affordable for the average user. High-fidelity simulations are able to capture all the relevant flow physics, provided that all the relevant scales are resolved, hence they have become the method of choice for the analysis of complex flow problems. Furthermore, quoting Orlandi (2001), "it is indeed true, as someone claims, that codes to solve the 3D Navier-Stokes equations are available at the supermarkets".

In this chapter, a time-stepping methodology is presented for the global linear stability analysis of FSI problems. The method makes use of high-fidelity nonlinear simulations obtained with a direct-forcing IB method, based on an MLS approach. One of the main advantages of the IB formulation resides in the fact that it can handle multi-body configurations with no additional complexity. In addition, the fluid equations are resolved on a staggered Cartesian grid, which makes the method prone to a simple parallel implementation for three-dimensional computations.

The choice of the specific IB forcing technique is crucial for the success of the computation. It has been noted that the use of a sharp forcing field usually leads to the appearance of unphysical fluctuations of the hydro-dynamical force acting on the solid body (Uhlmann, 2003). Seo and R. Mittal (2011) attributed the emergence of pressure oscillations to an unintended *transpiration* effect at the immersed boundary, due to the fact that the role of the Eulerian nodes close to the interface can change from a time-step to the next as the body moves. These spurious oscillations can be suppressed by spreading the forcing term over a wider stencil through the use of a smoother Lagrangian-Eulerian transfer function (X. Yang et al. 2009). In view of these considerations, the MLS forcing procedure exposed in section 2.4 is selected, which provides a good trade-off between accuracy and robustness.

The proposed strategy involves the adoption of the matrix exponential, first introduced by Eriksson and Rizzi (1985) in the context of global stability analysis. In their paper, the authors proposed to approximate the action of the Jacobian matrix via finite differences to investigate the instability of the transonic flow over an airfoil, a phenomenon modeled by the two-dimensional Euler equations. They also highlighted the need for a matrix transformation to retrieve the least stable portion of the spectrum of the discrete operator. The same approach was later extended to the full

Navier-Stokes equations by Chiba (1998), who performed a linear stability analysis of the two-dimensional square lid-driven cavity flow, and by Tezuka and Suzuki (2006), who carried out a TriGlobal stability analysis (V. Theofilis and Colonius, 2011) of the flow around various spheroids.
Gómez, Gomez, and V. Theofilis (2011) incorporated the approach of Tezuka and Suzuki (2006) into publicly-available computational fluid dynamics (CFD) solvers, highlighting the flexibility of the method that looks at the CFD solver as a black-box source. In a successive paper, Gómez, Pérez, et al. (2015) extended that work by inserting a shift-invert strategy to grant access to specific portions of the spectrum. This contribution builds on the above-mentioned series of papers and provides an extension of Chiba's approach to FSI problems.

3.2 Iterative eigenvalue computation

Iterative eigenspectrum retrieval is, without a doubt, the method of choice for global stability analyses of complex flows, owing to the reduced computational requirements with respect to direct methods. In this context, projection methods are by far the most popular technique employed to reduce the size of an eigenvalue problem. Among these, Krylov subspace methods (D. Sorensen, 2002) have been extensively used by the fluid mechanics community. The underlying idea is to search for an approximate solution to an eigenproblem with size N by projecting it on an m–dimensional Krylov subspace obtained by repeated applications of the system stability matrix $\boldsymbol{Q}$ on a starting vector $\boldsymbol{v}_1$

$$\mathcal{K}_m\left(\boldsymbol{Q}, \boldsymbol{v}_1\right) = span\{\boldsymbol{v}_1, \boldsymbol{Q}\boldsymbol{v}_1, \boldsymbol{Q}^2\boldsymbol{v}_1, ..., \boldsymbol{Q}^{m-1}\boldsymbol{v}_1\}. \tag{3.1}$$

The assembly of the sequence given by (3.1) requires only a series of matrix-vector multiplications, hence the algorithm performing them is used as a black box from the iterative procedure. This aspect constitutes a big advantage of projection methods and lays the foundation of time-stepping methodologies. The simplest algorithm of this kind is the power iteration method, which uses only the last element of the sequence to approximate the largest eigenvalue (in modulus) of the matrix $\boldsymbol{Q}$.
The first application of Krylov methods in the field of hydrodynamic stability dates back to Edwards et al. (1994), who carried out an LSA of the incompressible NS equations via the Implicitly Restarted Arnoldi Method (IRAM) . The classic Arnoldi algorithm is undoubtedly the most popular method belonging to the Krylov-subspace's family. It consists in the assembly of an orthonormal basis

$\boldsymbol{V}_m = [\boldsymbol{v}_1, \boldsymbol{v}_2, ..., \boldsymbol{v}_m]$ of the Kylov subspace $\mathcal{K}_m$, which is then used to create a reduced Hessenberg matrix :

$$\boldsymbol{Q}\boldsymbol{V}_m = \boldsymbol{V}\boldsymbol{H}_m + \boldsymbol{r}_m \boldsymbol{e}_m^{\mathsf{T}}, \tag{3.2}$$

where $\boldsymbol{H}_m$ is the $m \times m$ Hessenberg matrix, $\boldsymbol{r}_m$ is the residual vector and $\boldsymbol{e}_m^{\mathsf{T}}$ is the m–th unit vector in $\mathbb{R}^m$. The outline of the basic Arnoldi factorization is given below. The entries of the Hessenberg matrix are indicated with $h_{i,j}$. Thanks to

Algorithm 1 Arnoldi method

Select: m, $\boldsymbol{v}_1 \in \mathbb{R}^n$
$\boldsymbol{v}_1 \rightarrow \boldsymbol{v}_1 / \|\boldsymbol{v}_1\|_2$
for $k = 1$ to m **do**
  $\boldsymbol{z} = \boldsymbol{Q}\boldsymbol{v}_k$
  for $i = 1, ..., k$ **do**
    $h_{i,k} = \boldsymbol{v}_i^{\mathsf{T}} \boldsymbol{z}$
    $\boldsymbol{z} = \boldsymbol{z} - h_{i,k}\boldsymbol{v}_i$
  end for
  $h_{k+1,k} = \|\boldsymbol{z}\|_2$
  $\boldsymbol{v}_{k+1} = \boldsymbol{z} / h_{k+1,k}$
end for

its small dimension, the eigenvalues of matrix $\boldsymbol{H}_m$, the so-called *Ritz values*, can be computed by direct means. Their value constitutes an approximation of the eigenvalues of matrix $\boldsymbol{Q}$.
In the following section, after the introduction of the linear stability problem for a generic system, a time-stepping methodology is proposed for FSI applications.

3.3 Governing equations

The evolution in time of a generic continuous-time physical system (also called a *flow* (Bhatia and Szegö, 1970)) is frequently governed by differential equations that arise from conservation principles. For a fluid system, for instance, these basic principles include the conservation of mass, momentum, and energy. In the continuum model, these concepts often assume the form of an ordinary differential equation,

$$\frac{d\boldsymbol{q}}{dt} = \boldsymbol{R}(t, \{\beta_i\}, \boldsymbol{q}) \tag{3.3}$$

where $\boldsymbol{q}$ is a *state vector* , collecting all the variables that describe the system, $\{\beta_i\}$ is a set of parameters that influence the dynamics and $\boldsymbol{R}$ is a smooth function called the *evolution operator* of the system. For instance, for a two-dimensional flow

interacting with a rigid body, $\boldsymbol{q} = [\boldsymbol{u}, p, \boldsymbol{x}_B]^\intercal$.
According to the linear theory, we are interested in asymptotic solutions of the IVP (3.3), *i.e.* steady solutions or periodic ones. In this thesis, only steady solutions $\boldsymbol{q}_b$ to (3.3) will be considered, for which

$$\boldsymbol{R}\left(t, \{\beta_i\}, \boldsymbol{q}_b\right) = 0. \tag{3.4}$$

The stability of periodic orbits, for which $\boldsymbol{q}_b(t+T) = \boldsymbol{q}_b(t)$, can be analyzed in the same fashion under the Floquet theory . According to the linear theory, the state vector can be decomposed as the sum of the basic state $\boldsymbol{q}_b$ and a small-amplitude perturbation $\boldsymbol{q}'$

$$\boldsymbol{q}\left(t\right) = \boldsymbol{q}_b + \epsilon \boldsymbol{q}'\left(t\right), \tag{3.5}$$

where ϵ is a small scalar. Injecting this expansion into (3.3), the time derivative of $\boldsymbol{q}$ can be approximated by a Taylor series

$$\frac{d\boldsymbol{q}}{dt} = \epsilon \frac{d\boldsymbol{q}'}{dt} \approx \epsilon \left.\frac{\partial \boldsymbol{R}}{\partial \boldsymbol{q}}\right|_{\boldsymbol{q}_b} \boldsymbol{q}' + O(\epsilon^2). \tag{3.6}$$

Neglecting higher order terms in ϵ, the stability of the system is predicted by the solutions of an IVP for $\boldsymbol{q}'$,

$$\frac{d\boldsymbol{q}'}{dt} = \left.\frac{\partial \boldsymbol{R}}{\partial \boldsymbol{q}}\right|_{\boldsymbol{q}_b} \boldsymbol{q}' = \boldsymbol{J}\left(\boldsymbol{q}_b\right) \boldsymbol{q}', \tag{3.7}$$

where $\boldsymbol{J}(\boldsymbol{q}_b)$ is the linear Jacobian operator evaluated with respect to the steady-state $\boldsymbol{q}_b$. Then, following the traditional modal approach, the perturbation is expanded into a series of normal modes

$$\boldsymbol{q}'(t) = \sum_i \left(\hat{\boldsymbol{q}}_i e^{\omega_i t} + c.c.\right), \tag{3.8}$$

where ω_i is a complex eigenvalue [1], $\hat{\boldsymbol{q}}_i$ is the corresponding eigenfunction and $c.c.$ indicates the complex conjugate. Accordingly, the stability characteristics of the system can be deduced from solutions of an EVP for the Jacobian operator

$$\left(\boldsymbol{J}\left(\boldsymbol{q}_b\right) - \boldsymbol{I}\omega\right) \hat{\boldsymbol{q}} = 0, \tag{3.9}$$

where $\boldsymbol{I}$ is the identity tensor. In the case of an autonomous system, *i.e.* a system for which $\boldsymbol{R}$ does not depend explicitly on time, the exact solution of the linear initial value problem expressed by eq. (3.9) is given by

$$\boldsymbol{q'}(t_0 + T) = e^{\boldsymbol{J}(\boldsymbol{q}_b)T} \boldsymbol{q'}(t_0) = \boldsymbol{\Phi}(T) \boldsymbol{q'}(t_0), \tag{3.10}$$

[1] $\boldsymbol{q}'$ is actually equal to the real part of the expansion.

where the operator $\mathbf{\Phi}$ is known as the *exponential propagator* of the system. The propagator can be interpreted as the operator that advances in time the small amplitude perturbations on $\boldsymbol{q}_b$. Injecting into (3.10) the modal decomposition, one gets the following eigenvalue problem

$$\mu\hat{\boldsymbol{q}} = \mathbf{\Phi}(T)\hat{\boldsymbol{q}}. \tag{3.11}$$

The eigenvalues of the two problems are related through the exponential transformation $\mu = e^{\omega T}$, while the eigenvectors remain unchanged. The asymptotic linear stability properties of the system are dictated by the module of the eigenvalues μ. If all eigenvalues have $|\mu| < 1$, the system is linearly stable, while it is unstable if at least one eigenvalue has $|\mu| > 1$. For $|\mu| = 1$, the system is neutrally stable. For periodic base states, the propagator is denoted as *monodromy operator* and its eigenvalues are known as *Floquet multipliers*. The exponential transformation alters the spectrum in such a way that the *dominant* eigenvalues, *i.e.* the eigenvalues of largest modulus, correspond to the leading ones in the original eigenvalue problem, where with the term *leading*, we refer to the eigenvalues with the largest real parts. This is a desirable feature, since iterative solvers, such as the Arnoldi algorithm, identify the dominant eigenvalues of the system, if not used in conjunction with some spectral transformation.

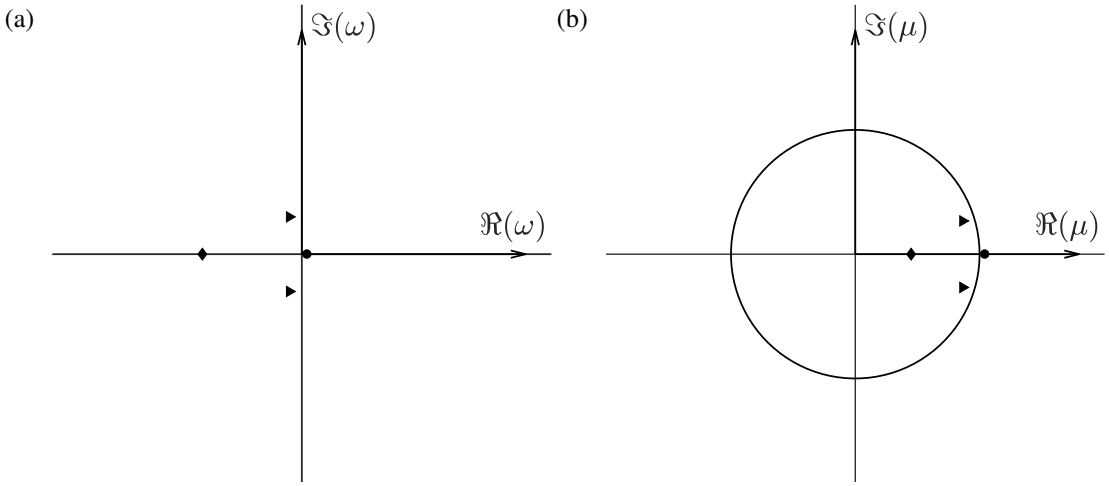

Figure 3.1: Exponential tranformation of the spectrum. The eigenvalues ω of operator $\boldsymbol{J}$ (a) are shifted to the right after the exponential transformation $\mu = e^{\omega T}$ (b). On the right, the unit circle is reported to show the clustering of the least stable eigenvalues near the circumference.

3.4 Numerical strategy

The problem of linear stability is now reduced to finding the eigenvalues of the propagator $\boldsymbol{\Phi}$. In a discrete framework, this reduces to finding the eigenvalues of an $N \times N$ matrix, where the size of the system N is given by the number of cells or nodes of the discretized domain times the number of flow variables, plus the degrees of freedom of the body. For real-world systems, the explicit calculation (and storage) of the matrix exponential often carries a prohibitive computational load and one must resort to iterative algorithms, such as those belonging to the class of Krylov-subspace projection methods. In these algorithms, an m–dimensional Hessenberg matrix $\boldsymbol{H}$ (with $m \ll N$) approximates the matrix exponential in a low-dimensional Krylov subspace, which is constructed via the repeated action of operator $\boldsymbol{\Phi}$ on a given starting vector. The eigenvalues of the Hessenberg matrix, the so-called *Ritz values*, constitute an approximation of the eigenvalues of the exponential matrix.

Given the matrix-free framework of this method, one aims at approximating the action of $\boldsymbol{\Phi}$ on a perturbation vector. This is done by introducing the propagator $\boldsymbol{F}(\boldsymbol{q})$ of the complete solution,

$$\boldsymbol{q}(t_0 + T) = \boldsymbol{F}(\boldsymbol{q}_0, \{\beta_i\}, T), \tag{3.12}$$

where $\boldsymbol{q}_0$ is the value assumed by the state vector $\boldsymbol{q}$ at a given time $t = t_0$ and $\boldsymbol{q}(t_0 + T)$ represents its evolution after a period T. The solution at time $t = t_0$ can be expressed as the superposition of the previously defined steady-state $\boldsymbol{q}_b$ and a small amplitude deviation from it $\epsilon \boldsymbol{q}'(t_0)$. A Taylor expansion of operator $\boldsymbol{F}$ around the base state $\boldsymbol{q}_b$ yields

$$\boldsymbol{F}(\boldsymbol{q}_b + \epsilon \boldsymbol{q}'(t_0), T) = \boldsymbol{F}(\boldsymbol{q}_b, T) + \left.\frac{\partial \boldsymbol{F}(\boldsymbol{q}, T)}{\partial \boldsymbol{q}}\right|_{\boldsymbol{q}_b} \epsilon \boldsymbol{q}'(t_0) + O(\epsilon^2), \tag{3.13}$$

where the dependence of $\boldsymbol{F}$ upon the set of parameters $\{\beta_i\}$ has been neglected for conciseness. It can be shown that the second term on the RHS is, up to the scalar ϵ, an approximation of $(\boldsymbol{q}'(t_0 + T) - \boldsymbol{q}'(t_0))$ for small values of T. The details of this derivation are provided in section A.1 of the appendix.

Substituting this expression into the RHS of (3.13) and neglecting higher order terms in ϵ, one gets an expression for evaluating the advancement in time of the perturbation based only on the propagator of the complete solution

$$\boldsymbol{q}'(t_0 + T) \approx \frac{\boldsymbol{F}(\boldsymbol{q}_b + \epsilon \boldsymbol{q}'(t_0), T) - \boldsymbol{F}(\boldsymbol{q}_b, T)}{\epsilon}. \tag{3.14}$$

Taking the limit of (3.14) as $\epsilon \to 0$, the RHS gives a Gateaux derivative of $\boldsymbol{F}$ at $\boldsymbol{q}_b$,

$$\lim_{\epsilon \to 0} \frac{\boldsymbol{F}(\boldsymbol{q}_b + \epsilon \boldsymbol{q}'(t_0), T) - \boldsymbol{F}(\boldsymbol{q}_b, T)}{\epsilon}. \tag{3.15}$$

In a discrete context, the action of the time-marching matrix of the perturbation can be recovered through a finite difference that only involves calls to the time-stepping scheme described in section 2.4. Here the same nomenclature is used to refer to both the time-discrete and time-continuous operator

$$\boldsymbol{q}^{n+1} = \boldsymbol{F}(\{\beta_i\}, \boldsymbol{q}^n) \tag{3.16}$$

In the equation above, $\boldsymbol{F}$ is the time-stepper used to advance the solution from time level n to $n+1$. Selecting a small but non-zero value of ϵ, the derivative given by eq. (3.15) can be approximated by

$$\frac{\boldsymbol{F}(\boldsymbol{q}_b + \epsilon \boldsymbol{q}_p(t_0), n_{st}\Delta t) - \boldsymbol{F}(\boldsymbol{q}_b, n_{st}\Delta t)}{\epsilon}, \tag{3.17}$$

where $\boldsymbol{q}_p$ represents the perturbation vector in the discrete system. For ease of notation, the same notation $\boldsymbol{q}_b$ is employed to refer to both the continuous and spatially discretized base state. The parameter n_{st} is the number of time-steps by which the solution is advanced in time and Δt is simply the time-step of the scheme, chosen according to the desired CFL condition.

A better approximation of (3.15) can be built via higher-order finite differences. For the results presented in this thesis, a second-order central finite difference is used to approximate the evolution of a given perturbation $\boldsymbol{q}_p(t_0)$

$$\boldsymbol{q}_p(t_0 + n_{st}\Delta t) = \frac{\boldsymbol{q}_+ - \boldsymbol{q}_-}{2\epsilon}, \tag{3.18}$$

where $\boldsymbol{q}_+$ and $\boldsymbol{q}_-$ are the results of two separate calls to the FSI solver, advancing in time the base state after the addition and subtraction, respectively, of the same small perturbation:

$$\boldsymbol{q}_+ = \boldsymbol{F}(\boldsymbol{q}_b + \epsilon \boldsymbol{q}_p(t_0), n_{st}\Delta t), \tag{3.19}$$

$$\boldsymbol{q}_- = \boldsymbol{F}(\boldsymbol{q}_b - \epsilon \boldsymbol{q}_p(t_0), n_{st}\Delta t). \tag{3.20}$$

Although such an approach presents the disadvantage of requiring two calls to the time-stepper, it reduces the number of required iterations by providing a more accurate estimate for the matrix-vector product (Knoll and Keyes, 2004).

A set of the least stable eigenvalues can now be computed via a Krylov projection method. In this work, approximations to the leading eigenvalues of the system are computed using the IRAM algorithm (Danny C. Sorensen, 1992) as implemented in the open source package ARPACK (Lehoucq, D. C. Sorensen, and C. Yang, 1998). The base states here considered are equilibrium solutions of the fully coupled

nonlinear system, therefore their evaluation requires the solution of a nonlinear algebraic system.

For large-scale problems, a pure Newton-Raphson method is prohibitive because of the size of the systems, hence the most common approach to overcome this difficulty is the use of a Newton-Krylov technique. With the proposed methodology, the base state for each test case was computed using *BoostConv* (Citro et al. 2017), an iterative residual recombination procedure belonging to the class of Krylov methods.

The choice of such an algorithm fits perfectly into the proposed matrix-free approach since *BoostConv* can be easily applied as a black-box procedure that requires only several calls to a pre-existing time-marching algorithm, without any modification. The outline of the algorithm is shown below

For all cases shown in this thesis, a non-zero pseudo-random perturbation has been

---

Algorithm 2 Proposed methodology

Compute base state with *BoostConv* (Citro et al. 2017)
Select starting vector $\boldsymbol{q}_p^0$
while Covergence is not reached **do**
    $\boldsymbol{q}_p^k \rightarrow$ Call ARPACK (Lehoucq, D. C. Sorensen, and C. Yang, 1998)
    Call time-stepper $\rightarrow \boldsymbol{q}_p^{k+1} = \frac{\boldsymbol{q}_+ - \boldsymbol{q}_-}{2\epsilon}$
    Reverse communication with ARPACK
    Check convergence of the desired Ritz pairs
end while
Perform the logarithmic transformation to recover the original eigenvalues:
$\omega = (\log|\mu| + i\arg(\mu))\,(n_{st}\Delta t)^{-1}$.

---

employed as a starting vector for the Arnoldi iterations, with the only requirement of respecting the divergence constraint on the velocity. It is worth pointing out that the present approach circumvents the need to select appropriate boundary conditions for the perturbation field, while the boundary conditions of the nonlinear evolution problem are included in the discrete operator $\boldsymbol{F}$.

Some remarks on the effect of the IB interface on the linear results With the IB approach, the solid-fluid interface is enforced by a time-varying distribution of forcing terms that mimics the effect of the body on the flow. Since, in general, the interface does not coincide with the grid lines, the need for an interpolation procedure arises. The way this transfer of information is done defines the specific variant of the IB method.

In the presence of a moving interface, the choice of the interpolation scheme is even

more important. It has been noted, for instance, that non-physical force oscillations arise, in this case, with some variants of the IB method (X. Yang et al. 2009), like the discrete Delta function formulation. Complications emerge also with the Cartesian grid (or cut-cell) approach, in which the fluid-solid interface is sharply tracked, in view of the fact that the role of the grid points near the interface can change from time-step to time-step (J. Yang and Balaras, 2006) (*i.e.* a grid point that belongs to the portion of the domain occupied by the solid at a given time-step can drop out of the body contour at the next time-step and viceversa). While the role of the node changes, it still carries the physical information about its previous phase, consequently, the local pressure field is strongly perturbed.

The choice of the above-described MLS technique, among the diverse options belonging to the class of non-conforming methods, is motivated by the need for a smooth transfer between Lagrangian and Eulerian nodes (Vanella and Balaras, 2009; Uhlmann, 2003). Indeed, the emergence of non-physical pressure oscillations in the nonlinear solution would have a detrimental impact on the accuracy of (3.18), involved in the computation of the linear modes with respect to the steady-state. The present method shows reduced spurious oscillations in the vicinity of the interface due to the fact that the IB forcing field is slightly smeared within the compact support of the MLS interpolation.

One issue of interest is to what extent the smeared representation of the interface affects the accuracy of the computation for higher Reynolds number flows. The wall-resolved computation of the viscous shear layer in presence of moving immersed boundaries is still an open research area. One way to improve the local accuracy with reasonable computational expense within an IB framework is to employ a locally refined semi-structured grid (Durbin and Iaccarino, 2002; de Tullio et al. 2007) in order to increase the grid resolution near the body. It is worth recalling that the present method relies on the linearization of the system around steady solutions of the Navier-Stokes equations, which usually exist for sufficiently low Reynolds numbers.

Another point to be considered is the effect of the IB treatment on the evaluation of the finite difference in (3.18) itself. When the position of a given Lagrangian marker falls into a certain grid cell in the solution $\boldsymbol{q}_+$ and into an adjacent cell in $\boldsymbol{q}_-$, the subtraction $(\boldsymbol{q}_+ - \boldsymbol{q}_-)$ involves grid points that are included in the support domain of the marker in one case and left out in the other. To avoid this problem, the support domain of each marker is kept fixed during the evaluation of $\boldsymbol{q}_+$ and $\boldsymbol{q}_-$, such that the forced fluid cells are the same in the two solutions. The corresponding marker

is prevented from falling outside of the fixed support owing to the short integration time T and the small scaling factor ϵ employed in the linearization procedure. In this way, the procedure provides an accurate and robust computation of leading modes with a finite difference approach.

Selection of the linearization parameters

One critical aspect of the presented procedure is the selection of the linearization parameters, *i.e.* the integration period $T = n_{st}\Delta t$ and the perturbation scaling factor ϵ.

The choice of the integration time is somewhat problem dependent. As reported by Goldhirsch (Goldhirsch, Orszag, and Maulik, 1987), for a given number of requested eigenvalues k, the order of the error related to the model reduction is given by $\left|e^{(\omega_k-\omega_m)T}\right|$. This means that the accuracy can be improved either by increasing the number of integration time steps n_{st}, or by augmenting the dimension of the basis m. Eriksson and Rizzi (1985) refer to n_{st} as a *selectivity* parameter, in the sense that, as it increases, the separation among the least damped eigenvalues is magnified. Both options can provide sufficient separation between the desired eigenvalues and the remaining part of the spectrum.

In spite of that, it is worth noting that this methodology is based on an approximation of the evolved perturbation, given by (3.14), which is valid for short integration periods. For this reason, it is legitimate to keep T small while increasing the value of m for particularly clustered eigenvalues. Table 3.1 reports the results of the LSA of the uniform flow past a fixed circular cylinder at $Re = 60$, as the number of time steps n_{st} employed by the linearization procedure is varied. All the computations are carried out using the same dimension $m = 30$ for the Krylov subspace and requesting the same number of eigenvalues with tolerance 10^{-6}. As can be seen in Table 3.1, the number of Arnoldi iterations required for convergence decreases almost linearly and, consequently, so does the total number of matrix-vector multiplications required (see Figure 3.2a). However, given that the simulations are carried out with a fixed time step equal for all cases, the actual cost of the operation is given by the total number of single time step advancements, reported in Figure 3.2b. For the case under investigation, this shows that it is not convenient to select a large value for n_{st}. It must be noted, however, that in this case there is only one unstable eigenvalue. In presence of multiple clustered unstable eigenvalues, a bigger value of n_{st} could be a more suitable choice. One issue to be considered when dealing with iterative methods is the need for convergence acceleration that arises for high-resolution simulations.

n_{st}	N_A	ω_r	ω_i
1	317	0.0483	0.7444
2	266	0.0477	0.7441
4	138	0.0479	0.7457
10	81	0.0484	0.7435
20	51	0.0485	0.7448
30	36	0.0481	0.7436
50	27	0.0485	0.7446
100	15	0.0482	0.7440

Table 3.1: Results of the eigenvalue calculation for the uniform flow past a fixed circular cylinder at $Re = 60$. The table shows the growth rate ω_r and circular frequency ω_i of the leading eigenvalue computed for a different number of time steps n_{st} in the linearization procedure. The dimension of the Krylov subspace is $m = 30$ for all the calculations, as the size of the single time step $\Delta t = 3 \times 10^{-3}$. The table also reports the total number of Arnoldi iterations N_A for each calculation.

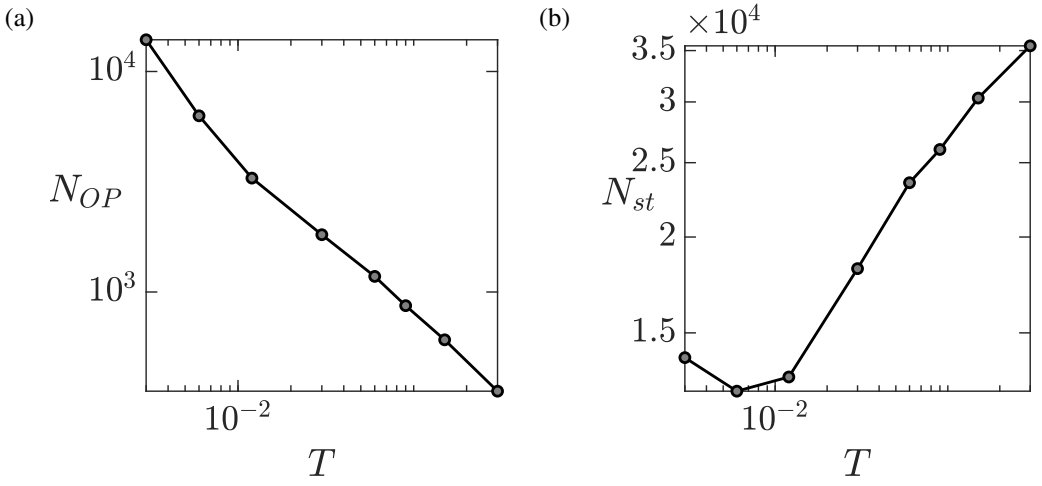

Figure 3.2: Number of matrix-vector multiplications N_{OP} (a) and total number of time steps N_{st} (b) required for the convergence of the Arnoldi method with different values of the integration time T. The case under investigation and the setup of the solver are the same as Table 3.1.

The rate of convergence of an iterative method decreases with the condition number of the Jacobian matrix, which in turn increases as the grid is refined. To address this issue and improve the performance of the method, adequate preconditioning is usually required. Building a preconditioner in a matrix-free context is not a trivial task because the matrix is never formed and standard preconditioning techniques

cannot be directly applied.

To preserve the flexibility of the time-stepping global stability solver, the technique employed to control the convergence must be iterative and matrix-free. As an example, Mack and Peter J. Schmid (2010) proposed a Jacobian-free DNS-based global stability solver for compressible flows with the addition of a preconditioning matrix in explicit form. Instead, Asgharzadeh and Borazjani (2017) addressed this issue through the use of an analytical Jacobian as a preconditioner in a Newton-Krylov method for the implicit solution of the Navier-Stokes equations. Some other options for matrix-free preconditioning are discussed in (Knoll and Keyes, 2004).

The remaining parameter that must be selected by the user is the linearization coefficient ϵ, *i.e.* the amplitude of the discrete perturbation. Its value should result from a trade-off between the truncation error of the finite difference and round-off errors related to the finite precision arithmetic.

Literature provides some guidelines for the appropriate choice of ϵ, the interested reader is referred to the works of Eriksson and Rizzi (1985), Knoll and Keyes (2004), Schulze, P. J. Schmid, and Sesterhenn (2009) and Mack and Peter J. Schmid (2010). In this thesis, it is adopted a commonly used approach that selects the scaling factor of the perturbation at each time-stepper call as

$$\epsilon = \epsilon_0 \frac{\|\boldsymbol{q}_b\|_2 + \|\boldsymbol{q}_p\|_2}{\|\boldsymbol{q}_p\|_2}, \tag{3.21}$$

where $\|\boldsymbol{q}\|_2$ is the L_2 norm of vector $\boldsymbol{q}$ and ϵ_0 is a user-defined parameter related to the truncation error (An, Wen, and Feng, 2011) of the FSI time-stepping scheme.

The choice of ϵ_0 has a great influence on the success of this time-stepping approach, and the user should keep in mind that this task is somewhat solver-dependent. Following the example of Mack and Peter J. Schmid (2010), in A.3 it is reported a parametric study that illustrates the influence of the parameter ϵ_0 on the accuracy of the results obtained for a given configuration.

One final observation can be done regarding the linearized approach. The procedure enables the emergence of exponentially growing modes that are rarely observed in natural systems or in time-marching simulations. The reason lies in the fact that, since a perturbation is usually a superposition of all the modes, the exponential growth is observable only after a long transient, when the leading mode overcomes the others. In reality, the disturbances are not infinitesimal, hence nonlinearity becomes relevant before the exponential growth phase is reached. Constraining the size of the perturbation to a relatively small value, the numerical linearization procedure, instead, enables the emergence of the exponential growth stage.

3.5 Validation case: VIV of an isolated cylinder

The proposed methodology has been first validated with respect to the two-dimensional flow past a fixed circular cylinder, which is the subject of abundant literature in the field of hydrodynamic instability as it is considered the prototype flow around bluff bodies.

For this case, the flow quantities are made dimensionless by taking the diameter of the cylinder D and the incoming flow velocity U_∞ as reference variables. The reported results are obtained over a rectangular domain with size $[-28D : 52D] \times [-28D : 28D]$, with the origin placed on the cylinder axis. A uniform streamwise velocity is imposed at the inlet boundary along with a zero cross-sectional velocity ($u = 1$, $v = 0$), while free-shear boundary conditions are enforced on the lateral boundaries. At the outlet, a convective boundary condition allows the outgoing waves to exit the computational domain with minimal reflections while preserving local continuity. No-slip conditions are applied to the velocity at the surface of the cylinder via the IB procedure described in the previous section. Figure 3.4 illustrates an example of the stretched Cartesian grid used for the computations. To obtain the results here presented, a grid containing 900×570 cells has been employed, with a minimum grid spacing of $0.022D$ attained over a uniformly spaced rectangular region around the cylinder measuring $10D$ in the streamwise direction and $4D$ in the cross-stream direction.

An estimate for the globally unstable eigenvalue ω at $Re = 50$ is reported in Table 3.2 along with results from references (Siconolfi et al. 2017; Negi, Hanifi, and D. S. Henningson, 2020), while Figure 3.3 shows the vorticity (a,b) and streamwise velocity component (c,d) fields of the real (a,c) and imaginary parts (b,d) of the related unstable eigenmode.

Reference	ω	(%)
Siconolfi et al. (2017)	$0.0160 + 0.759i$	2.85
Negi, Hanifi, and D. S. Henningson (2020)	$0.0133 + 0.742i$	0.61
Present	$0.0154 + 0.738i$	-

Table 3.2: Unstable eigenvalue for the flow past a fixed circular cylinder at $Re = 50$. The results obtained with the presented methodology show good agreement with values present in the literature, as indicated by the relative error reported on the right.

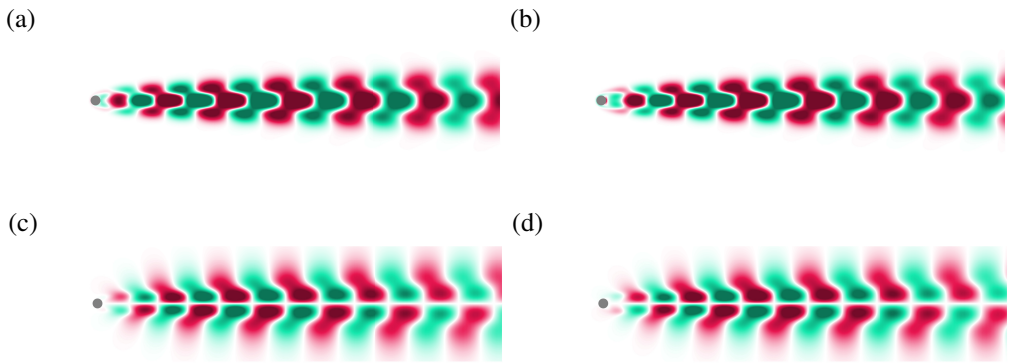

Figure 3.3: Real (left) and imaginary (right) part of vorticity (a,b) and streamwise velocity (c,d) fields for the unstable eigenmode of the flow past a fixed circular cylinder at $Re = 50$. Flow is from left to right.

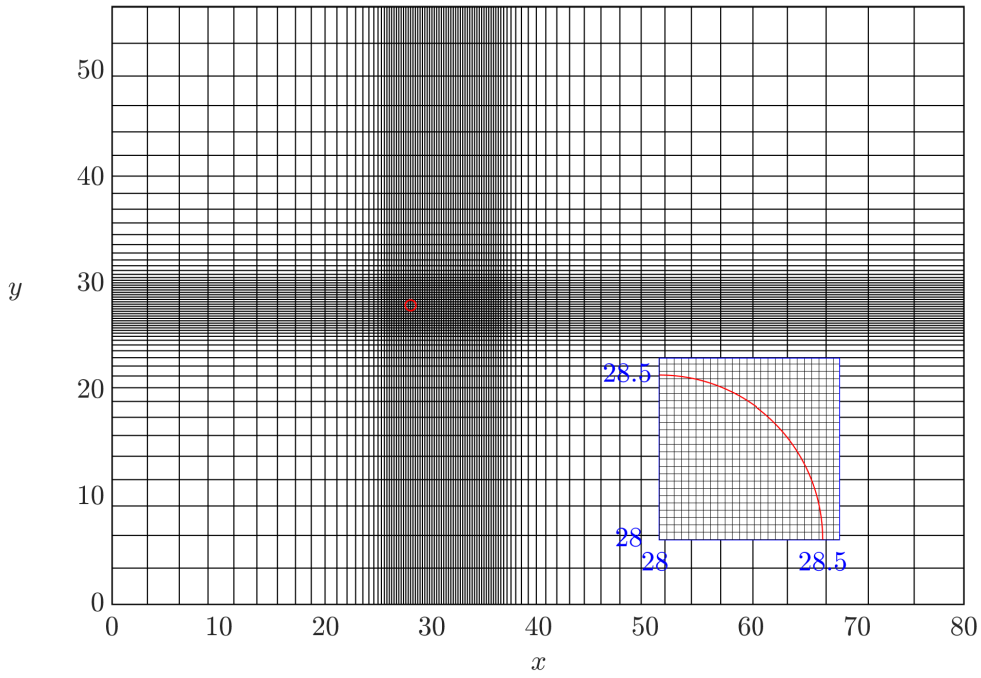

Figure 3.4: Example of a grid used for the linear stability analysis of the flow past a circular cylinder (for both the fixed and oscillating cases). To make the graph more readable, every tenth grid point in each direction is displayed. The inset shows a close-up of the cylinder region for the actual grid employed in the calculations.

The selected validation case for FSI configurations is the linear stability analysis of the VIV of an isolated elastically mounted circular cylinder. This test aims at demonstrating the ability of the IB solver to accurately capture the dynamics of a small perturbation of the fluid-structure system.

The size of the domain and the distance of the center of mass of the cylinder from its

boundaries are the same as in the case of the fixed cylinder, as well as the boundary conditions. For all cases investigated, the Reynolds number based on the cylinder diameter is kept fixed at $Re = 60$, the cylinder being free to oscillate only in the cross-stream direction with no structural damping.

The dynamics of this configuration is governed by three non-dimensional parameters, namely, the Reynolds number Re, the density ratio ρ^*, and the reduced velocity U^*, which gives the ratio of two characteristic time scales of the problem, *i.e.* the period of one natural mode of the body and that of the convective motions of the flow. It is defined as

$$U^* = \sqrt{\frac{A^* \rho^* 4\pi^2}{\xi_y}}. \tag{3.22}$$

For the computations, the same grid used for the case of the fixed cylinder was employed after a grid convergence study. Results and details of the grid refinement study are reported in section A.2 together with an investigation of the influence of the domain size on the accuracy of the results.

In Figure 3.5, it is reported the variation of the non-dimensional frequency and growth rate of the two least stable eigenvalues with the reduced velocity U^*, for two distinct values of the relative density, namely, $\rho^* = 20$ and $\rho^* = 5$. For the largest density ratio, the two leading modes exhibit a clear distinction for each value of the reduced velocity U^*. Following Navrose and S. Mittal (2016), here they are denoted as the *fluid mode* (FM), due to the high affinity that it shows with the wake mode of the fixed cylinder (see Figure 3.6), and the *elastic mode* (EM). This classification is further confirmed by noticing how the frequency of the FM remains close to that of the unstable mode for the flow around a fixed cylinder at the same Reynolds number (see Table 3.1) for all values of U^*, while the frequency of the EM, on the other hand, decreases following the variation of the natural frequency of the cylinder, given by $1/U^*$.

For $\rho^* = 5$, the two modes lose their distinction for intermediate values of U^*, therefore, following Navrose and S. Mittal (2016), they are referred to as the coupled fluid-elastic modes (FEM) I and II. For low values of U^*, modes $FEMI$ and $FEMII$ resemble the stationary wake mode (*i.e.* the mode associated with the vortex-shedding in the wake of the fixed cylinder) and the elastic mode, respectively; however, as U^* increases, the two eigenmodes become coupled and exchange their characteristics (see Figure 3.7).

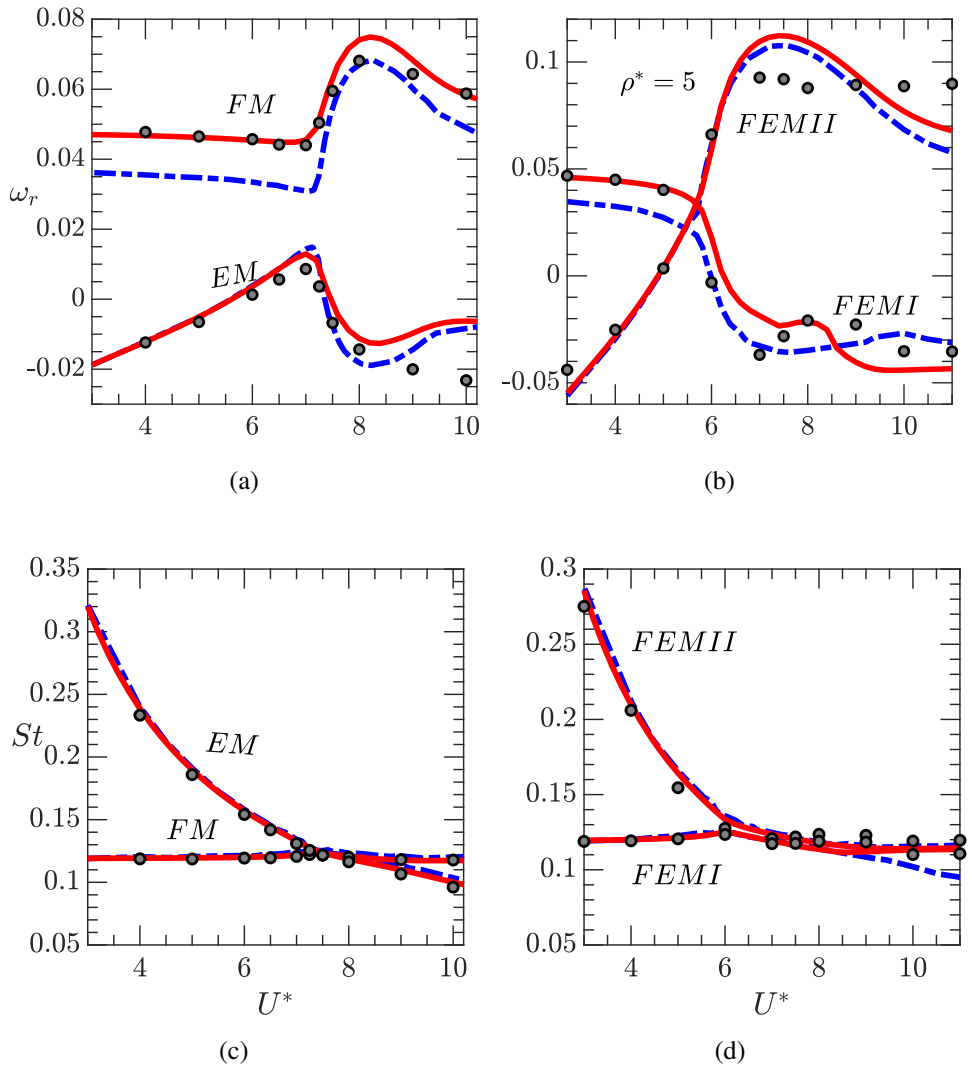

Figure 3.5: Linear stability results: change of the growth rate ω_r and the Strouhal number, $St = (fD)/U_\infty$, of the two least stable modes with U^* for $\rho^* = 20$ (*a*,*c*) and $\rho^* = 5$ (*b*,*d*) at $Re = 60$. Continuous red line: results from Sabino et al. (2020); dashed blue line: results from Navrose and S. Mittal (2016); gray circles: present results. The red curves were reproduced using the open-source Matlab drivers of the StabFem project (StabFem).

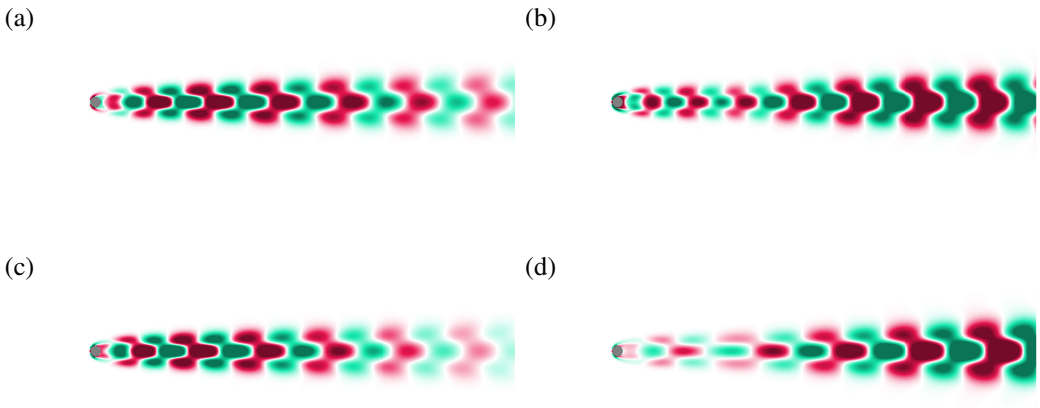

Figure 3.6: Spanwise vorticity field of the real part of FM (a,c) and EM (b,d) for ($Re = 60, \rho^* = 20$) at $U^* = 7$ (a,b) and $U^* = 9$ (c,d). The fluid flows from left to right. The fluid mode closely resembles the unstable mode for a fixed cylinder reported in Figure 3.3

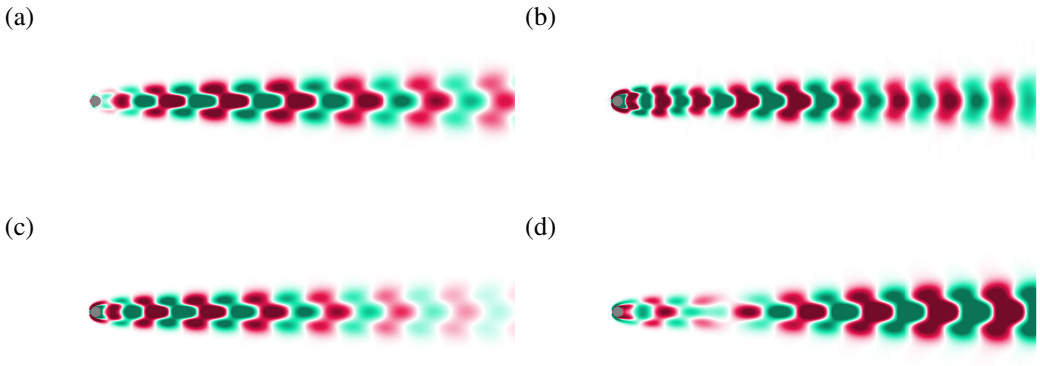

Figure 3.7: Spanwise vorticity field of the real part of FEMI (a,c) and FEMII (b,d) for ($Re = 60, \rho^* = 5$) at $U^* = 5$ (a,b) and $U^* = 6$ (c,d). The fluid flows from left to right.

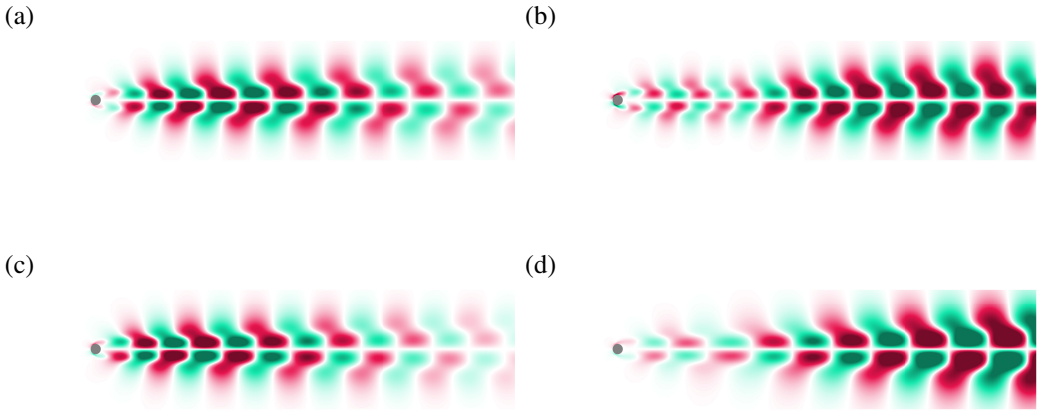

Figure 3.8: Streamwise velocity field of the real part of FM (a,c) and EM (b,d) for ($Re = 60, \rho^* = 20$) at $U^* = 7$ (a,b) and $U^* = 9$ (c,d). The fluid flows from left to right.

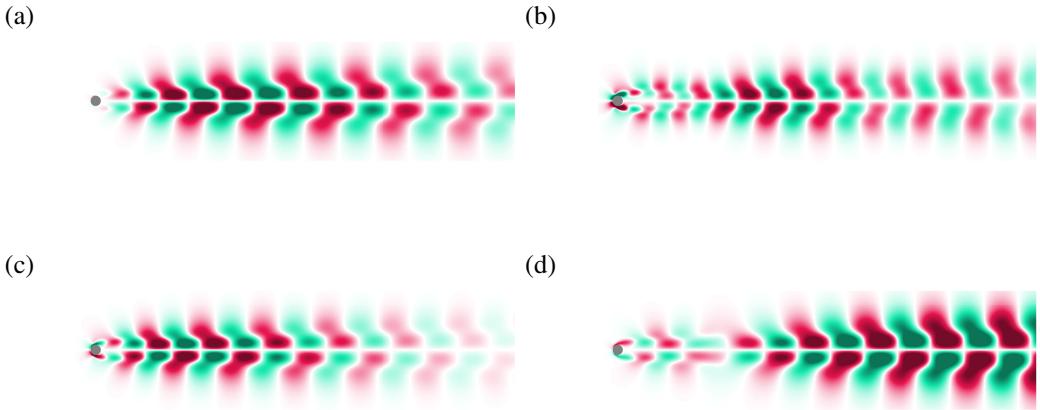

Figure 3.9: Horizontal velocity field of the real part of FEMI (a,c) and FEMII (b,d) for ($Re = 60, \rho^* = 5$) at $U^* = 5$ (a,b) and $U^* = 6$ (c,d). The fluid flows from left to right.

References

An, Heng-Bin, Ju Wen, and Tao Feng (2011). "On finite difference approximation of a matrix-vector product in the Jacobian-free Newton–Krylov method". In: *Journal of Computational and Applied Mathematics* 236.6, pp. 1399–1409. ISSN: 0377-0427. DOI: https://doi.org/10.1016/j.cam.2011.09.003.

Asgharzadeh, Hafez and Iman Borazjani (2017). "A Newton–Krylov method with an approximate analytical Jacobian for implicit solution of Navier–Stokes equations on staggered overset-curvilinear grids with immersed boundaries". In: *Journal of Computational Physics* 331, pp. 227–256. ISSN: 0021-9991. DOI: https://doi.org/10.1016/j.jcp.2016.11.033.

Bhatia, N.P. and G.P. Szegö (1970). *Stability Theory of Dynamical Systems*. Grundlehren der mathematischen Wissenschaften in Einzeldarstellungen mit besonderer Berücksichtigung der Anwendungsgebiete. Springer-Verlag. URL: https://link.springer.com/book/9783540427483.

Chiba, Satoshi (1998). "Global stability analysis of incompressible viscous flow". In: *Journal of Japan Society of Computational Fluid Dynamics* 7, 20–48 (In Japanese).

Citro, V. et al. (2017). "Efficient stabilization and acceleration of numerical simulation of fluid flows by residual recombination". In: *Journal of Computational Physics* 344, pp. 234–246. ISSN: 0021-9991. DOI: https://doi.org/10.1016/j.jcp.2017.04.081.

de Tullio, M.D. et al. (2007). "An immersed boundary method for compressible flows using local grid refinement". In: *Journal of Computational Physics* 225.2, pp. 2098–2117. ISSN: 0021-9991. DOI: https://doi.org/10.1016/j.jcp.2007.03.008.

Durbin, P.A and G Iaccarino (2002). "An Approach to Local Refinement of Structured Grids". In: *Journal of Computational Physics* 181.2, pp. 639–653. ISSN: 0021-9991. DOI: https://doi.org/10.1006/jcph.2002.7147.

Edwards, W.S. et al. (1994). "Krylov Methods for the Incompressible Navier-Stokes Equations". In: *Journal of Computational Physics* 110.1, pp. 82–102. ISSN: 0021-9991. DOI: https://doi.org/10.1006/jcph.1994.1007.

Eriksson, Lars E and Arthur Rizzi (1985). "Computer-aided analysis of the convergence to steady state of discrete approximations to the euler equations". In: *Journal of Computational Physics* 57.1, pp. 90–128. ISSN: 0021-9991. DOI: https://doi.org/10.1016/0021-9991(85)90054-3.

Goldhirsch, L., S.A. Orszag, and B.K. Maulik (1987). "An efficient method for computing leading eigenvalues and eigenvectors of large asymmetric matrices". In: *Journal of Scientific Computing* 2.1, pp. 33–58. ISSN: 0885-7474. DOI: https://doi.org/10.1007/BF01061511.

Gómez, Francisco, Ricky Gomez, and V. Theofilis (June 2011). "Coupling time-stepping numerical methods and standard aerodynamics codes for instability analysis of flows in complex geometries". In: *6th AIAA Theoretical Fluid Mechanics Conference*. DOI: 10.2514/6.2011-3753.

Gómez, Francisco, José Miguel Pérez, et al. (2015). "On the use of matrix-free shift-invert strategies for global flow instability analysis". In: *Aerospace Science and Technology* 44. Instability and Control of Massively Separated Flows, pp. 69–76. ISSN: 1270-9638. DOI: https://doi.org/10.1016/j.ast.2014.11.003.

Knoll, D.A. and D.E. Keyes (2004). "Jacobian-free Newton–Krylov methods: a survey of approaches and applications". In: *Journal of Computational Physics* 193.2, pp. 357–397. ISSN: 0021-9991. DOI: https://doi.org/10.1016/j.jcp.2003.08.010.

Lehoucq, R. B., D. C. Sorensen, and C. Yang (1998). *ARPACK Users' Guide*. Society for Industrial and Applied Mathematics. DOI: 10.1137/1.9780898719628. eprint: https://epubs.siam.org/doi/pdf/10.1137/1.9780898719628.

Mack, Christoph J. and Peter J. Schmid (2010). "A preconditioned Krylov technique for global hydrodynamic stability analysis of large-scale compressible flows". In: *Journal of Computational Physics* 229.3, pp. 541–560. ISSN: 0021-9991. DOI: https://doi.org/10.1016/j.jcp.2009.09.019.

Mettot, Clément, Florent Renac, and Denis Sipp (July 2014). "Computation of eigenvalue sensitivity to base flow modifications in a discrete framework: Application to open-loop control". In: *Journal of Computational Physics* 269, pp. 234–258. DOI: 10.1016/j.jcp.2014.03.022.

Navrose and Sanjay Mittal (2016). "Lock-in in vortex-induced vibration". In: *Journal of Fluid Mechanics* 794, pp. 565–594. DOI: 10.1017/jfm.2016.157.

Negi, P. S., A. Hanifi, and D. S. Henningson (2020). "On the linear global stability analysis of rigid-body motion fluid–structure-interaction problems". In: *Journal of Fluid Mechanics* 903, A35. DOI: 10.1017/jfm.2020.685.

Orlandi, Paolo (2001). *Fluid Flow Phenomena - A Numerical Toolkit*. 1st ed. Fluid Mechanics and Its Applications. Springer Dordrecht. DOI: https://doi.org/10.1007/978-94-011-4281-6.

Sabino, D. et al. (2020). "Vortex-induced vibration prediction via an impedance criterion". In: *Journal of Fluid Mechanics* 890. DOI: 10.1017/jfm.2020.104.

Schmid, Peter J. and Dan Henningson (Jan. 2001). *Stability and Transition in Shear Flows*. Vol. 142. ISBN: 9780387989853. DOI: 10.1007/978-1-4613-0185-1.

Schulze, J. C., P. J. Schmid, and J. L. Sesterhenn (2009). "Exponential time integration using Krylov subspaces". In: *International Journal for Numerical Methods in Fluids* 60.6, pp. 591–609. DOI: https://doi.org/10.1002/fld.1902. eprint: https://onlinelibrary.wiley.com/doi/pdf/10.1002/fld.1902.

Seo, Jung Hee and Rajat Mittal (Aug. 2011). "A Sharp-Interface Immersed Boundary Method with Improved Mass Conservation and Reduced Spurious Pressure Oscillations". In: *Journal of computational physics* 230, pp. 7347–7363. DOI: 10.1016/j.jcp.2011.06.003.

Siconolfi, L. et al. (2017). "Towards a quantitative comparison between global and local stability analysis". In: *Journal of Fluid Mechanics* 819, pp. 147–164. DOI: 10.1017/jfm.2017.167.

Sorensen, Danny (Jan. 2002). "Sorensen D.C.: Numerical methods for large eigenvalue problems. Acta Numerica 11, 519-584". In: *Acta Numerica* 11, pp. 519–584. DOI: 10.1017/S0962492902000089.

Sorensen, Danny C. (1992). "Implicit Application of Polynomial Filters in a k-Step Arnoldi Method". In: *SIAM J. Matrix Anal. Appl.* 13, pp. 357–385.

Tezuka, Asei and Kojiro Suzuki (2006). "Three-Dimensional Global Linear Stability Analysis of Flow Around a Spheroid". In: *AIAA Journal* 44.8, pp. 1697–1708. DOI: 10.2514/1.16632. eprint: https://doi.org/10.2514/1.16632.

Theofilis, V. and Tim Colonius (June 2011). "Special issue on global flow instability and control". In: *Theoretical and Computational Fluid Dynamics* 25, pp. 1–6. DOI: 10.1007/s00162-010-0217-3.

Theofilis, Vassilios (2003). "Advances in global linear instability analysis of nonparallel and three-dimensional flows". In: *Progress in Aerospace Sciences* 39.4, pp. 249–315. ISSN: 0376-0421. DOI: https://doi.org/10.1016/S0376-0421(02)00030-1. URL: https://www.sciencedirect.com/science/article/pii/S0376042102000301.

Uhlmann, Markus (July 2003). *First Experiments with the Simulation of Particulate Flows*.

Vanella, Marcos and Elias Balaras (2009). "A moving-least-squares reconstruction for embedded-boundary formulations". In: *Journal of computational physics (Print)* 228.18, pp. 6617–6628.

Yang, Jianming and Elias Balaras (June 2006). "An embedded-boundary formulation for large-eddy simulation of turbulent flows interacting with moving boundaries". In: *Journal of Computational Physics* 215, pp. 12–40. DOI: 10.1016/j.jcp.2005.10.035.

Yang, Xiaolei et al. (Nov. 2009). "A smoothing technique for discrete delta functions with application to immersed boundary method in moving boundary simulations". In: *Journal of Computational Physics* 228, pp. 7821–7836. DOI: 10.1016/j.jcp.2009.07.023.

Chapter 4

VORTEX-INDUCED VIBRATIONS OF CYLINDERS IN TANDEM

Practical application is found by not looking for it, and one can say that the whole progress of civilization rests on that principle.

Jacques Hadamard

In this chapter, the vortex-induced vibrations of two identical elastically mounted rigid cylinders in tandem arrangement is investigated numerically. The dynamics of the system is initially explored by means of time-marching simulations, carried out with the solver presented in Chapter 2.

Subsequently, the leading eigenvalues of the system are computed at $Re = 100$ by using the time-stepping procedure introduced in Chapter 3. To the author's knowledge, linear stability had not been yet applied to fluid-structure interaction problems involving multiple bodies, without any approximation made about the dynamic coupling between the solid and the fluid.

The obtained results provide further confidence in the robustness of the method and open the way to the instability analysis of generic multi-body configurations. Besides, the linear predictions could explain the change of behavior of the system that happens for $U^* = 5$ and that has been observed in previous studies.

4.1 Introduction

The case considered in this chapter is the configuration proposed by Borazjani and Sotiropoulos (2009), with two identical elastically mounted cylinders in tandem arrangement placed in a free-stream flow. This configuration is a prototype problem for cross-flow-induced vibrations of interfering bodies, such as offshore structures, submerged pipelines, and overhead transmission cables.

These systems are known to develop self-excited oscillations, and this is in general not worrisome as far as their amplitudes remain small. This may not be the case in presence of the *lock-in* phenomenon, during which the oscillation frequency is

close to the natural frequency of the cylinder in vacuum. For supercritical Reynolds numbers, *i.e.* Reynolds numbers bigger than the instability threshold for the fixed configuration, lock-in is seen to occur for a certain range of U^*. It has been also observed through numerical and experimental investigations that the lock-in region of U^* for the tandem arrangement is wider than that for the isolated cylinder case explored in Chapter 3.

A parametric exploration of the nonlinear dynamics of the system is beyond the scope of the current work, the number of publications on the subject being already consistent. The purpose of this work is thus to assess the robustness of the methodology with respect to multi-body configurations. The analysis here is restricted to the 1–DOF case in which the cylinders are free to oscillate only in the cross-stream direction. The streamwise distance between their centers is equal to 1.5 diameters, while the cross-stream offset is zero. No structural damping is considered and the solid-to-fluid density ratio is kept constant at $\rho^* = 2.546$ for all simulations. Given the low value of the density ratio and the close proximity of the cylinders, the problem under investigation represents a more challenging test case compared to the single-cylinder problem investigated in Chapter 3.

At first, the nonlinear response of the cylinders is reported for a diameter-based Reynolds number $Re = 200$, for values of the reduced velocity spanning the range $1.5 \leq U^* \leq 14$. A sketch of the computational domain along with the boundary conditions employed is shown in Figure 4.1. The inlet is located at a distance $L_{in} = 15D$ from the midpoint between the centers of the cylinders, with the total length of the domain being equal to $L_{in} + L_{out} = 55D$, while the lateral boundaries are placed at a distance $L_{lat} = 15D$ from the centers. A uniform Dirichlet boundary condition is given at the inlet and on the lateral boundaries, and a convective condition is assigned at the outlet with a convective velocity $c = 0.8$. In Figure 4.1, x is the streamwise direction and y is the cross-stream coordinate direction. The computations have been performed over a stretched Cartesian grid containing 900×520 cells, with a minimum grid spacing of $0.0154D$ in the regularly spaced box region around the origin, measuring $4D$ in each direction.

All simulations have been initialized with the steady base flow computed via *Boost-Conv* (Citro et al. 2017) by keeping the cylinders fixed at their initial positions. This is allowed since the configuration is symmetrical with respect to a horizontal axis passing through the centers of the cylinders. No starting perturbation is superposed to the stabilized solution; thus, the initial departure from the basic state is triggered only by round-off errors. Figure 4.2 shows the temporal evolution of

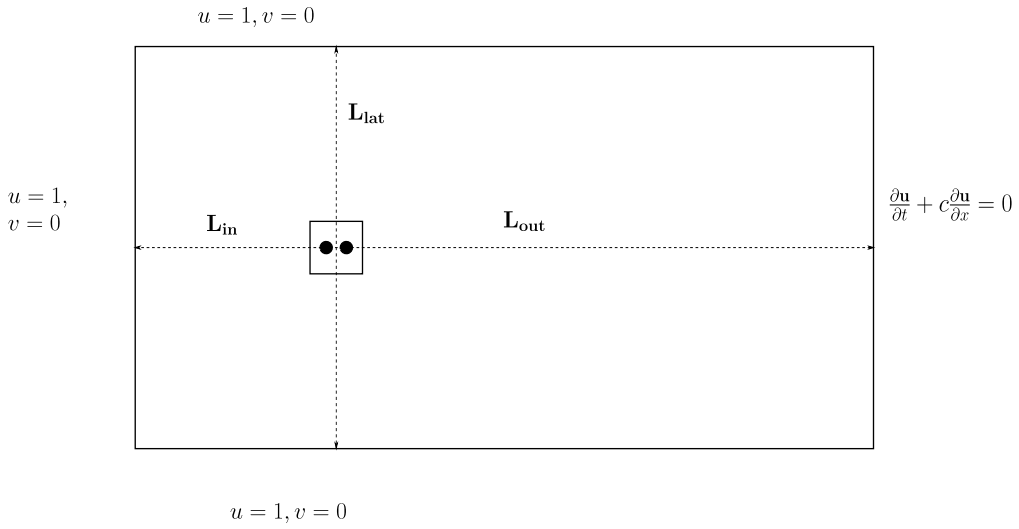

Figure 4.1: Sketch of the computational domain employed for the direct numerical simulations of the flow interacting with two circular cylinders in tandem arrangement at $Re = 200$.

the position of the centers of mass of the two cylinders for different values of U^*, each one being representative of a distinct behavior of the system. For $U^* = 3$ (see Figure 4.2a) the cylinders experience a longer transient phase characterized by low-amplitude vibrations before reaching a periodic regime where the two cylinders oscillate out-of-phase with the front one exhibiting higher amplitude than the rear. Borazjani and Sotiropoulos (2009) classified this behavior as state 1 of the system, referring to the vibration state where the rear cylinder achieves a larger oscillation amplitude as state 2. When the reduced velocity is increased to $U^* = 4$, the dynamic response of the fluid-structure system changes noticeably as the two cylinders exhibit a quasi-periodic behavior distinguished by larger amplitudes of vibration that undergo a low-frequency modulation in time. As can be seen from the close-up region in Figure 4.2b, such modulations come with a change in the phase difference between the two oscillatory motions, as the phase angles are generally out of phase, but match periodically.

As the reduced velocity is further increased to $U^* = 5$, a shift from state 1 to state 2 is observed as the two cylinders oscillate in phase opposition, with the rear one exhibiting greater amplitude than the front one. For higher values of the reduced velocity, there is no qualitative change in the dynamical response of the system. The trailing cylinder continues to oscillate at a higher amplitude and out-of-phase with respect to the front one. Figure 4.3a shows the variation of the maximum displacement A^*_{MAX} with the reduced velocity for each cylinder; the value A^*_{MAX}

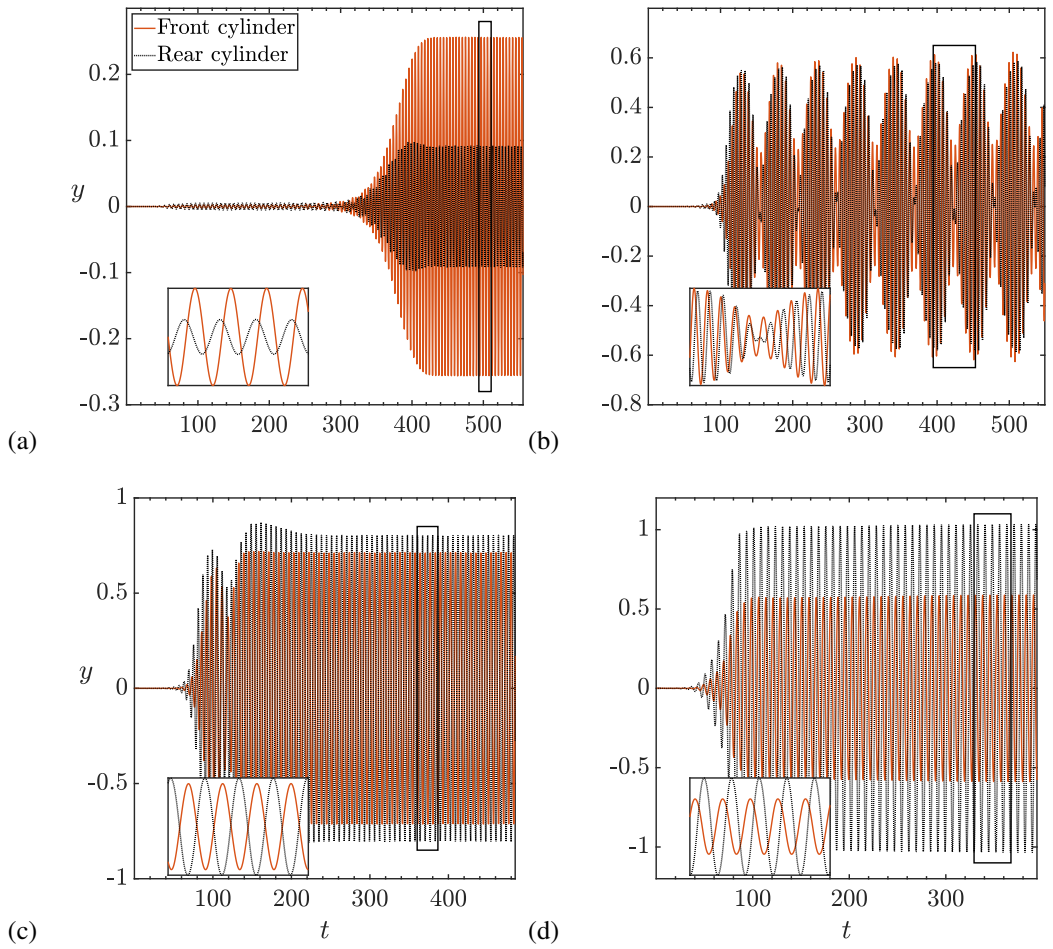

Figure 4.2: Flow past two freely vibrating cylinders in tandem at $(Re, \rho^*) = (200, 2.546)$: time evolution of the vertical nondimensional displacement of the cylinders for different values of U^*; (a): $U^* = 3$; (b): $U^* = 4$; (c): $U^* = 5$; (d): $U^* = 7$. The inset in the lower-left corner of each figure provides a zoom-in of the region delimited by the black rectangle.

was measured disregarding the early transient phase. Results from Borazjani and Sotiropoulos (2009) and Griffith et al. (2017) are also included for comparison, showing a good overall agreement with the present outcome. The main discrepancy observed for the higher values of U^* can be ascribed to the different initial conditions. To verify this assumption, the computations were repeated for $11 \leq U^* \leq 14$ starting from a snapshot of the unsteady solution at $U^* = 10$; the results, represented in Figure 4.3a by dashed lines, are markedly closer to the data present in the literature. These findings could indicate the existence of a hysteresis effect, already observed for the case of two stationary cylinders in tandem (Papaioannou et al. 2006) and for the VIV of a single cylinder (Prasanth and Mittal, 2009; Singh and

Mittal, 2005). Figure 4.4 reports the vorticity contours throughout an oscillation

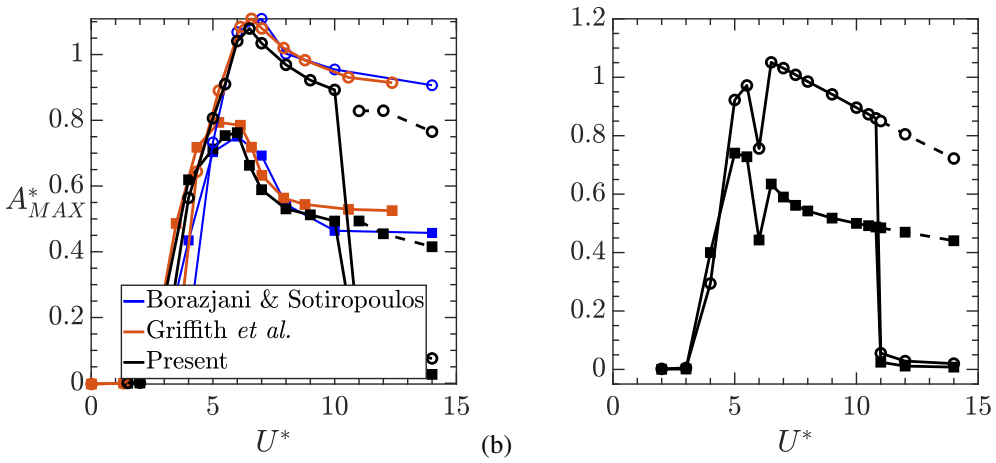

Figure 4.3: Variation with the reduced velocity U^* of the maximum non-dimensional displacement A^*_{MAX} of two identical cylinders in tandem ($L = 1.5$) at $Re = 200$ (a) and $Re = 100$ (b). Squares: front cylinder; circles: rear cylinder. The present results for $Re = 200$ are compared with the ones from Borazjani and Sotiropoulos (2009) and Griffith et al. (2017). Dashed line: the simulations were initialized from an instantaneous snapshot of the solution for a smaller value of U^*.

cicle at $Re = 100$ for $U^* = 6$. In this case, the cylinders oscillate out-of-phase, and the rear cylinder exhibits larger amplitudes. As shown in Figure 4.3a, for $U^* = 6$ the difference between the peak displacements of the cylinders is maximum. Due to the higher (periodic) spacing between the cylinders, a vortex pair starts forming in the gap, but the ascending (or descending, depending on the position in the cycle) rear cylinder cuts through the shear layer of the front one, thus vortices actually detach from the rear cylinder. This mode is referred to as $2P$ vortex shedding since two vortex pairs are shed per cycle.

Results obtained by running simulations of the same configuration at $Re = 100$ are presented in Figure 4.3b; the behavior of the system is found to depend strongly on the reduced velocity with a good qualitative agreement with the $Re = 200$ case. Time traces of the displacements of the two cylinders are reported in Figure 4.5 for four different values of the reduced velocity, along with the spectral content of the time history of the vertical separation Δy between the centers of the two cylinders. For low values of the reduced velocity, the cylinders are found to oscillate in phase with small amplitudes, indicating that they are still outside the lock-in regime. For $U^* = 3$ (see Figure 4.5a), the phase difference between the front and rear cylinders is small, with the rear one exhibiting somewhat larger displacements.

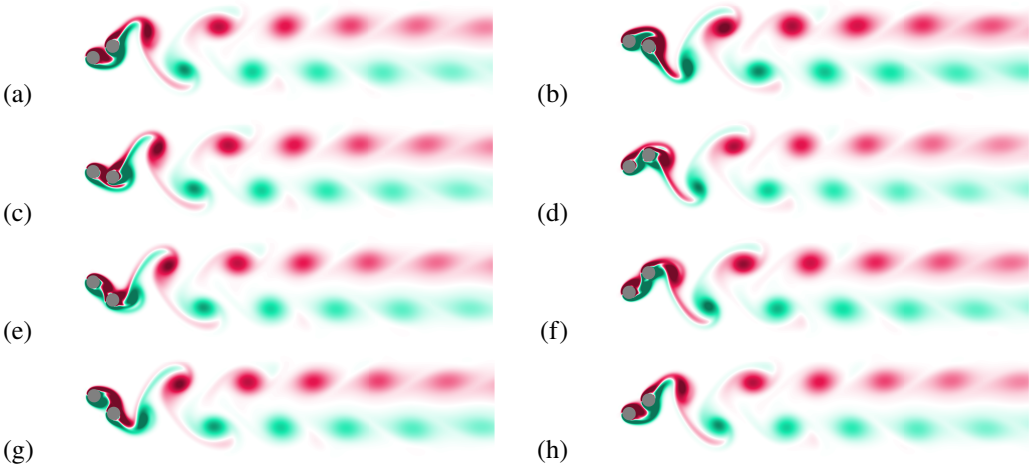

Figure 4.4: Vorticity contours of the tandem cylinder arrangement for $U^* = 6$ and $Re = 100$. The figures describe (from (a) to (h)) a complete oscillation cycle.

When the reduced velocity is increased to $U^* = 4$, the dynamic response of the system changes considerably as the cylinders enter the lock-in regime, oscillating out-of-phase at a higher frequency and with the front cylinder now exhibiting wider oscillations. As the velocity is further increased to $U^* = 5$, a change in the behavior of the system is observed again since the rear cylinder now oscillates with larger relative amplitude, while the vertical separation between the cylinders undergoes oscillations with a periodic amplitude modulation that closely resembles a beating motion. This observation is confirmed by looking at the frequency content in Figure 4.5c, which shows two main peaks having similar frequencies. In a linear system, the superposition of these two harmonics would result in a beating frequency, given by $f_b = |f_2 - f_1|$, and a corresponding period of about 97 time units, which is very close to the characterizing period of the oscillations of both cylinders. This beating phenomenon disappears by further increasing the reduced velocity as the frequency of vibration diminishes. It is interesting to notice that Borazjani and Sotiropoulos (2009) identified $U^* = 5$ as the critical state of the system at $Re = 200$, delimiting the transition from state 1 to state 2.

Global stability

In this section, the interaction between the fluid and the two elastically mounted cylinders in tandem is investigated through a global linear stability analysis, to further ascertain the validity and robustness of the proposed methodology.
The computations have been performed on the same grid used to conduct the flow analysis presented in the previous section. Given the low value of the density ratio

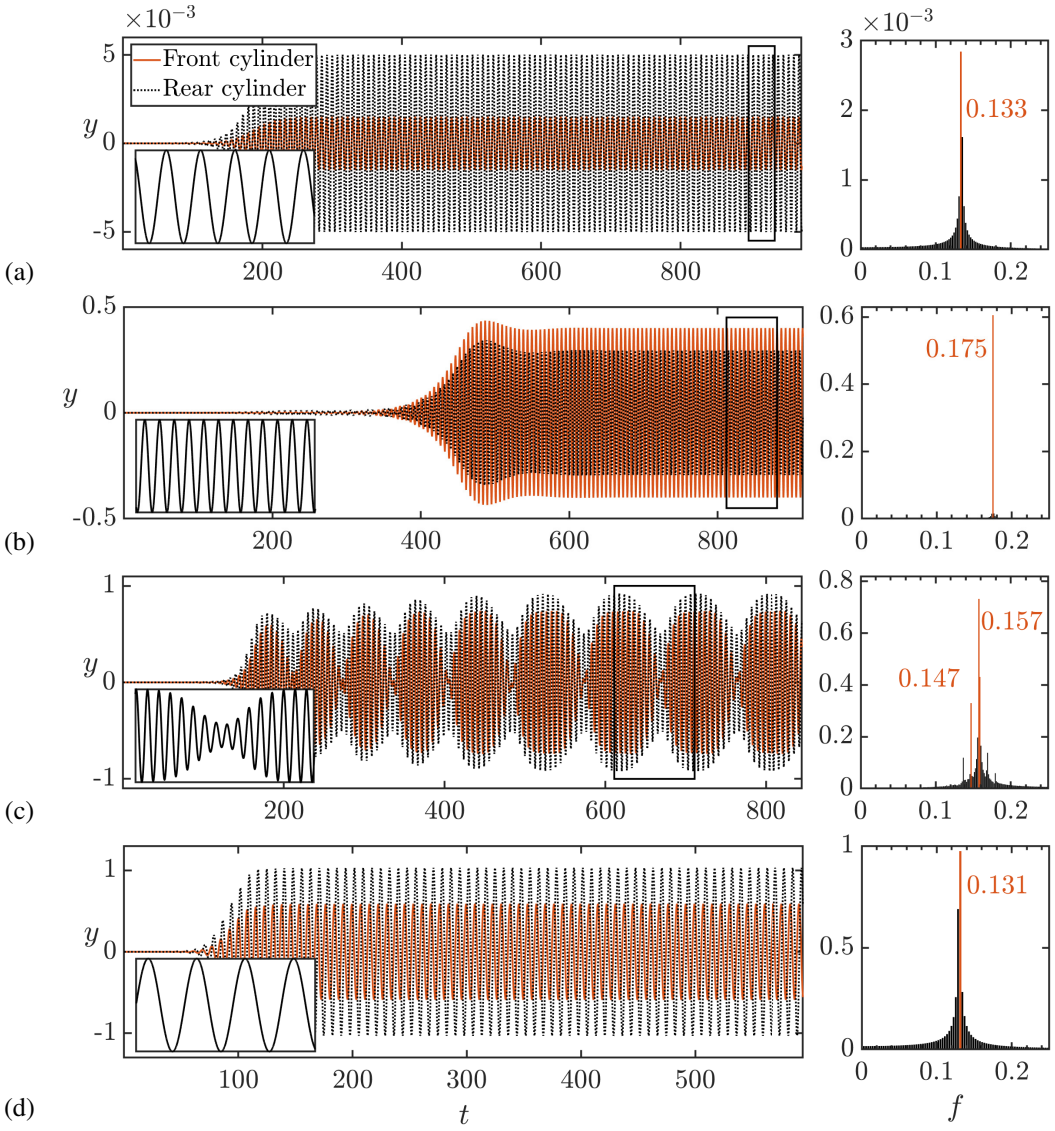

Figure 4.5: Flow past two freely vibrating cylinders in tandem arrangement at $(Re, \rho^*) = (100, 2.546)$: time evolution of the vertical displacement of the cylinders for different values of U^*; *a*: $U^* = 3$; *b*: $U^* = 4$; *c*: $U^* = 5$; *d*: $U^* = 7$. The inset in the lower-left corner of each figure shows the time history of the vertical distance Δy_c between the cylinders for the time interval marked by the black rectangle. On the right, it is reported the single-sided amplitude spectrum of Δy_c.

ρ^*, the results of the nonlinear simulations obtained with a weak coupling of the fluid and solid dynamics were compared with those obtained via a strong coupling. Even though the two procedures exhibited very similar results, the iterative procedure provided more accurate results with a reduced number of Arnoldi iterations for the stability calculations. The fixed time-step size was chosen in order to keep the CFL number under the 0.4 value. As in the case of the single cylinder, the linear

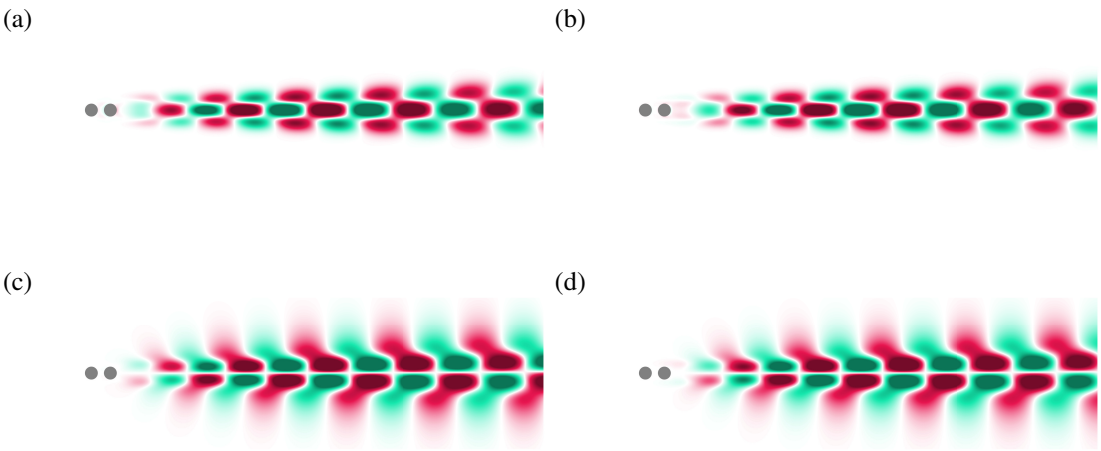

Figure 4.6: Real (a,c) and imaginary (b,d) parts o the modal vorticity (a,b) and horizontal velocity component (c,d) of the unstable eigenmode for the flow past two stationary cylinders in tandem arrangement at $Re = 100$.

stability analysis of the fluid alone predicts the existence of an unstable eigenvalue $\omega_s = 0.0404 + 0.7907i$ associated with the vortex shedding in the wake of the two cylinders. In the following, this eigenvalue is referred to as the *stationary wake mode*. The corresponding eigenmode (see Figure 4.6) closely resembles the unstable eigenmode of the single cylinder case. This observation is consistent with results from literature asserting that, for small streamwise spacings, the two cylinders shed like a single body (Papaioannou et al. 2006).

When the cylinders are free to move in the cross-stream direction, the LSA identifies the presence of an additional eigenmode for the range of parameters considered. In Figure 4.7, the two least stable eigenvalues are tracked over a wide range of reduced velocities, in an attempt to identify the mechanisms responsible for the lock-in regime and for the change of behavior that occurs around $U^* = 5$. It is observed that, for the lower values of U^*, the two leading modes are quite distinct, with the frequency of the first mode (represented by blue dots in Figure 4.7b and Figure 4.7d) being close to the nondimensional frequency of the stationary wake mode, $f_s D/U_\infty = 0.1258$. Conversely, the frequency associated with the second mode (red dots in Figure 4.7b and Figure 4.7d) is slightly smaller than the natural frequency of the cylinders for values of the reduced velocity up to $U^* = 7$, where the frequencies of the two modes are almost coincident and remarkably close to that of the limit cycle shown in Figure 4.5d. Therefore, for the lower values of U^*, the first mode is associated with the wake instability and the second one with the structural mode. For $U^* = 5$ the two modes show comparable growth rates and close frequencies, flagging an

interaction that is visible in the nonlinear evolution as well. The peak frequencies revealed by the amplitude spectrum on the right side of Figure 4.5c are, indeed, quite close to the frequencies of the leading modes at $U^* = 5$ reported in Figure 4.7d. After the crossing of the two modes, both frequencies remain close to that of the stationary wake mode for all U^*, and a classification of the modes as fluid mode and structural mode is not possible.

For values of the reduced velocity lower than $U^* = 4$, the mode associated with

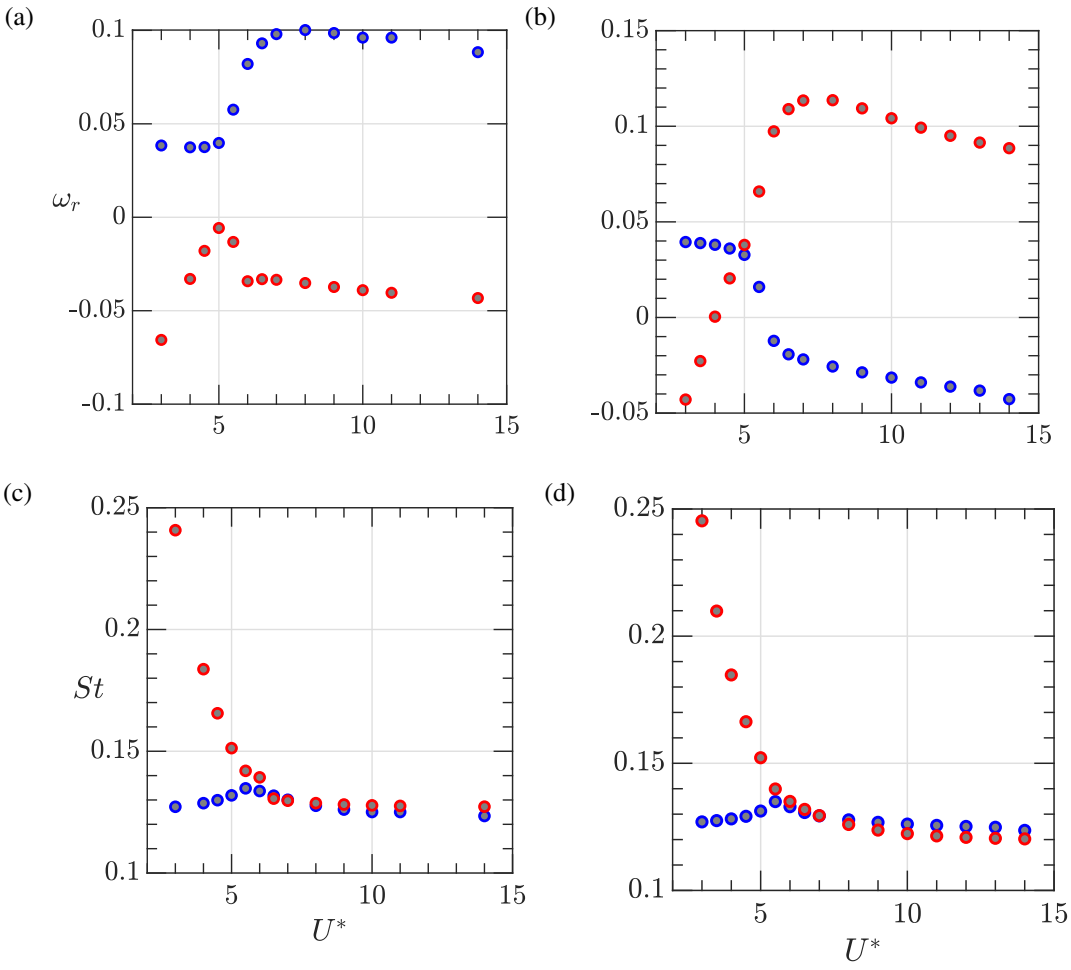

Figure 4.7: Results of the LSA for the flow around two elastically-mounted cylinders in tandem at $Re = 100$. Evolution with U^* of the growth rate ω_r and the Strouhal number St of the two least stable modes. Fig. (a,c): only the rear cylinder is free to oscillate; fig. (b,d): both cylinders are free to move.

the structure is still stable. This finding is coherent with the small amplitude of oscillation observed in the calculations. Then, at the critical value $U^* = 5$, the growth rate of mode 2 surpasses that of mode 1, possibly explaining the transition from state 1 to state 2 and the greater amplitudes of vibration observed in the

nonlinear simulations. In an attempt to shed further light on this phenomenon, in Figure 4.7a and Figure 4.7c are reported the growth rate and the frequency, respectively, of the two least stable modes for the same tandem arrangement when only the rear cylinder is free to move. For this configuration, the results show that the growth rate of the unstable mode increases considerably for $U^* \geq 5$, while the growth rate of the stable mode attains its maximum value.

These findings indicate that the mechanism responsible for the large amplitude oscillations is already present in this fixed-free case. The temporal evolution of the flow starting from the base state shows that, for all the values of the reduced velocity, a regular vortex street excites the oscillation of both cylinders, with the rear one undergoing larger vibrations. This is due to the fact that vortices are initially shed only from the rear cylinder, which thus experiences a greater pressure difference. The outcome is coherent with the observations of Borazjani and Sotiropoulos (2009), who suggest that it is the vortex-shedding in the wake that initiates the excitation of the system and subsequently generates a vertical separation between the cylinders. When this separation becomes large enough, other interaction mechanisms come into play and give rise to different dynamical states.

There is, however, another point to address which is the passage from state 2 to state 1 that is observed when changing the value of U^* from $U^* = 3$ to $U^* = 4$ and the switch from state 1 to state 2 that occurs at $U^* = 5$. To investigate this phenomenon, in Figure 4.8 the early transient is reported of the time history of the vertical displacement of the cylinders for $U^* = 4$. It is clearly visible that the cylinders oscillate almost in phase, with a low amplitude of vibration as in the case $U^* = 3$ (Figure 4.8b) and the rear cylinder exhibits larger oscillations, following the characteristics of the first mode. The temporal evolution shows that the growth of the first mode saturates as the oscillations approach a limit cycle with a small amplitude. Later, the cylinders lose their synchronization owing to the emergence of the second mode. The greater amplitude of vibration of the front cylinder, however, cannot be explained with linear arguments. For $U^* > 5$, the dynamics of the linearized system is governed by the second mode, characterized by the counter-phase oscillation of the cylinders, with the rear one undergoing larger vibrations.

Figure 4.9 shows the vorticity fields of the two unstable eigenmodes related to the eigenvalues reported in Figure 4.7, for three different values of the reduced velocity. Again, for $U^* = 3$ and $U^* = 4$, mode 1 resembles the stationary wake mode of Figure 4.6 but departs from it for the higher values of U^*. On the other hand, the shape of mode 2 also changes when the reduced velocity is increased from $U^* = 4$

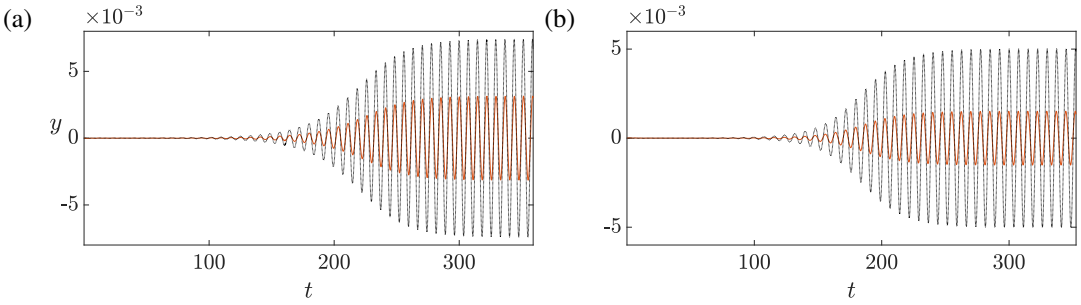

Figure 4.8: Time evolution of the vertical displacement of two freely vibrating cylinders in tandem arrangement at $(Re, \rho^*) = (100, 2.546)$ for $U^* = 4$ (a) and $U^* = 3$ (b).

to $U^* = 5$, while a further increase in the value of U^* produces a shift upstream of the high vorticity region. Figure 4.10 confirms this observation by showing the streamwise real velocity components of the leading modes for the same values of U^*. For $U^* = 3$, mode 2 is clearly a structural mode, as the flow far from the cylinders is slightly perturbed, while mode 1 is clearly the wake mode. As U^* increases, the two modes lose their clear distinction.

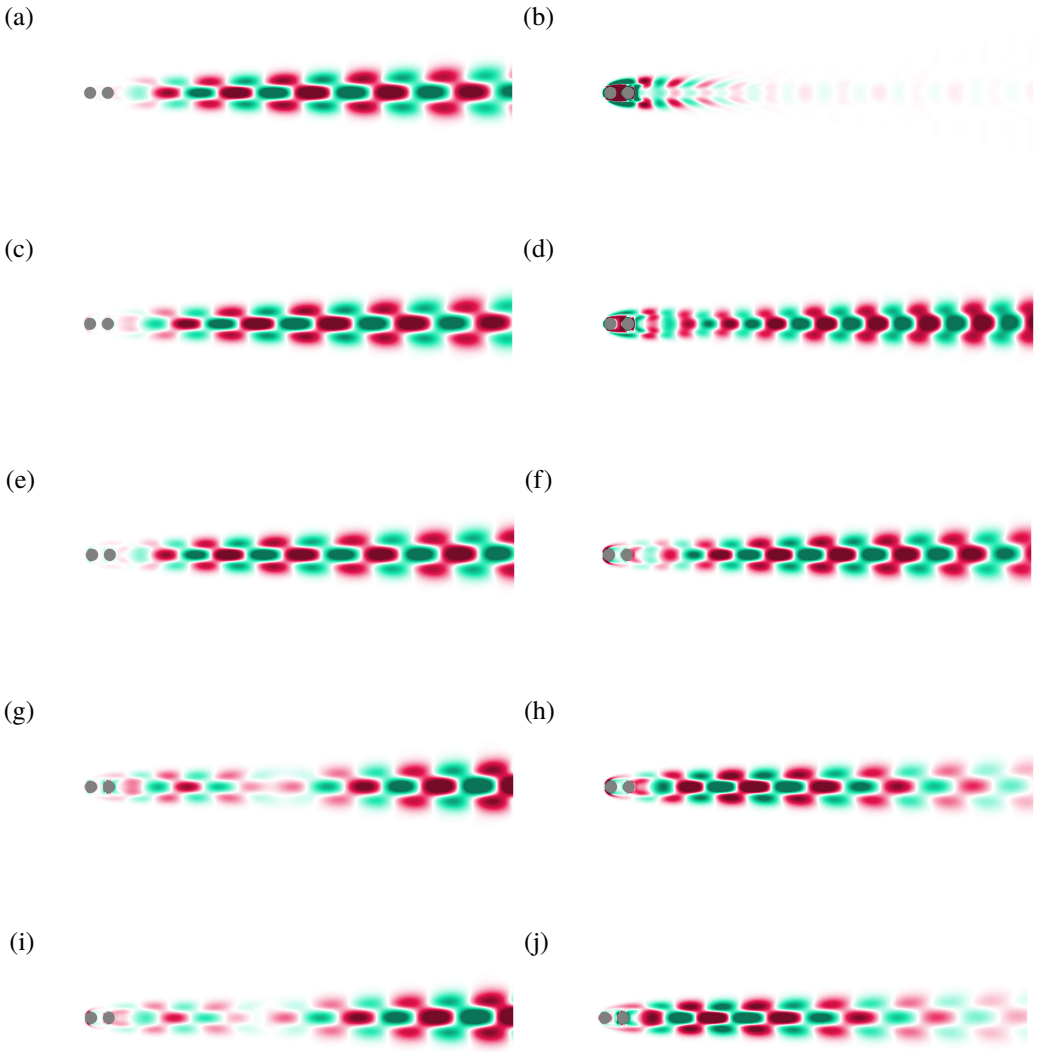

Figure 4.9: Flow past two spring-mounted circular cylinders in tandem arrangement at $Re = 100$. Spatial distribution of the vorticity of the real part of mode 1 (a,c,e,g,i) and mode 2 (b,d,f,h,j) for $U^* = 3$ (a,b), $U^* = 4$ (c,d), $U^* = 5$ (e,f), $U^* = 6$ (g,h) and $U^* = 7$ (i,j).

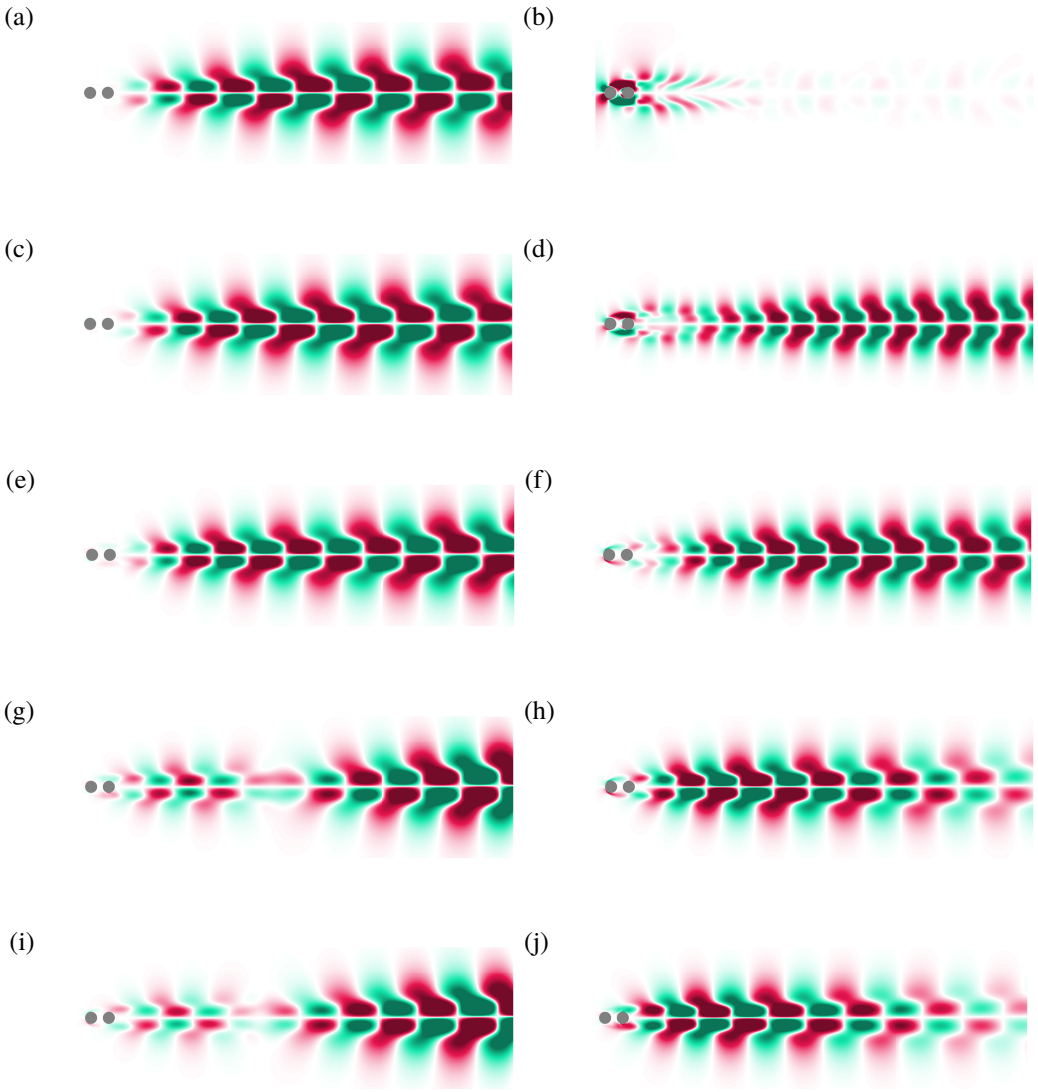

Figure 4.10: Flow past two spring-mounted circular cylinders in tandem arrangement at $Re = 100$. Spatial distribution of the horizontal velocity component of the real part of mode 1 (a,c,e,g,i) and mode 2 (b,d,f,h,j) for $U^* = 3$ (a,b), $U^* = 4$ (c,d), $U^* = 5$ (e,f), $U^* = 6$ (g,h) and $U^* = 7$ (i,j).

References

Borazjani, Iman and Fotis Sotiropoulos (2009). "Vortex-induced vibrations of two cylinders in tandem arrangement in the proximity–wake interference region". In: *Journal of Fluid Mechanics* 621, pp. 321–364. DOI: 10.1017/S0022112008004850.

Citro, V. et al. (2017). "Efficient stabilization and acceleration of numerical simulation of fluid flows by residual recombination". In: *Journal of Computational Physics* 344, pp. 234–246. ISSN: 0021-9991. DOI: https://doi.org/10.1016/j.jcp.2017.04.081.

Griffith, Martin D. et al. (2017). "Flow-induced vibration of two cylinders in tandem and staggered arrangements". In: *Journal of Fluid Mechanics* 833, pp. 98–130. DOI: 10.1017/jfm.2017.673.

Papaioannou, Georgios V. et al. (2006). "Three-dimensionality effects in flow around two tandem cylinders". In: *Journal of Fluid Mechanics* 558, pp. 387–413. DOI: 10.1017/S0022112006000139.

Prasanth, T. and Sanjay Mittal (May 2009). "Vortex-induced vibration of two circular cylinders at low Reynolds number". In: *Journal of Fluids and Structures* 25, pp. 731–741. DOI: 10.1016/j.jfluidstructs.2008.12.002.

Singh, Satya and Sanjay Mittal (Nov. 2005). "Vortex-induced oscillations at low Reynolds numbers: Hysteresis and vortex-shedding modes". In: *Journal of Fluids and Structures* 20, pp. 1085–1104. DOI: 10.1016/j.jfluidstructs.2005.05.011.

Chapter 5

LINEAR STABILITY OF A GAS BUBBLE IN A STRAINING FLOW

The shortest path between two truths in the real domain passes through the complex domain.

Jacques Hadamard

In this chapter, the problem of the behavior of a gas bubble immersed in an axisymmetric straining flow is investigated. The dynamics is explored by means of a linear stability analysis of the steady solutions of the system conducted within a linearized Arbitrary Lagrangian Eulerian framework.

The maximum Weber number We_c is determined, beyond which no steady state is possible. Besides, by means of a pseudo-arc-length continuation method, an unstable branch of solutions is identified and a saddle-node bifurcation is detected. Edge states along this unstable branch constitute routes to the bubble breakup through an end-pinching mechanism. A new unstable non-oscillating mode is discovered, never identified before. The mode behaves in a counterintuitive way, as it corresponds to a drift of the bubble in the direction perpendicular to the axial strain, where the flow exerts compressive forces on the bubble. This surprising dynamics is made possible by a self-propulsion mechanism that exploits the asymmetric deformation of the bubble.

5.1 Introduction

The formation of bubbles and droplets is part of our daily life, from geophysical flows to the fizz of a Champagne bottle, or kids blowing soap bubbles. From a technical point of view, the use of air bubbles is a promising approach for various Lab on Chip applications, while it is already recognized as effective in drug-reduction applications. As a result of its universality, this phenomenon has long attracted the interest of researchers since the early studies of Leonardo, who first noticed the spiraling or zigzag paths of ascending bubbles (Herrada and Eggers, 2023).

The dynamics of a gas bubble suspended in a uniaxial straining flow is considered here. This problem has received great attention since the pioneering experiments

of Taylor (1934), who placed a liquid drop in a straining flow generated by counter-rotating rollers. Differently from the cases investigated in the previous chapters, the dynamics of bubbles and droplets is characterized by the presence of an interface delimiting two different fluid phases, rather than a solid-fluid one. The dynamics of the interface is predicted by the interplay of capillary, pressure, and viscous forces. When the action of viscous forces overcomes the restoring effect of capillary forces, the bubble cannot undergo further elongation and breaks up. This phenomenon is typically described in terms of two non-dimensional parameters that can be selected out of three possibilities, namely the Reynolds number Re, the Weber number We , defined as the ratio of inertial forces to capillary forces, and the Ohnesorge number Oh , which compares the magnitudes of viscous and capillary forces. Many researchers have conjectured the existence of a critical Weber number We_c beyond which no steady bubble shape can exist. The first contribution to this theory was made by Acrivos and Lo (1978), who showed that for low-Reynolds number flows the critical Weber goes as $We_c \propto Re^{3/4}$. Later, steady-state solutions for the finite deformation of a bubble in a uniaxial straining flow were found numerically by Miksis (1981), who considered the bubble breakup in the inviscid limit and determined We_c for the convergence of steady solutions. Subsequently, Ryskin and Leal (1984) numerically identified steady bubble shapes for non-zero viscosity cases over a wide range of We_c and for a set of finite Re, by solving the complete Navier-Stokes equations on a body-fitted grid. For each Reynolds number, steady solutions could only be found for $We < We_c$, with We_c increasing monotonically with Re. The results matched reasonably well with the predictions of Acrivos and Lo, 1978 and Miksis, 1981 in the respective limits. The critical values predicted by Ryskin and Leal (1984) were later confirmed by Kang and Leal (1987), who considered the unsteady bubble deformation in uniaxial straining both at finite Re and under the potential assumption. They showed that the bubble becomes infinitely elongated for $We > We_c$, and that the critical Weber is highly sensitive to the initial shape of the bubble. In addition, the unsteady analysis of oscillating bubbles revealed that the oscillation frequency decreases with We.

In this work, this phenomenon is investigated with the help of a global linear stability approach. The difficulties arising because of the unknown shape and location of the interface are addressed here by making use of a recently developed ALE formalism (Bonnefis, 2019), which enables the coupling between the fluid and the interface in a consistent manner. Here it is considered an incompressible gas bubble with volume V_b placed in a uniaxial straining flow. The dimensional velocity field far

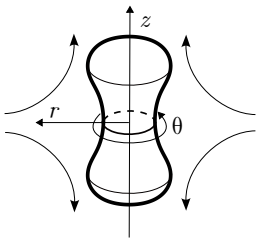

Figure 5.1: Sketch of the physical configuration with the symmetry axis $r = 0$ and the symmetry plane $z = 0$ of the undisturbed straining flow, and the corresponding $(\boldsymbol{e}_r, \boldsymbol{e}_\theta, \boldsymbol{e}_z)$ basis.

from the interface, outlined in Figure 5.1 is the hyperbolic steady flow given by

$$\boldsymbol{U}_\infty = -\frac{S}{2} r \boldsymbol{e}_r + S z \boldsymbol{e}_z, \tag{5.1}$$

where S denotes the uniform strain rate, and $(\boldsymbol{e}_r, \boldsymbol{e}_\theta, \boldsymbol{e}_z)$ is the coordinate basis. The density and viscosity of the lighter fluid inside the bubble are considered to be negligible with respect to the external fluid, whose density ρ and dynamic viscosity λ are assumed to be constant . The effects of gravity are neglected and the surface tension γ is considered to be uniform throughout the interface. The bubble is initially placed with its centroid at the origin of the coordinate system ($z = 0$). The dynamics is governed by the following set of equations

$$\partial_t \boldsymbol{v} + \boldsymbol{v} \cdot \nabla \boldsymbol{v} = \rho^{-1} \nabla \cdot \boldsymbol{\Sigma} \quad \text{in } \Omega(t)\,, \tag{5.2}$$

$$\nabla \cdot \boldsymbol{v} = 0 \quad \text{in } \Omega(t)\,, \tag{5.3}$$

$$\partial_t \eta = \boldsymbol{v} \cdot \boldsymbol{n} \quad \text{on } \Gamma_b(t)\,, \tag{5.4}$$

$$\boldsymbol{\Sigma} \cdot \boldsymbol{n} = (-p_b + \gamma\kappa)\boldsymbol{n} \quad \text{on } \Gamma_b(t)\,, \tag{5.5}$$

In the above-described system, $\Omega(t)$ and $\Gamma_b(t)$ denote the fluid domain and bubble-fluid interface, respectively, η is the normal displacement of the interface, $\boldsymbol{n}$ is the local unit normal vector directed into the fluid and κ is the curvature at the surface. Equation 5.2 and 5.3 are the dimensional Navier-Stokes and continuity equations, respectively, where $\boldsymbol{v}$ is the flow velocity and $\boldsymbol{\Sigma} = -p\boldsymbol{I} + \lambda\left(\nabla \boldsymbol{v} + \nabla^\intercal \boldsymbol{v}\right)$ is the stress tensor. Equation 5.4 gives the kinematic boundary condition, imposing the coincidence of normal velocities at the interface, while Equation 5.5 imposes the dynamic boundary condition, expressing the equilibrium of stresses at the interface. Specifically, the jump in normal stress across the interface is proportional to its curvature, and p_b is the pressure inside the bubble. The system must be closed by appropriate boundary conditions at $r = 0$, $z = 0$, and in the far field.

Compared to the FSI problems investigated in the previous chapters, fluid-fluid problems differ in the way they impose the boundary conditions as slipping is allowed at the interface in absence of surfactants. Hence, tangential stresses cancel out at the interface and the free-shear condition $\boldsymbol{t}\cot(\boldsymbol{\Sigma}\cdot\boldsymbol{n})$ closes the system.

5.2 Steady solutions and bifurcation diagram

The symmetry of the boundary conditions is reflected in the base flow, which is axisymmetric with respect to the z-axis ($r = 0$) and shows a mirror symmetry with respect to the midplane $z = 0$ Figure 5.1. In addition to the boundary conditions given above, the bubble equilibrium shape must ensure that its volume remains constant and equal to $V_b = \frac{\pi}{6}d^3$, where d is the equilibrium diameter.

The first objective of this work is to track the equilibrium solutions in the state space (Oh, We), where the Ohnesorge $Oh = \dfrac{\mu}{\sqrt{\rho\gamma d}}$ corresponds to a capillary number $Ca = \dfrac{U_c\mu}{\gamma}$ based on the capillary velocity scale $U_c = (\gamma/(\rho d))^{1/2}$, and the Weber number is defined as $We = \dfrac{\rho S^2 d^3}{4\gamma}$. In section 5.1 it was stated that only two out of three non-dimensional parameters are needed to characterize the dynamics of the system. This is indeed true as an appropriate definition of the Reynolds number may be obtained by combining the other two parameters as $Re = \dfrac{\sqrt{We}}{Oh} = \dfrac{\rho U_c d}{\mu}$. Given the symmetry of the equilibrium solution, the deformed bubble shape may be described through the aspect ratio $\chi = d_z/d_r$, with d_z and d_r the major and minor axis lengths, respectively.

The difficulties arising due to the dependence of the flow domain over time are handled through the adoption of a Linearized Arbitrary Lagrangian Eulerian formalism (L-ALE), which allows to rewrite the fluid equations in a fixed reference domain and accounts for the deformation of the actual domain introducing an extension by introducing an extension displacement field $\boldsymbol{\xi}$ that propagates the deformation of the interface into the fluid domain. It is arbitrary as it only needs to respect the no-penetration condition and ensure a smooth propagation of the interface displacement. The L-ALE method employed for this investigation, developed by Bonnefis (2019), is especially suited for the class of problems involving free surfaces. Figure 5.2 illustrates the basic principle of the L-ALE methodology. The sketch shows how the interface Γ_b in the physical domain Ω is linked to the reference configuration Γ_b. The quantities of interest are evaluated in the reference domain, then they are mapped onto the physical domain. The flow equations and the deformation

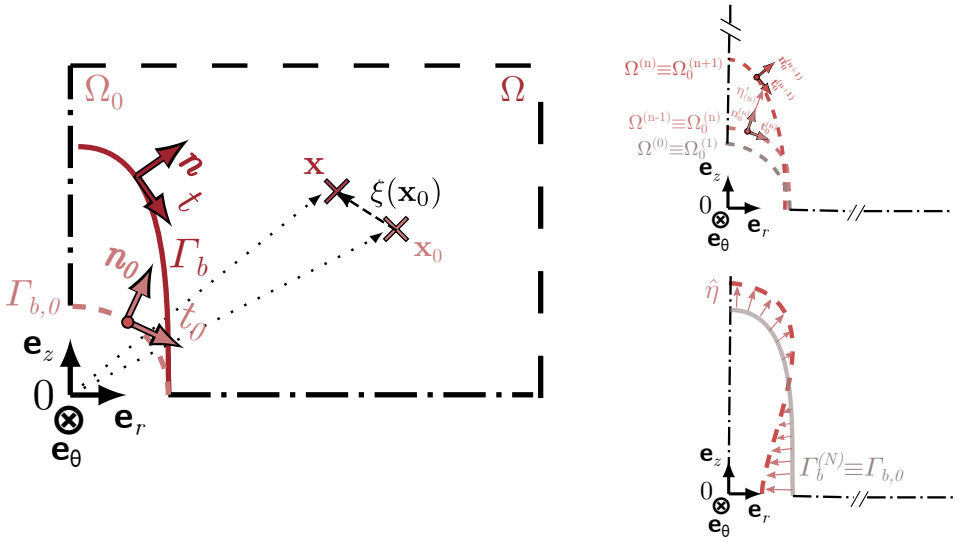

Figure 5.2: Sketch of the L-ALE approach. (a): the general framework, showing the *physical* domain Ω and the *reference* domain Ω_0 (the bubble surface in these two domains is Γ_b and $\Gamma_{b,0}$, respectively); (b): successive updates of the reference domain during the iterations of the Newton method; (c): reference domain for the linear stability problem.

of the interface are solved simultaneously, yielding a monolithic approach, which ensures the stability of the calculations. In order to determine equilibrium solutions with varying (Re, We), it is used a continuation method based on a Newton algorithm. Specifically, a pseudo-arch-length is implemented, which consists in adding an additional column and row to the Jacobian matrix of the system, *i.e.* adding an unknown in the Newton iteration. In this case, the state vector is augmented with the update of the strain rate. The solver utilizes the finite-element software FreeFem++ (Hecht, 2012) to assemble all the matrices resulting from the variational formulation of the equations. The arch-length continuation is performed via the Matlab drivers of the StabFem project (StabFem). As the bubble shape deforms in the continuation process, the starting mesh can become too distorted, thus a re-meshing step may be required at some point.

Figure 5.3b shows the variation of We_c with the Reynolds number. For low Reynolds numbers, the critical Weber grows almost linearly with Re. The result is in good agreement with the predictions of Acrivos and Lo (1978) for the creeping flow. For larger values of Re, the critical Weber tends to the inviscid limit, as expected. The present results confirm those of Ryskin and Leal (1984) (solid black line). It may be observed that the stationary bubble shape corresponding to critical

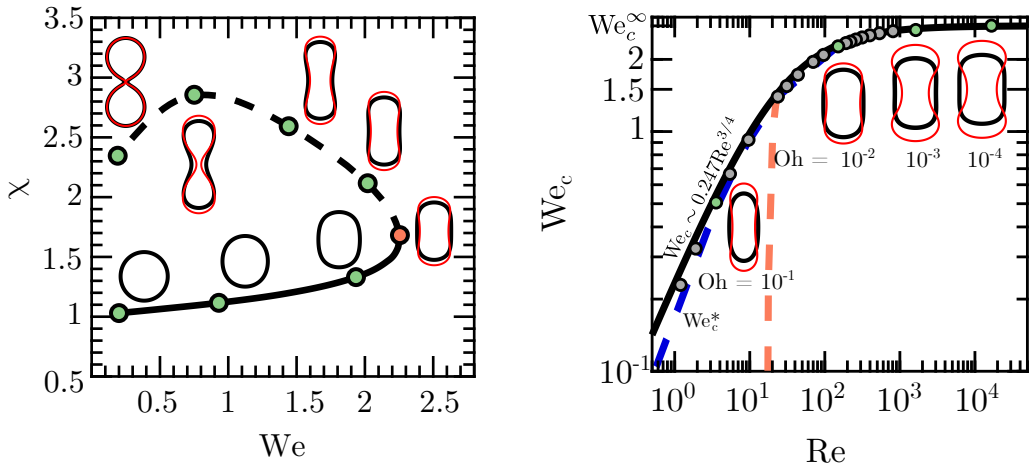

Figure 5.3: (a): variation of the bubble elongation with the Weber number for a fixed value of the Ohnesorge number, here $Oh = 10^{-2}$; (b): variation of the critical Weber number with the Reynolds number. Grey, green, and red circles: present results obtained with the L-ALE approach (the red bullet corresponds to the critical Weber number where the saddle-node bifurcation takes place); thick solid black line: empirical correlation proposed in (Ryskin and Leal, 1984). In (b), the red dashed line is the limit beyond which the Mode 1-S (s) is unstable; the blue dashed line is the maximum Weber number $We = We_c^*(Re)$ beyond which the bubble stops oscillating. In both panels, bubble shapes are shown for selected values of the parameters corresponding to the green bullets; the black and red contours correspond to the steady state and the unstable Mode 0-S (s), respectively.

conditions is convex for intermediate and large Ohnesorge numbers, but becomes slightly concave in the neighborhood of the symmetry plane at lower Oh. Here We_c indicates the maximum Weber number for which convergence of the steady state could be obtained. The corresponding bubble shapes are reported on the figure, for the Reynolds numbers indicated by the green circles in the graph, with black contours. The corresponding value of the Ohnesorge number is reported under each shape.

A bifurcation diagram for the Ohnesorge value $Oh = 0.01$ is reported in Figure 5.3a. It is identified a saddle-node bifurcation at a critical Weber number $\mathrm{We}_c \approx 2.27$ beyond which no stationary solution exists. The bifurcation connects a stable and an unstable branch. As shown in the graph, the stable branch (indicated by a solid black line) corresponds to the previously computed steady states. Previous studies (Kang and Leal, 1987) showed that the bubble extends indefinitely for $We > We_c$, and eventually breaks up. The unstable branch, which was reported before under

the creeping-flow assumption (Gallino, Schneider, and Gallaire, 2018), is associated with the breakup of the bubble under subcritical conditions. Within the creping-flow limit, Gallino, Schneider, and Gallaire (2018) indicated this branch as the orbit of *edge states*, *i.e.* unstable equilibria that behave as attractors if the initial condition lies in their basin of attraction. Practically speaking, the edge states "guide" the bubble to break up in a sub-critical flow, selecting a precise mechanism for the rupture. Physically, this mechanism corresponds to the emergence of a neck in the symmetry plane. Edge states for lower Weber numbers have not been calculated since their computation becomes tricky due to the high concavity of the bubble neck. Figure 5.4a shows the result of the continuation procedure for different values of the Ohnesorge number. The solid line is used to represent the stable branch, while the dashed line indicates the edge states. In red is reported the value of Oh for each curve. For larger values of the Ohnesorge number, the critical Weber number is seen to decrease rapidly with Oh, as reported also in Figure 5.4b.

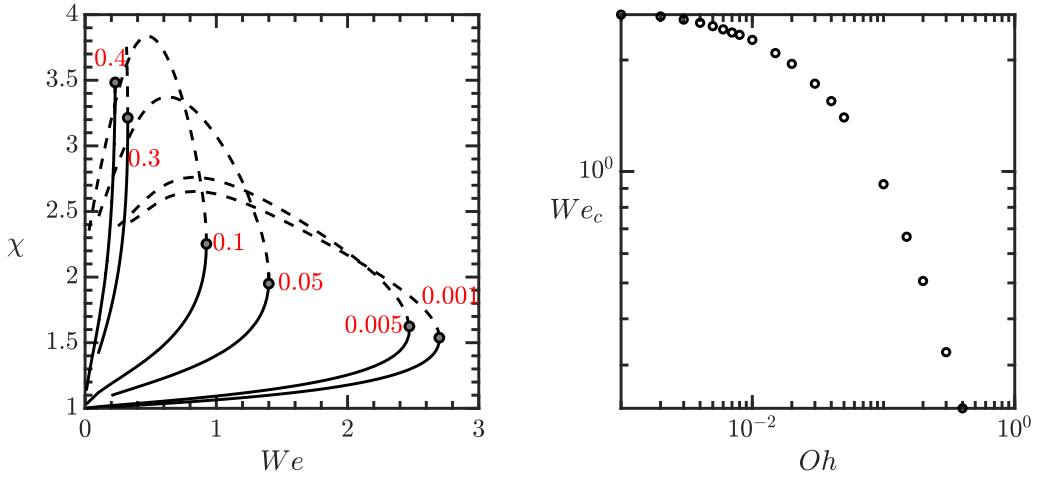

Figure 5.4: Bubble aspect ratio χ versus the Weber number We, for different values of Oh. The critical Weber number We_c for each curve is represented with a grey circle, while the value of Oh is reported in red. (b): Variation of the critical Weber number We_c with the Ohnesorge number Oh.

One intriguing result to notice is that, for the Ohnesorge number selected in Figure 5.3a, this concavity does not emerge at the critical We, but appears at some point on the unstable branch. It coincides with the saddle-node only in the high-Reynolds limit.

5.3 Linear Stability

The stability of steady states is investigated by means of a modal LSA analysis that looks at the evolution of perturbations with a specific form. Namely, in this work are considered perturbations of the form $\Psi(r,z)e^{im\theta-i\omega t}$, where θ is the polar angle of the cylindrical coordinate system sketched in Fig. 5.1, m is the polar wavenumber and ω is the complex eigenvalue. Eigenmodes of the kind defined above can be classified depending on the value of m and their symmetry characteristics. The nomenclature employed here to designate the linear modes makes use of the polar wavenumber and two letters, the first one indicating the symmetry type (symmetric S or antisymmetric A) with respect to $z = 0$, and the second one indicating the oscillatory (o) or steady (s) nature of the mode. It is worth recalling that within this framework, the frequency of the mode is given by the real part of the eigenvalue ω, and the growth rate corresponds to the imaginary part, in contrast with the convention adopted in the previous chapters. The steady solutions on the lower branch of the bifurcation diagram of Figure 5.3a are found to be linearly stable as any small disturbance to their shape dies out owing to the effect of viscosity and surface tension. The edge states, by contrast, are linearly unstable due to the existence of an amplified eigenmode of the 0-S(s) type.

Symmetry-preserving modes

The eigenmodes considered here belong to the class 0-S, as they are symmetric with respect to $z = 0$. This characteristic is common to many experimental studies, where the bubble centroid is kept fixed at the stagnation point through computer-controlled devices (Bentley and Leal, 1986b; Bentley and Leal, 1986a). Under such circumstances, two leading eigenmodes are found. One is the previously mentioned unstable breakup mode 0-S (s), found along the upper branch of the bifurcation diagram. This mode is stationary ($\Re(\omega) = 0$) and emerges at the critical Weber We_c. The second mode, instead, has an oscillatory nature (0-S (o)) and it is stable. In Figure 5.6(a) it is shown how the frequency of this mode (black line) decreases with We and becomes eventually zero for $We = We_c^*$, as the complex eigenmode splits into two real stable modes. Then, one of these modes increases as We_c grows towards We_c^* (red one), and the other one decrease (green one). The damping rate of the eigenvalue with the smallest module (red line) vanishes eventually for $We_c = We_c^*$, leading to the emergence of the amplified mode 0-S (s) beyond the saddle-node point, which corresponds to infinite elongation breakup. The damping rate of the original mode 0-S (o) (green line), instead, increases continuously from

We_c^* to We_c.

Figure 5.6 reports the eigenfunctions corresponding to modes 0-S (o) and 0-S (s) at a slightly subcritical Weber number. Owing to the competition of inertial and capillary effects, the bubble undergoes a periodic compression and elongation in the z-direction under mode 0-S (o).

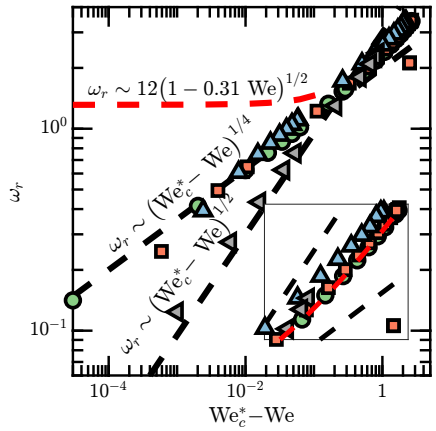

Figure 5.5: Variation of the oscillation frequency ω_r of Mode 0-S (o) with We. The black dashed lines correspond to the asymptotic scalings suggested by the present result. The red line shows the low-We expansion of (Kang and Leal, 1988). The green circles, red squares, blue triangles, and grey triangles refer to $Oh = 10^{-4}, 10^{-3}, 10^{-2}$ and 10^{-1}, respectively.

Figure 5.7(a), instead, reports the variation of the growth rate of mode 0-S (s) with respect to $(We_c - We)$. In the high and low Reynolds number limit, the growth rate goes as $(We_c - We)^\alpha$, with $\alpha = 1/4$ and $\alpha = 1/2$, respectively. The same coefficients hold for the frequency of mode 0-S (o), which varies as $(We_c^* - We)^\alpha$. The similarity of the scalings suggests a close connection between the dynamics of the two modes. As can be seen from Figure 5.6(a), We_c^* is slightly smaller than We_c when viscous effects are predominant (higher Oh values), and it coincides with We_c when they are negligible ($Oh \to 0$). These results are consistent with those of Kang and Leal (1987). The aperiodically damped oscillations of mode 0-S (o) were also noticed by Kang and Leal (1988), who predicted the emergence of this behavior for $Oh \gtrsim 0.12$.

The inset in Figure 5.8 shows a close up of the change in ω_r with $(We_c^* - We)$ for $(We_c^* - We) \gtrsim 0.3$. The red dashed line reports the predicted behavior of ω_r based on an expansion around $We = 0$. This prediction is shown to hold in the inset region, but it fails to predict the rapid variations of the frequency near the critical Weber number.

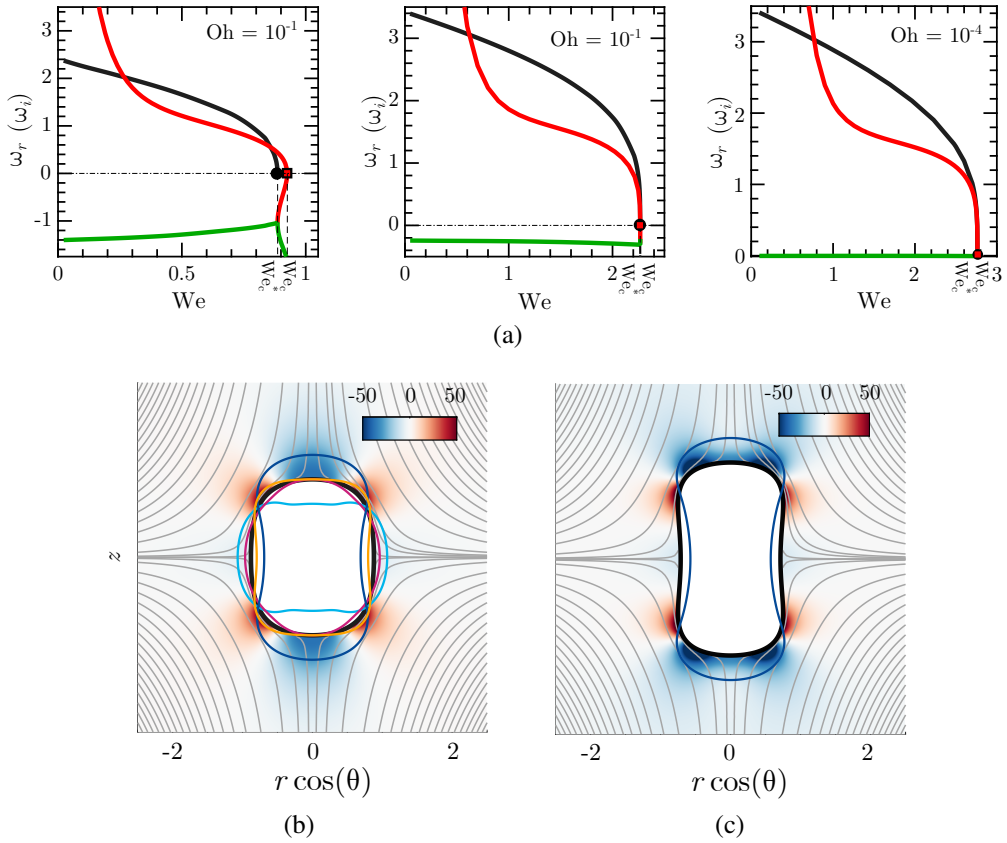

Figure 5.6: (a): Variation of the frequency (solid lines) and growth rate (dashed lines) of Mode 0-S (o) (with thick and thin black lines for $\mathrm{We} \leq \mathrm{We}_c^*$ and $\mathrm{We} > \mathrm{We}_c^*$, respectively) and Mode 0-S (s) (red lines) with respect to We, for three values of the Ohnesorge number. The black circle and red square indicate the critical values We_c^* and We_c, respectively. $(b) - (c)$: Pressure disturbance (colors) and bubble shape (thick contours) for Mode 0-S (o) in (b) and Mode 0-S (s) in (c), both at $\mathrm{We} = 2.5$ and $\mathrm{Oh} = 1 \times 10^{-4}$. The black contour and thin grey lines respectively represent the bubble shape and the streamlines in the base state, which stands on the lower branch of the bifurcation diagram in (b) ($\omega = -0.0044 + 1.3284\mathrm{i}$) and on the upper branch in (c) ($\omega = +0.2797$). In (b), the colors show the imaginary part of the pressure disturbance at time $t = T/4$ and the bubble shape is displayed at $t = T/4$ (light blue solid line), $t = T/2$ (light blue dashed line), $t = 3T/4$ (dark blue solid line), and $t = T$ (dark blue dashed line), with T the period of oscillation.

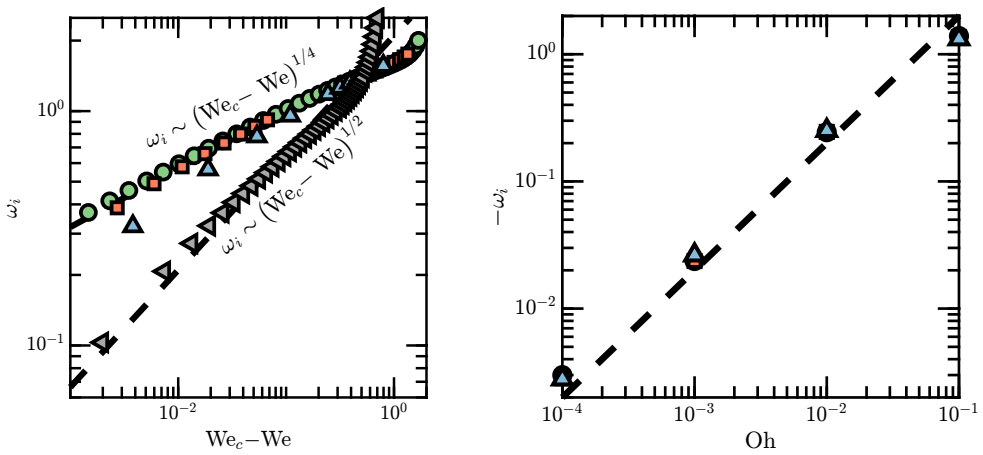

Figure 5.7: Variations of the growth rate of modes 0-S (o) and 0-S (s). (a): with respect to $\mathrm{We}_c - \mathrm{We}$ for Mode 0-S (s) on the unstable branch; (b): with respect to Oh for Mode 0-S (o) on the stable branch. In (a), the green bullets, red squares, blue triangles, and grey triangles refer to Oh = $10^{-4}, 10^{-3}, 10^{-2}$ and 10^{-1}, respectively; in (b), the green circles, red squares, and blue triangles refer to We = $0.1, 0.2$ and 0.4, respectively. The dashed lines indicate the asymptotic scalings.

In Figure 5.7(b), the decay rate of mode 0-S (o) is reported as a function of Oh. The mode is always stable and the growth rate decreases linearly with Oh, with apparently no dependence on We. In the inviscid limit ($Oh \to 0$), the mode becomes neutrally stable. This result is consistent with the observation that two purely complex eigenvalues become two real ones (see Figure 5.6(a)). The oscillating mode 0-S (o), therefore, cannot lead to the bubble breakup since viscous damping and capillary tension act as stabilizers, at least for non-zero viscosity values. It is clear that the symmetry-preserving mode leading to rupture is the stationary mode 0-S (s) linked to the infinite elongation of the bubble. For instance, when the initial bubble shape is characterized by a high aspect ratio, the capillarity force in the neck region fails to balance the higher pressure acting in the mid-plane. Beyond the linear stage considered here, this situation leads unavoidably to break up through the classic end-pinching scenario (Stone, Bentley, and Leal, 1986; Stone and Leal, 1989).

Symmetry-breaking unstable modes

Here they are considered eigenmodes of the type 0-A, *i.e.* modes showing an asymmetry with the midplane.

These modes can arise when the bubble is not forced to remain centered in the stagnation point. Two new unstable modes are identified in this way. One of them,

denoted as mode 0-A (s), is unstable for every (We, Re) couple and shows an asymmetry with respect to the plane $z = 0$. The mode, reported in Figure 5.9(b), tends to move the bubble away from the hyperbolic point of the base flow. The escaping mechanism of the bubble can be easily explained: an initial perturbation breaks the symmetry of the base state as the bubble centroid is displaced along the z axis. As a consequence of this movement, the bubble drifts away with the flow as the fore-aft symmetry of the pressure distribution is broken.

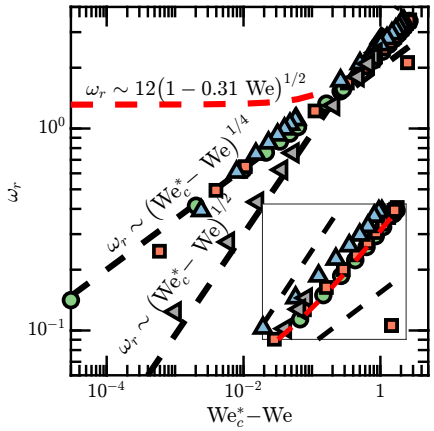

Figure 5.8: Variation of the oscillation frequency ω_r of Mode 0-S (o) with We. The black dashed lines correspond to the asymptotic scalings suggested by the present results. The red line shows the low-We expansion of (Kang and Leal, 1988). The green bullets, red squares, blue triangles, and grey triangles refer to Oh = $10^{-4}, 10^{-3}, 10^{-2}$ and 10^{-1}, respectively.

The second unstable mode, denoted as mode 1-S (s), is also a stationary mode, but it is antisymmetric with respect to the $r = 0$ plane and associated with a $m = 1$ polar number. In this case, the bubble still drifts away, but this time it is not carried by the straining flow, instead, its movement opposed the direction of the baseflow. This result is quite surprising since it is counterintuitive that the bubble can move towards higher-pressure regions.

The explanation for this self-propulsion lies in the asymmetric deformation of the surface. Indeed, a massless deformable moby immersed in a potential flow can self-propel by experiencing a net rate of deformation (Saffman, 1967) and (Miloh and Galper, 1993). Of course, since the mode involved in the present case is stationary, this self-propulsion lasts only as long as this mode grows, and it necessarily stops due to the nonlinear saturation. This hypothesis is confirmed by investigating analytically the leading-order perturbation of the solution obtained with the potential assumption, following the approach of Kang and Leal (1988) and Yang, Feng, and Leal (1993).

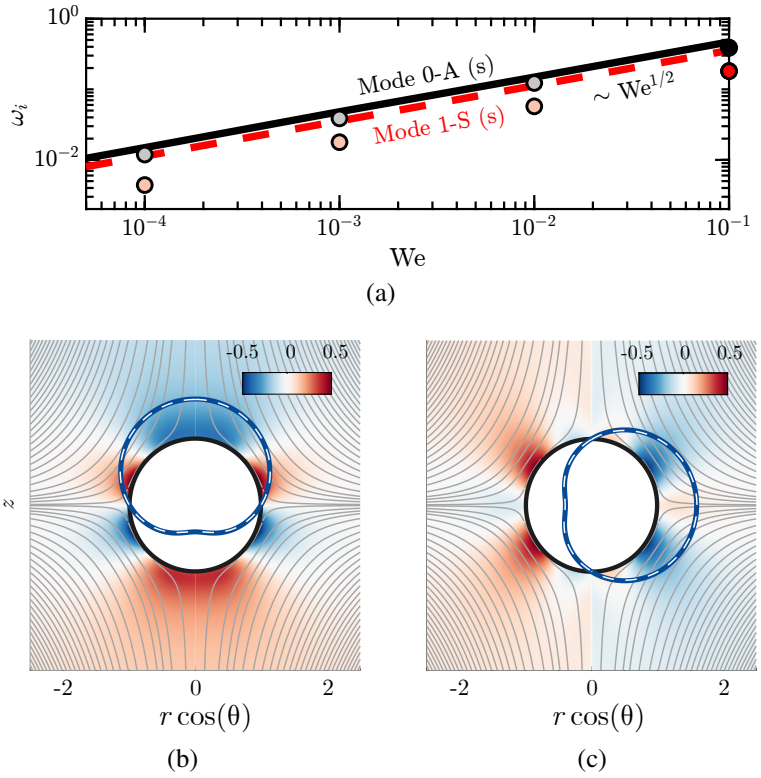

Figure 5.9: Modes 0-A (s) and 1-S (s) in a high-Reynolds-number case. (a): variation of the growth rate of the two modes with respect to We, computed through the truncated inviscid potential solution (lines), and the L-ALE approach in a slightly viscous flow with Re=10^3 (bullets); black/grey: Mode 0-A (s), red/pink: Mode 1-S (s). (b): pressure disturbance (colors) and bubble shape (contours) for Mode 0-A (s) with $We = 10^{-1}$ and $Re = 10^3$ (corresponding to the black bullet in (a)). The blue solid and pink dashed lines refer to the results provided by the L-ALE approach and the truncated potential flow expansion, respectively. (c): same with Mode 1-S (s) (corresponding to the red bullet in (a)). In $(b)-(c)$, the black contour represents the bubble shape in the base state and the thin grey lines show the corresponding streamlines.

Specifically, assuming $\boldsymbol{v} = \nabla\phi$, solutions are sought in the form of harmonic functions satisfying

$$\partial_t\eta = \nabla\phi\cdot\boldsymbol{n}\,, \quad \partial_t\phi + \frac{1}{2}(\nabla\phi\cdot\nabla\phi) + \rho^{-1}p_b = \rho^{-1}\gamma\nabla\cdot\boldsymbol{n} \quad \text{on } \Gamma_b\,. \tag{5.6}$$

Expanding the velocity potential ϕ and the surface η of the bubble in the form

$$\begin{aligned} \phi &= \tfrac{Sd^2}{4}(\phi_s + \varepsilon\phi_u^m)\,, & \eta &= \tfrac{d}{2}(\eta_s + \varepsilon\eta_u^m)\,, \\ \phi_s &= P_2^0(\zeta)(\tfrac{1}{2}r_s^2 + \tfrac{1}{3}r_s^{-3})\,, & \eta_s &= 1\,, \\ \phi_u^m &= \textstyle\sum_{n=0}^{\infty}\chi_n^m(t)r_s^{-(n+1)}Y_n^m(\Theta,\varphi)\,, & \eta_u^m &= \textstyle\sum_{n=1}^{\infty}\delta_n^m(t)Y_n^m(\Theta,\varphi)\,, \end{aligned} \tag{5.7}$$

with $Y_n^m(\Theta, \varphi) = P_n(\zeta)e^{-im\varphi}$ the spherical harmonics, P_n the associated Legendre polynomial and $\zeta = \cos\Theta$. The spherical coordinate system is such that $\Theta = 0(\pi)$ on the positive (negative) semi-axis in the z direction (see Figure 5.1). Here the meridional angle ϕ is equivalent to θ, r_s denotes the non-dimensional radial position in the spherical coordinate system. Injecting the ansatz (5.7) into Equation 5.6, with $\varepsilon \ll 1$ and keeping only terms of $O(\varepsilon)$ yields an eigenvalue problem. The solution of this EVP for $m = 0$ and $m = 1$ reveals the existence of two leading modes, 0-A (s) and 1-S (s). Their growth rate is reported in Figure 5.9(a) as a function of We. The circles in the figure represent the growth rates of the corresponding modes obtained with the L-ALE approach. As can be observed, the values obtained with the L-ALE framework are slightly lower, this is due to the fact that the potential flow assumption does not take into account stabilizing viscous effects. Although these effects are expected to be weak for $Re = 10^3$, they are nonetheless to be stabilizing. Despite these limitations, the truncated potential flow solution is found to provide a reliable estimate of the bubble deformation for modes 0-A (s) and 1-S (s) (dashed line in Figure 5.9$(b) - (c)$). This perturbative approach confirms that the unexpected presence of the unstable mode 1-S (s) is indeed physically admissible and it is not a numerical artifact of the L-ALE approach. One last thing to point out is that the growth rate of mode 1-S (s) is slightly smaller than the one of mode 0-A (s). Consequently, to observe the former in a laboratory experiment, it is necessary to constrain the bubble displacement to prevent it from moving along the z-axis.

References

Acrivos, A. and T. S. Lo (1978). "Deformation and breakup of a single slender drop in an extensional flow". In: *J. Fluid Mech.* 86.4, pp. 641–672.

Bentley, B. J. and L. G. Leal (1986a). "A computer-controlled four-roll mill for investigations of particle and drop dynamics in two-dimensional linear shear flows". In: *J. Fluid Mech.* 167, pp. 219–240.

– (1986b). "An experimental investigation of drop deformation and breakup in steady, two-dimensional linear flows". In: *J. Fluid Mech.* 167, pp. 241–283.

Bonnefis, P. (2019). "Etude des instabilités de sillage, de forme et de trajectoire de bulles par une approche de stabilité linéaire globale". PhD thesis. Toulouse, France (available online at http://www.theses.fr/2019INPT0070): Inst. Nat. Polytech. Toulouse.

Gallino, G., T. M. Schneider, and F. Gallaire (2018). "Edge states control droplet breakup in subcritical extensional flows". In: *Phys. Rev. Fluids* 3.7, p. 073603.

Hecht, Frédéric (Dec. 2012). "New development in FreeFem++". In: *Journal of Numerical Mathematics* 20. DOI: 10.1515/jnum-2012-0013.

Herrada, Miguel A. and Jens G. Eggers (2023). "Path instability of an air bubble rising in water". In: *Proceedings of the National Academy of Sciences* 120.4, e2216830120. DOI: 10.1073/pnas.2216830120.

Kang, I. S. and L. G. Leal (1987). "Numerical solution of axisymmetric, unsteady free-boundary problems at finite Reynolds number. I. Finite-difference scheme and its application to the deformation of a bubble in a uniaxial straining flow". In: *Phys. Fluids* 30.7, pp. 1929–1940.

– (1988). "Small-amplitude perturbations of shape for a nearly spherical bubble in an inviscid straining flow (steady shapes and oscillatory motion)". In: *J. Fluid Mech.* 187, pp. 231–266.

Miksis, M. J. (1981). "A bubble in an axially symmetric shear flow". In: *Phys. Fluids* 24.7, pp. 1229–1231.

Miloh, T. and A. Galper (1993). "Self-propulsion of general deformable shapes in a perfect fluid". In: *Proc. R. Soc. London Ser. A-Math. Phys. Eng. Sci.* 442.1915, pp. 273–299.

Ryskin, G. and L. G. Leal (1984). "Numerical solution of free-boundary problems in fluid mechanics. Part 3. Bubble deformation in an axisymmetric straining flow". In: *J. Fluid Mech.* 148, pp. 37–43.

Saffman, P. G. (1967). "The self-propulsion of a deformable body in a perfect fluid". In: *J. Fluid Mech.* 28.2, pp. 385–389.

Stone, H. A., B. J. Bentley, and L. G. Leal (1986). "An experimental study of transient effects in the breakup of viscous drops". In: *J. Fluid Mech.* 173, pp. 131–158.

Stone, H. A. and L. G. Leal (1989). “Relaxation and breakup of an initially extended drop in an otherwise quiescent fluid”. In: *J. Fluid Mech.* 198, pp. 399–427.

Taylor, G. I. (1934). “The formation of emulsions in definable fields of flow”. In: *Proc. R. Soc. London Ser. A-Math. Phys. Eng. Sci.* 146, pp. 501–523.

Yang, S. M., Z. C. Feng, and L. G. Leal (1993). “Nonlinear effects in the dynamics of shape and volume oscillations for a gas bubble in an external flow”. In: *J. Fluid Mech.* 247, pp. 417–454.

Chapter 6

CONCLUDING REMARKS AND PERSPECTIVES

This thesis represents a contribution towards the analysis of complex fluid-structure interaction problems from a linear perspective. The role played by linear effects in the loss of stability of a fluid-structure system has motivated researchers to develop new techniques to perform linear stability analyses of coupled FSI problems. The main contribution of this work is the introduction of a matrix-free procedure that extends time-stepping approaches to the analysis of fully coupled flow-structure systems. To the author's knowledge, in the context of FSI systems, the global linear approach has not been extended to problems involving multiple elastic bodies up to now. The numerical linearization proposed in this thesis accounts for the fully coupled solid and fluid dynamics and thus is able to identify all the instability mechanisms arising in the system. The proposed time-stepping IB approach, indeed, is able to extract stability information from simulations irrespective of the total number of immersed bodies or the complexity of the multi-physics phenomenon under investigation.

In the first chapter, an introduction to FSI problems was given, together with a short preamble to the broad subject of fluid-structure instability. In the second chapter, after a brief literature review on the most common numerical methods employed for the solution of FSI problems, the IB computational framework utilized throughout the manuscript is presented. A direct-forcing IB method is adopted to simulate fully coupled nonlinear FSI problems, based on an MLS procedure to impose the boundary conditions at the interface. The principal advantage offered by the method is its versatility and efficiency in handling complex geometries of arbitrary thickness. Some details are given about the tricky task of hydrodynamic load evaluation with partitioned algorithms.

In the third chapter, a simple and robust approach to perform linear stability analyses of FSI configurations was presented. A time-stepping iterative procedure, based on the exponential transformation of the Jacobian matrix, was derived in a general setting. This was implemented within the IB framework described in the second chapter and validated against well-documented cases of flow-induced vibrations of rigid bodies. The outcomes of the linear stability analysis showed a good overall agreement with the results from the literature, obtained using mesh-conforming

methods.

In the fourth chapter, the methodology was applied to study the VIV of two cylinders in tandem; the results of the stability analysis matched reasonably well with the nonlinear simulations, providing further confidence in the robustness of the method and opening the way to the instability analysis of multi-body configurations. Two dominant modes were identified across the range $3 \leq U^* \leq 14$. For values of the reduced velocity $U^* < 4$, only one mode is unstable and the cylinders oscillate out of lock-in. At $U^* = 4$ the second mode loses its stability and the cylinders enter the lock-in zone, then for $U^* = 5$ the modes cross and their interaction gives rise to the beating phenomenon observed in the nonlinear simulations. For $U^* > 5$ the growth rate of the dominant mode is significantly greater than that of the other one, justifying the higher amplitude of vibration observed in the calculations. The comparison with the linear stability of the fixed-free configuration shows that the mechanism giving rise to large amplitude oscillations is already present in the latter case, as the growth rate of the unstable mode grows in a similar fashion for $U^* > 5$ while its frequency is always close to that of the stationary wake mode. This observation implies that the vortex-shedding plays a major role in triggering the vibrations of the rear cylinder and that interference effects between the cylinders come into play only when the vertical separation between the two cylinders is large enough, as suggested in the literature.

The matrix-free nature of the algorithm presented makes it particularly convenient for the analysis of three-dimensional flows around structures with complex geometries, where an analytical linearization of the coupled systems of equations would be impracticable. In addition, multiple bodies can be handled by the methodology with no added complexity. Moreover, the Cartesian grid employed within the IB framework facilitates the parallelization of the numerical scheme, which is an essential feature for solving three-dimensional problems within a reasonable time. One major advantage of the methodology resides in the generality and modularity of the formulation, which does not depend on the specific time-stepping scheme chosen for integrating the governing equations. Without the pretense of being exhaustive, some guidelines were provided for the selection of the linearization parameters, with the purpose to furnish the reader with the necessary tools to implement the strategy within existing codes.

Future developments of the method could include a local grid refinement to achieve a higher resolution near the immersed surface at a lower cost. The validation tests were limited to the case of rigid-body motion, nevertheless, it is straightforward to

extend the range of applicability of the method to deformable structures.

In the last chapter, an Arbitrary Lagrangian Eulerian framework was adopted to investigate the linear dynamics of a gas bubble placed in an axisymmetric straining flow. The maximum Weber number We_c was determined, beyond which no steady state is possible. Besides, by means of a pseudo-arc-length continuation method, an unstable branch of solutions was identified and a saddle-node bifurcation is detected. Edge states along this unstable branch constitute routes to the bubble breakup through an end-pinching mechanism.

Besides, the analysis revealed the existence of a self-propelling unstable mode, which is counterintuitive as the mode drifts the babble towards a higher-pressure region. It was shown that the observed dynamics is made possible by a self-propulsion mechanism that exploits shape asymmetries to create positive pressure differences.

Appendix A

APPENDIX

A.1 Derivation of the Gateaux derivative

In this annex it is reported, for the sake of completeness, the detailed derivation of Equation 3.14 presented in section 3.4.

Combining the definitions of $\boldsymbol{F}$ and $\boldsymbol{R}(\boldsymbol{q})$ given in section 3.4, we get

$$\boldsymbol{F}(\boldsymbol{q}(t_0), T) = \int_{t_0}^{t_0+T} \boldsymbol{R}(\boldsymbol{q}(t))dt + \boldsymbol{q}(t_0). \tag{A.1}$$

We now consider the second term on the right-hand side of Equation 3.13. Substituting the expression above, it reads

$$\left.\frac{\partial \boldsymbol{F}(\boldsymbol{q}, T)}{\partial \boldsymbol{q}}\right|_{\boldsymbol{q}_b} \boldsymbol{q}'(t_0) = \left.\frac{\partial}{\partial \boldsymbol{q}}\right|_{\boldsymbol{q}_b} \left[\int_{t_0}^{t_0+T} \boldsymbol{R}(\boldsymbol{q})dt\right] \boldsymbol{q}'(t_0) + \boldsymbol{q}'(t_0). \tag{A.2}$$

Recognizing that the extremes of integration do not depend on $\boldsymbol{q}$ and that $\boldsymbol{q}'(t_0)$ does not depend on time, we can interchange integration and differentiation and bring $\boldsymbol{q}'(t_0)$ inside the integral,

$$\left.\frac{\partial \boldsymbol{F}(\boldsymbol{q}, T)}{\partial \boldsymbol{q}}\right|_{\boldsymbol{q}_b} \boldsymbol{q}'(t_0) = \int_{t_0}^{t_0+T} \left.\frac{\partial \boldsymbol{R}(\boldsymbol{q})}{\partial \boldsymbol{q}}\right|_{\boldsymbol{q}_b} \boldsymbol{q}'(t_0)dt + \boldsymbol{q}'(t_0). \tag{A.3}$$

Supposing then a little variation of $\boldsymbol{q}'(t)$ in the interval $[t_0, t_0+T]$, which is true for small values of T, we have replaced $\boldsymbol{q}'(t_0)$ into the integral with $\boldsymbol{q}'(t)$.

$$\int_{t_0}^{t_0+T} \left.\frac{\partial \boldsymbol{R}(\boldsymbol{q})}{\partial \boldsymbol{q}}\right|_{\boldsymbol{q}_b} \boldsymbol{q}'(t_0)dt \approx \int_{t_0}^{t_0+T} \boldsymbol{J}(\boldsymbol{q}_b)\boldsymbol{q}'(t)dt. \tag{A.4}$$

Finally, we recognize that Equation A.4 is simply the integration of the initial value problem given by Equation 3.7, and therefore

$$\left.\frac{\partial \boldsymbol{F}(\boldsymbol{q}, T)}{\partial \boldsymbol{q}}\right|_{\boldsymbol{q}_b} \boldsymbol{q}'(t_0) \approx \boldsymbol{q}'(t_0+T) - \boldsymbol{q}'(t_0). \tag{A.5}$$

A.2 Grid convergence tests

To assess the grid and domain convergence of the stability results, eigenvalue computations were performed on different grids for the VIV case presented in 3.5, with $(\rho^*, U^*) = (20, 7)$.

Table A.1 reports the growth rate ω_r and the Strouhal number St of the least stable eigenvalue for four different discretizations of the same domain of size $[-28D : 52D] \times [-28D : 28D]$, with the origin placed on the cylinder axis. On the rightmost column, it is reported the percentage error $e_{\%j}$ made in computing the eigenvalue ω_j, as the finest grid is taken as reference,

$$e_{\%j} = \frac{|\omega_j - \omega_{ref}|}{|\omega_{ref}|} \times 100. \tag{A.6}$$

Grid	N_c	Δx_{min}	ω_r	St	$e_{\%}$
1	310800	0.0286	0.0427	0.1205	0.662
2	513000	0.0220	0.0447	0.1210	0.221
3	765600	0.0182	0.0448	0.1211	0.106
4	1068600	0.0154	0.0447	0.1213	—

Table A.1: Convergence study with respect to grid resolution. For each of the four grids, the total number of cells N_c and the minimum cell dimension Δx_{min} are reported, together with the growth rate ω_r and the Strouhal number St of the least stable mode for $(Re, \rho^*, U^*) = (60, 20, 7)$. Grid 2 was used to obtain the results presented throughout the manuscript, while the relative error $e_{\%}$ is computed with respect to the values obtained with grid 4.

Table A.2 reports the growth rate and the non-dimensional frequency of both the fluid and elastic modes for three distinct domains. The corresponding grids are coincident in the uniformly spaced rectangular zone around the cylinder, the minimum spacing being equal to $\Delta x_{min} = 0.022$. In particular, the grid used for the medium domain $D2$ corresponds to grid 2 in A.1. The analysis shows a minor difference between the medium and big domains, thus motivating the choice of $D2$ as the computational domain for the cases presented in section 3.5 The blockage ratio reported in A.2 is defined as the ratio of the cylinder diameter to the cross-stream dimension of the computational domain.

A.3 Effect of the linearization parameter ϵ_0

To evaluate the influence of the user-defined linearization parameter ϵ_0 on the accuracy of the results, it is reported in Figure A.3.1 the variation of the relative error e_r and the residual $\|\boldsymbol{r}\|$ of the least stable Ritz pair against ϵ_0. The former is given by

$$e_r = \frac{|\omega - \omega_{ref}|}{|\omega_{ref}|}, \tag{A.7}$$

	D1		D2		D3	
	1.43%		1.78%		2.38%	
	ω_r	St	ω_r	St	ω_r	St
FM	0.0440	0.1206	0.0447	0.1210	0.0461	0.1219
EM	0.0086	0.1309	0.0085	0.1309	0.0080	0.1308

Table A.2: Sensitivity of the rightmost eigenvalues to the size of the computational domain for $(Re, \rho^*, U^*) = (60, 20, 7)$. $D1$: $[-35 : 65] \times [-35 : 35]$, $D2$: $[-28 : 52] \times [-28 : 28]$, $D3$: $[-21 : 39] \times [-21 : 21]$. All the grids used for the analysis have the same minimum cell dimension Δx_{min}. The percentage blockage ratio is reported for each domain size.

where ω is the least stable eigenvalue computed for a given value of ϵ_0 on the chosen grid and ω_{ref} is a reference value. In the absence of an exact solution of the EVP, the selected ω_{ref} is the least stable eigenvalue computed on a reference grid with the parameter ϵ_0 chosen so as to minimize the residual $\|\boldsymbol{r}\|$. The results displayed in A.3.1 refer to the VIV case introduced in section 3.5 with $(Re, \rho^*, U^*) = (60, 20, 7)$.

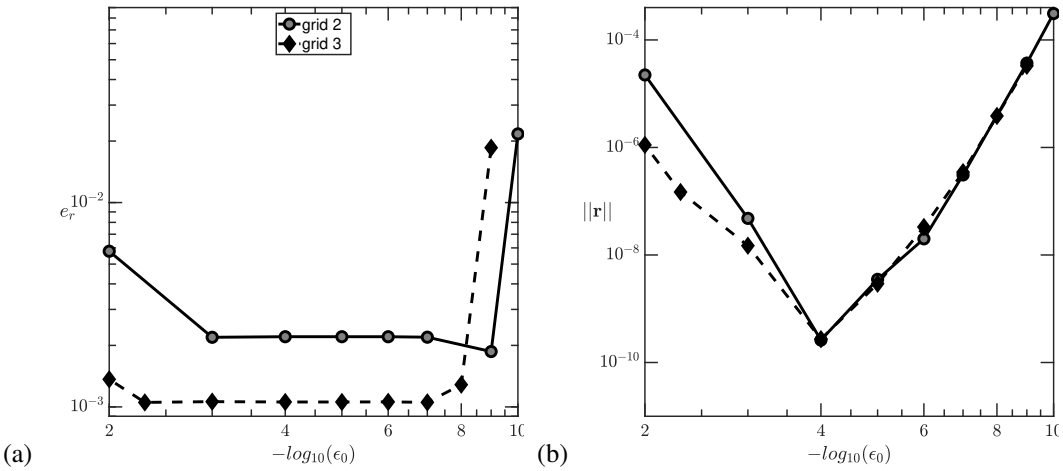

Figure A.3.1: Effect of the input parameter ϵ_0 on the relative error (a) and direct residual (b) for the VIV case reported in section 3.5 with the following set of parameters ($\rho^* = 20$, $Re = 60$, $U^* = 7$). Results are reported for two different grids (see Table A.1 for details), the relative error is computed with respect to the finest grid in Table A.1

INDEX